UNIVERSITY OF COPENHAGEN
FACULTY OF SCIENCE

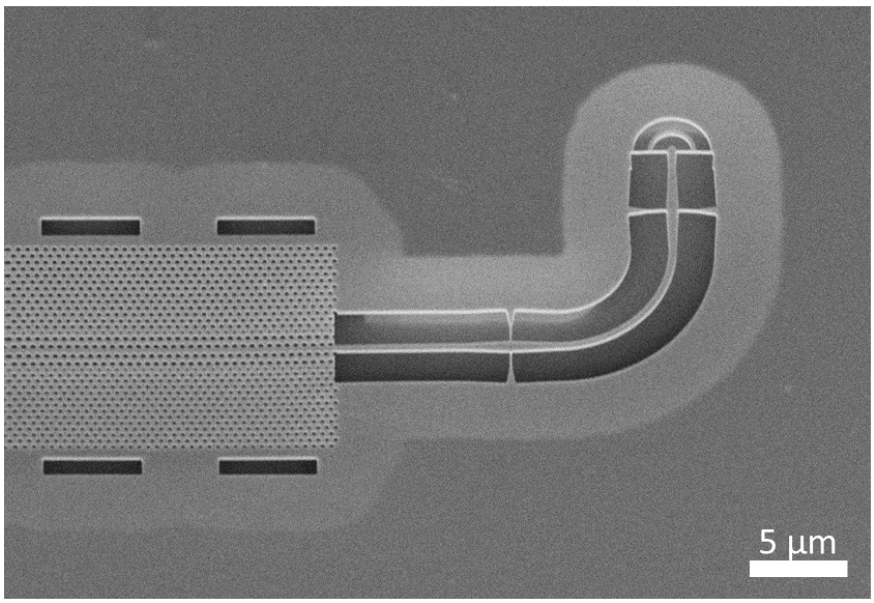

PhD Thesis

Experiments on Glide-Symmetric Photonic-Crystal Waveguides

CHIRAG MURENDRANATH PATIL

Advisor : ALBERT SCHLIESSER

Niels Bohr Institute

UNIVERSITY OF COPENHAGEN

Copenhagen, Denmark 2020

Ph.D. thesis 2020

This thesis is submitted in partial fulfilment for the degree of Ph.D at

The Niels Bohr Institute

University of Copenhagen

Experiments on glide-symmetric photonic-crystal waveguides

Chirag Murendranath Patil

Advisor :

Albert Schliesser

Copenhagen, Denmark 2020

Faculty of Science

Niels Bohn Institute

University of Copenhagen

Copenhagen, Denmark 2020

Experiments on glide-symmetric photonic-crystal waveguides
CHIRAG MURENDRANATH PATIL

Supervisor: Albert Schliesser
Søren Stobbe

PhD Thesis 2020
Faculty of Science
Niels Bohr Institute
University of Copenhagen
Blegdemsvej 17
2100, Copenhagen.
Telephone +45 35 32 52 09

Cover: Pespective scanning electron-micrograph of a glide-symmetric photonic-crystal waveguide membrane.

Typeset in LaTeX
Copenhagen, Denmark 2020

Abstract

This thesis is intended to report the research outcome of the fabrication and characterization of glide-symmetry photonic-crystal waveguides on a silicon-on-insulator (SOI) platform. The glide-symmetry waveguide has the potential to offer new functionalities in the realm of chiral quantum-optics. These waveguides can support circularly polarized light, which is important for observing chiral behavior. Additionally, the presence of a band-crossing at the Brillouin-zone edge offers an interesting feature.

Silicon is a promising substrate for fabricating both active and passive nanophotonic devices, and has a huge potential for building photonic integrated-circuits. An optimized recipe to fabricate photonic-crystal waveguides on SOI platform has been described. Major challenges and drawbacks have been investigated and reported. The final devices are optically characterized and measured to study the various properties of the photonic-crystal waveguides.

A free-space optics characterization setup is built to perform transmission measurements on resonators and photonic circuits. Measurements are performed on more than 150 devices for statistical averaging on an ensemble of photonic-crystal waveguides. From the glide-symmetry waveguide resonator design, slow-light phenomenon is observed, the group index is extracted and its implications are discussed. A combination of slow-light and transmission over band-crossing in photonic-crystal lattices presents an opportunity to investigate interesting features.

Further, a novel criterion to qualitatively measure the localization length is also proposed. Localization length is a key parameter to detect the onset of Anderson localization in disordered systems. The Thouless criterion clearly distinguishes localized and non-localized modes by making a connection between fluctuations in conductance with localization. This criterion is explored and combined with systematic variation of sample size to extract the localization length in a simplified manner. This method is further verified experimentally for two different variations of photonic-crystal waveguide.

Keywords: Photonic-crystals, glide-symmetry, fabrication, localization.

Acknowledgements

The results presented in this thesis is a culmination of work carried out between April 2016 to September 2019. Under the supervision of Associate Professor. Søren Stobbe, the work was initially carried out at the Niels Bohr Institute, University of Copenhagen in the Quantum Photonics group of Professor. Peter Lodahl. Since February 2018, the work was conducted at DTU, Fotonik in the Quantum and Laser Photonics group of Professor. Jesper Mørk.

Firstly, I would like to express my profound gratitude to Associate Professor. Søren Stobbe for providing an opportunity to carry out my project in this exciting field of silicon photonics. The journey has had many ups and downs, old chapters ended and new chapters written, and I'm glad that Søren stood by me at every stage. Be it the recipe to fabricate nanostructures or to brew coffee, consistency and perfection has been the hallmark of his approach, and hence my motivation.

Niels Bohr Institute provided an ideal start for my research career, and for this, I would like to thank Professor. Peter Lodahl for welcoming me into his group. Many thanks to Associate Professor. Leonardo Midolo for making me feel comfortable and helping me to get on track with the research. During my initial days, I had the pleasure of working with Xiaoyan Zhou and Morten Herskind, whose expertise on the measurement setup set the stage for initial measurements. I appreciate their company and support. Office colleagues form an integral part and the experience has been very encouraging. I have had the pleasure to experience the best of Tommaso Pregnolato, Thomas Hummel, Asli Dilara Ugurlu, Konstantinos Tsoukalas, and Kasper Lund. It has been a pleasure sharing so many memories with everyone.

The second half of my time was spent at DTU, Fotonik. I would like to thank Professor. Jesper Mork for welcoming into his group midway which allowed me to continue on my research unhindered. Special thanks to Professor. Albert Schliesser from NBI for agreeing to be my supervisor while I carried out my work at DTU, Fotonik. I'm indebted to Babak Lahijani and Marcus Albrechtsen for their friendship, the thought-provoking conversations and invaluable feedback while preparing this thesis. I would like to thank all the members of the Quantum and Laser Photonics

group for the good discussions, warm coffee breaks, and enjoyable environment.
I have spent hours trying to learn, optimize, and fabricate samples in the cleanroom facility at DTU Nanolab. Special thanks to Jesper Hanberg for his constant support and help in adjusting with the flow of cleanroom life. Along with the other staff at DTU Nanolab cleanroom facility, I'd like to thank the following staff for their invaluable inputs and discussions: Jonas Michael-Lindhard, Lean Gottlieb Pedersen, Thomas Pedersen, and Peixiong Shi.
As a part of my external stay, I had the opportunity to perform an external project at Accelink Denmark in Hillerød. I'd like to convey my sincere thanks to Yueqiang Shen, CEO at Accelink Denmark A/S, for providing me an opportunity to work at the company and Dan Zauner for the very constructive supervision.
It was a pleasure to collaborate and work with Pedro David García Fernández and Guillermo Arregui from the Catalan Institute of Nanoscience and Nanotechnology (ICN2), Barcelona on the localization length project. Thanks for all the good discussions and for performing the measurements with your setup.
Being away from NBI was never a hassle. Many thanks to Charlotte Hviid for helping me at every stage of my Ph.D. stay. This research has been supported by the Villum Foundation Young Investigator Programme and The Innovation Fund Denmark (Quantum Innovation Center 'Qubiz'). I highly appreciate their generous support.
Lastly, I would like to thank my friends for their continuous backing, family for their belief, and Sandeep Anjan for your hard-hitting motivational speeches. Heartfelt gratitude to my mother for patiently bearing me and to my father for all the motivation.

Chirag M Patil, Copenhagen, Dec 2019

Publications

Part of the work reported in this thesis was presented at the following conference.

- **C. M. Patil**, X. Zhou, M. Herskind, K. E. Lund, and S. Stobbe, "Transmission experiments on photonic-crystal waveguides with a symmetry-protected dirac point," in CLEO: Science and Innovations, (Optical Society of America, 2018), pp.STh3A–6

Contents

1 Introduction **1**

2 Introduction to photonic crystals **7**

2.1 Background 7

2.1.1 Defects in photonic crystals 16

2.2 Dispersion engineering 18

2.3 Slow light 19

2.4 Limitations of slow light in photonic crystals 23

2.4.1 Role of disorder 24

2.4.2 Impact of Anderson localization of light 26

2.5 Glide-symmetry waveguide 27

2.5.1 Design considerations 28

3 Waveguide coupling **33**

3.1 Grating coupler 35

3.1.1 Facet-coupling 37

3.1.2 Circular coupler gratings 38

3.1.3 Orthogonal coupling design 40

3.2 Mode converter 44

4 Nanofabrication **49**

4.1 Surface preparation 50

4.2 Resist preparation 52

4.3 Lithography 53

4.3.1 Electron beam lithography 54

4.3.1.1 Stitching errors . . . 55
4.3.1.2 Proximity effects . . . 56
4.3.1.3 Charging effects . . . 61
4.4 Etching process . . . 62
4.4.1 Inductively-coupled-plasma dry etching . . . 62
4.4.2 Buried oxide wet etching . . . 65
4.5 Sample drying . . . 67

5 Experimental characterization 69
5.1 Overview . . . 69
5.2 Probe techniques . . . 72

6 Transmission measurements on photonic-crystal waveguides 75
6.1 W1 waveguide . . . 76
6.2 Glide-symmetry waveguides . . . 81
6.3 Coupling through nanobeam waveguide . . . 89
6.4 Measuring localization length and multiple scattering . . . 94

7 Conclusion 99

Bibliography 103

A Process recipe I

B Ensemble measurements VII

C Hole radii analysis XVII

D Fabry-Peròt fringe analysis XIX
D.1 Peak search method . . . XIX
D.2 Calculating the shift parameter . . . XX
D.3 Factor of 2 in group index . . . XXI

E Polarization experiments XXV

1

Introduction

Photonics is considered as one of the key drivers of technology in the 21st century. From the early demonstrations of lasers [1, 2] and fiber optics [3] in the 60's to present day advanced optical computing [4, 5], photonics has made great strides for practical applications. More than 20 Nobel prizes were awarded for pioneering works in photonics and photonics-related research since the beginning of this millennium. The invention of semiconductor-based blue light-emitting diode [6, 7] to the development of single-molecule microscopy techniques [8] in chemistry, optical tweezers [9] to ultra-short optical pulse generation techniques [10]; photonics has made an indelible impression on the scientific community. This has eventually led to the successful commercialization of high performance devices like optical fibers [11], photovoltaics [12], and light-emitting diodes [13] which are now leading a revolution in energy efficiency. It can be rightly said that light-based technologies have undergone dramatic advances and thus have successfully established themselves as key enabling technologies in the present day.

Photons, the fundamental quanta of light, can be harnessed to realize faster and energy-efficient optical components. After conceiving and developing these optical components, it has become as pervasive as electronics. Cutting-edge technologies have made it possible to realize these components to generate, manipulate and detect photons for various applications. Information and communication technology, high-resolution displays, photovoltaics technology, coherent laser sources, fiber optics, electro-optics, nano-opto-electro-mechanical systems, multiprocessing core, and quantum information processing are few platforms where photonics has exceeded all expectations in terms of performance [14–17]. Using these components as building

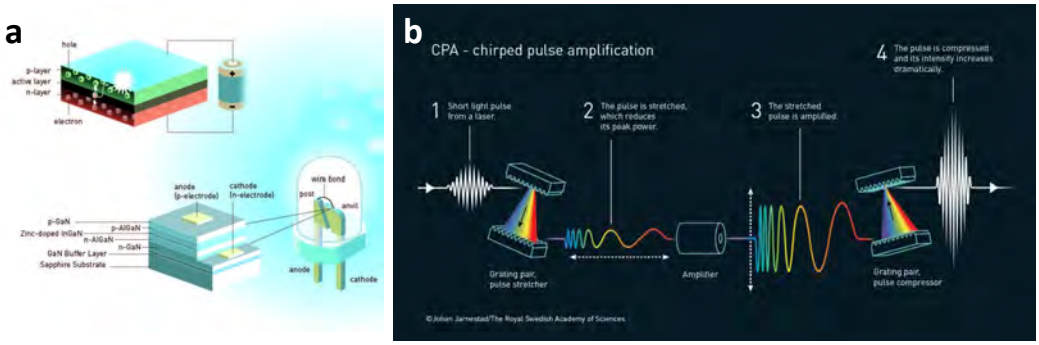

Figure 1.1: Noble Prize in Photonics. (a) The invention of blue light-emitting diodes enabled a new generation of energy-efficient lamps which had the greatest impact on global energy savings. (b) Chirped pulse amplification technique allows for generating highly intense laser pulses which is now used in specialized surgery equipment, industries, and other high-power laser facilities. Images taken from the Royal Swedish Academy of Science.

blocks, a much larger platform can be conceived where all the functionalities work seamlessly in tandem.

In fiber optics, light, more specifically infrared light with wavelengths around 1550 nm is used as a carrier for data transfer and communication over long distances. Apart from long-distance data transfer, the principle of using light can be extended to operating logic gates as well. Using these fundamental gates as building blocks, huge circuits which operate on light were conceived. These integrated photonic-circuits gained attention when telecommunication operators were looking for a highly disruptive technology that could meet the consumer demand for ultra-high bandwidth at a much lower cost than with traditional electronic integrated circuits. Photonics underpins various technologies to meet these demands. Photonic integrated circuits can integrate several components on the same chip and at the same time leave a small footprint. Components such as arrayed waveguide gratings, gigahertz switches, optical transceivers, laser sources, filters, amplifiers, and detectors can be densely packed on a single chip allowing it to have a significant advantage compared to traditional table-top photonic system assemblies. This leads to a more efficient and highly integrated on-chip optical functionalities. These levels of miniaturization and integration have been made possible because of one freely available semiconductor

material, silicon.

Silicon has for a long time been the backbone of the electronics industry. The technological progress in the electronic industry hinges on one key factor: integration of devices. The ability to fabricate billions of transistors and other solid state devices on a 1 mm × 1 mm size silicon chip has brought massive improvements in computing power. Photonics has followed the same trends paving the way for the next generation of ultra-fast highly integrated optical-components. High-density integration of components leads to miniaturization of building blocks. It would be possible to realize wide range of optical designs defined according to application specifications on a small footprint. This has been made possible because of advances in CMOS fabrication. Further, advanced nanofabrication processes have propelled silicon photonics to new heights.

Silicon photonic has many superior features. The high refractive index of silicon waveguides allows for efficient guiding of light and are typically 500 times smaller than conventional silica-based waveguides [18]. Although silicon has been a dependable platform for integrated photonics, the emission of light is still a major challenge. Silicon cannot emit light because of its indirect band-gap and strong absorption in the near-infrared spectrum. This issue can be solved by fabricating lasers using high gain materials like gallium arsenide and integrating them on a silicon platform. Silicon can then manipulate this light to generate other wavelengths. Engineered waveguides can confine light within small volume allowing for nonlinear behavior [19]. They can also be tailored to operate at specific frequencies and over a required bandwidth of light. Quantum dots embedded in waveguides, metamaterials, and photonic crystals are few configurations in which light is confined to subwavelength scale regions and allows for observing exotic optical properties [17].

The characteristic feature of photonic crystals that distinguishes them from other optical devices is the periodicity of their refractive index. This allows for the light waves to undergo multiple reflections forming different interference patterns in different directions. This property allows for the photonic crystals to confine light making them a promising candidate for a wide range of applications. They utilize the existence of photonic band-gaps to limit the propagation of light of certain wave-

lengths to produce desired effects like superprism effect [20], slow-light effect [21] and band-gap effects [22]. This thesis explores a new class of photonic crystals and their unique properties. Chapter 2 is dedicated to understanding the basic concepts required to construct these devices.

The main goal of this project has been to study and characterize a new photonic crystal design that can cater to a new line of research that has focused on exploiting slow-light effects towards manipulation and control of light. Glide-symmetry waveguides have been employed in studies of chiral quantum optics [4] where the main goal is maximizing the circular local density of optical states. This property can be further enhanced by increasing the interaction strength between light and matter. Slow-light phenomenon is a very strong tool to enhance this interaction strength.

Glide-symmetric waveguides have been the subject of theoretical studies due to their interesting properties with regards to suppressing out-of-plane scattering [23] and their photonic spin-orbit interaction [24]. However, experimental investigations on glide-symmetry waveguides are limited [25]. The group velocity and its dispersion, which play a crucial role to determine chirality, as well as the propagation properties have not been addressed experimentally so far. In section 2.5, the construction of a glide-symmetry waveguide is discussed while emphasizing the important features of interest.

In this thesis, I fabricate and characterize the optical properties of glide-symmetry waveguides on the silicon-on-insulator platform. The aim is to establish an optimized fabrication process to realize highly reproducible and robust waveguides. An optimized recipe, controlled with high precision is demonstrated in the Chapter 4. It can be quite a challenge to couple light into waveguides which are few microns in size using free-space optical setup. Chapter 3 describes the different coupler designs that have been implemented. A mode converter that solves this issue at a more commercial level has also been discussed. The characterization techniques and measurement setup required to measure transmission are discussed in Chapter 5. I perform a detailed study of slow-light properties in the glide-symmetry waveguides, by examining the group index in a resonant structure. I also demonstrate the idea of transmission over a gapless feature in a photonic-crystal waveguide design. Fab-

rication limitations leads to nanoscale disorder which leads to high scattering losses during the propagation of light in these devices. The formation of random cavities eventually leads to localized modes, called Anderson localization. This has proved to be one of the main limiting factors for realizing low loss photonic waveguides. A novel approach to quantitatively measure the localization length, which is a characteristic length scales over which localization occurs is also discussed. These results have been discussed in detail in Chapter 6.

2

Introduction to photonic crystals

Photonic crystals are a unique class of optical media that are formed from a periodic arrangement of two or more dielectric structures. This alternating refractive index profile causes light to interfere both constructively and destructively, giving rise to many interesting optical properties. Until recent years, the main attraction of these devices has been their ability to manipulate light in highly confined spaces [26–31]. More recently, they have been extended for the research of exotic physics in areas such as chiral quantum optics [4, 32], topological photonics [33–35] and valleytronics [36,37]. The ability to tailor the dispersive properties of photonic crystal to specific needs makes them an ideal platform for many potential applications.

2.1 Background

The propagation of waves through layered periodic structures was originally published by Lord Rayleigh in 1887 while studying the reflective properties of crystalline material [38]. This work provided for the first time the idea of a band-gap for electromagnetic waves which prohibited light propagation for a range of frequencies. This idea was further extended by Charles Galton Darwin who while analyzing the scattering of x-rays, figured out that for a certain range of angles, reflection was perfect and the transmitted beam extinguished much faster [39]. It took several decades to make a leap from layered periodic structures towards multilayered two- and three-dimensional structures. In 1979, Ohtaka developed a formalism to numerically analyze scattering of photons in a system of regular array of dielectric

spheres [40]. However, it wasn't until the pioneering works of Sajeev John and Eli Yablonovitch, who independently showed that like electrons, light waves could also be controlled by creating artificial periodic structures in two- and three-dimensions. Eli Yablonovitch while trying to address the suppression of lateral spontaneous emission in microcavities, proposed adding periodicity in three-dimensions [41]. This resulted in the formation of an omnidirectional forbidden band-gap. Around the same time, Sajeev John independently observed that the phenomenon of Anderson localization in disordered solid can be extended to optical systems, and showed that increased scattering can lead to strong localization of electromagnetic waves in disordered periodic structures [42]. These initial ideas triggered numerous research activities for realizing photonic band-gaps, localized defect-modes and other optical phenomena in photonic crystals.

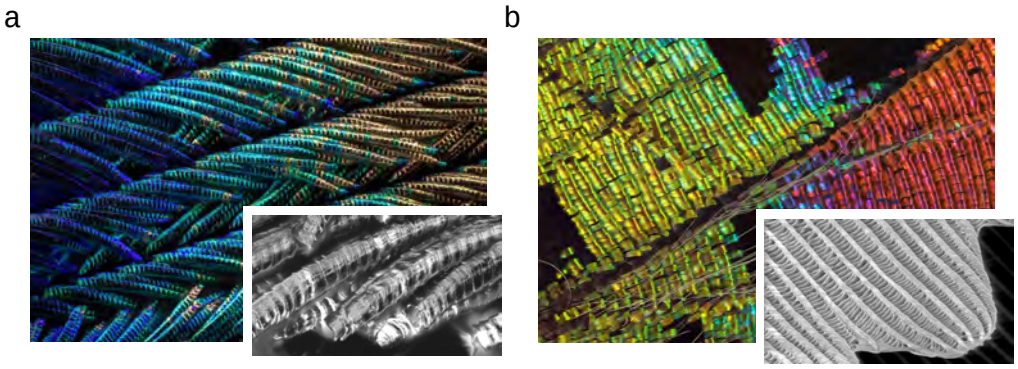

Figure 2.1: Photonic crystals observed in nature. False-color image of the feather of a peacock (a) and wingspan of a butterfly (b) observed through a microscope. The insets illustrate the periodic structures as seen under an electron microscope. Images are used with permission from the respective owners (Waldo Nell and Linden Gledhill).

Two-dimensional photonic crystals can be found in abundance in nature. The brightly colored feathers of birds, butterfly wings, and beetles are a few reasonably good examples. A detailed examination of these structures reveals high-index fibrous filaments arranged periodically and separated by thin layers of air. Each filament consists of periodically arranged micro-structures made from chitin which scatter light. The spacing between the scatterers determines the wavelength that is

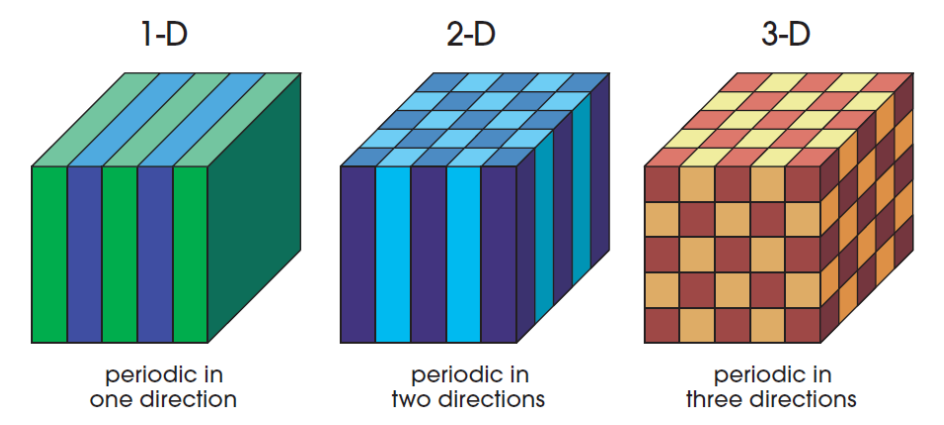

Figure 2.2: Illustration of one-, two-, and three-dimensional photonic crystals. A simple sketch explaining the periodicity of dielectric materials extending in different directions. Here, different colors represents a different material. Image taken from [22].

reflected producing bright iridescence when viewed from certain angles [43].

Artificially created photonic-crystals are optical materials formed by periodically stacking layers of dielectric media with different optical parameters [22, 41]. The periodic structure is made of at least two materials having different dielectric constants, ϵ. These classes of optical structures demonstrates peculiar properties which open new avenues for realizing different applications [20, 44–46]. Photonic crystals can be distinguished based on the spatial arrangement of the dielectric functions as illustrated in Fig. 2.2. A one-dimensional photonic crystal has a periodic modulation of refractive index in one dimension, while the medium is uniform in the other two directions. A vertical-cavity surface-emitting laser consisting of Bragg reflector can be considered as a simple example. A two-dimensional photonic structure will have periodicity in two directions while being homogeneous along the third direction. The most commonly found examples are an array of dielectric rods in air or a porous silicon membrane with etched holes arranged in a lattice structure. Three-dimensional photonic crystals have periodic modulation in all directions and is the most challenging to artificially realize. Opal is a naturally occurring example where micro-spheres occupy the nodes of a face-centered cubic lattice giving bright colors at different angles. Advancements in nano-fabrication techniques have made

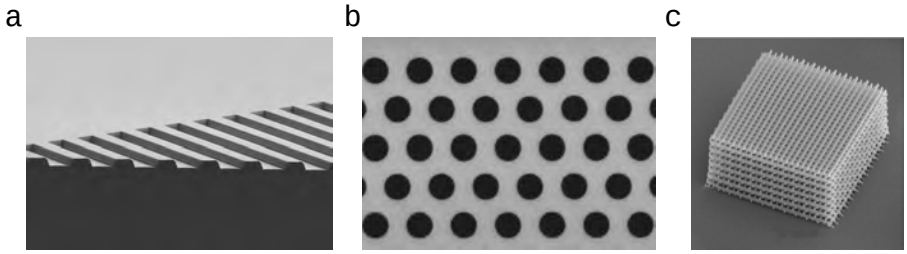

Figure 2.3: Examples of one-, two- and three-dimensional photonic crystals. Scanning electron micrograph of: (a) arrayed waveguides, (b) holes arranged in hexagonal lattice, and (c) woodpile structure [47].

it easier to realize a number of devices in all three configurations.

Photonic crystal structures are designed to affect the beam of light in the same way that an ordinary semiconductor would control the properties of electronic current. Like their electronic counterparts, photonic crystals can be characterized by band structures, which describe the range of energy levels a photon can occupy. A particularly interesting case is one where no states can exist for the photons to propagate. This range of frequencies is similar to the electronic band-gap observed in semiconductors and hence it is rightly called photonic band-gap. The photonic band-gap is formed from multiple Bragg reflections which are induced by the periodic dielectric profile of the materials. It defines a range of frequencies for which electromagnetic waves are forbidden to propagate inside the crystal [22]. This particular property has led to many innovative breakthroughs for controlling and manipulating the propagation of electromagnetic waves [48, 49].

Photonic band-gap

An omni-directional photonic band-gap can exist only in three-dimensional systems, where propagation of light is forbidden in all spatial directions. One- and two-dimensional systems exhibit incomplete band-gaps where light propagation is prohibited only for certain directions and polarizations in the photonic crystal.

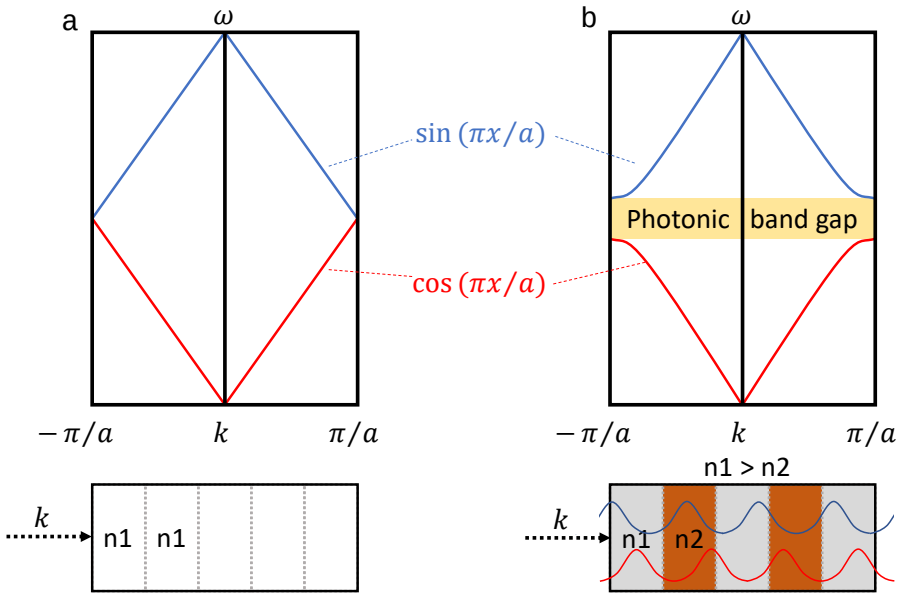

Figure 2.4: Dispersion relation for a one-dimensional photonic crystal. Frequency versus wavenumber relation for (a) uniform dielectric, and (b) periodic dielectric function highlighting the creating of a band-gap in one-dimensional systems.

The physics of band-gap can be well understood by examining the dispersion diagram, which maps out all the possible interactions of electromagnetic fields in a given system. An important consequence of the periodic dielectric function is that the optical modes can be calculated by using Bloch's theorem, i.e., the electric field equation should satisfy,

$$E_{n,k}(r + R) = e^{ik \cdot R} U_{n,k}(r) \tag{2.1}$$

where k is the Bloch wave vector and R is the primitive lattice-vector [22]. The solution to this equation gives eigenvalues $\omega(k)$ which forms a discrete band when plotted against wavevector k. For a homogeneous medium, this is given by $\omega(k) = ck/n$, where k is the wavevector and c/n is the speed of light in the given medium of uniform refractive index n. The eigensolutions are also periodic functions and must be invariant when translating over a unit-cell photonic crystal. This can be represented in the reduced Brillouin-zone notation (Fig. 2.4a), where it is restricted

between $k = +\pi/a$ and $k = -\pi/a$. The first- and the second-order modes are described by $\cos \pi x/a$ and $\sin \pi x/a$ respectively, which are the same for a uniform medium. Hence they converges at the same point at $k = \pm\pi/a$.

However, for a one-dimensional periodic structure of two different media with separate refractive indices, the two functions are no longer the same at the band edge. When light impinges with zero incidence angle at the interface of two different dielectric materials, a part of it is reflected. Subsequently, every alternating interface adds an additional phase-shift of π to the reflected wave. In other words, a phase difference of π builds up between two successively reflected waves. When the total phase difference between the reflected waves is 2π, they interfere constructively to generate standing waves (red and blue). A majority of power of the lower band (red) resides in the high index region, while the majority of the power for the second order band (blue) lies in the low index region. This is only possible if the two standing waves occupy different energies at the zone edge, thus resulting in band-splitting (Fig. 2.4b). The band-gap formed as a consequence, mainly depends on the index contrast between the two dielectric media, and constitutes a set of frequencies which are forbidden in this photonic structure. For large index contrast, the band-gap becomes much more pronounced for a range of frequencies that are fully affected for all wave-vector and angles.

These properties can be further applied to a two-dimensional photonic crystal, where periodicity extends in both x- and y-directions. In a two-dimension system, two different polarizations of the electromagnetic field can exist: transverse electric (TE) mode where the electric field is in the xy-plane ($E_z = 0$) and magnetic field is out of plane (z-axis); and transverse magnetic (TM) mode where the magnetic field is in the xy-plane ($H_z = 0$) and electric field is out of plane (z-axis). Consider a two-dimension lattice of air holes in dielectric (Fig. 2.5a) extended infinitely in the z-direction. The Bragg conditions can be applied here, that will establish the limits of the upper and lower edge of the band gap and set the characteristic frequencies at which reflection occurs. The dispersion relation for a two-dimensional photonic crystal is shown in Fig. 2.5c with the special directions denoted as Γ, K, and M.[1]

[1]The key points of symmetry are denoted as $\Gamma = 0$, $M = \frac{1}{2}\vec{T_1}$, and $K = \frac{1}{3}\vec{T_1} + \frac{1}{3}\vec{T_2}$, where $\vec{T_1}$

The frequencies are plotted for the k-points along the reduced Brillouin-zone edge (Fig. 2.5b, blue region). Here we can see that different polarization of light has different characteristic band features. For a TE-mode, a very large band-gap is formed whereas the TM-modes are characterized by the absence of a band-gap. A complete band-gap for both TE- and TM-modes can be realized by having high lattice symmetry and maximizing the dielectric constant contrast.

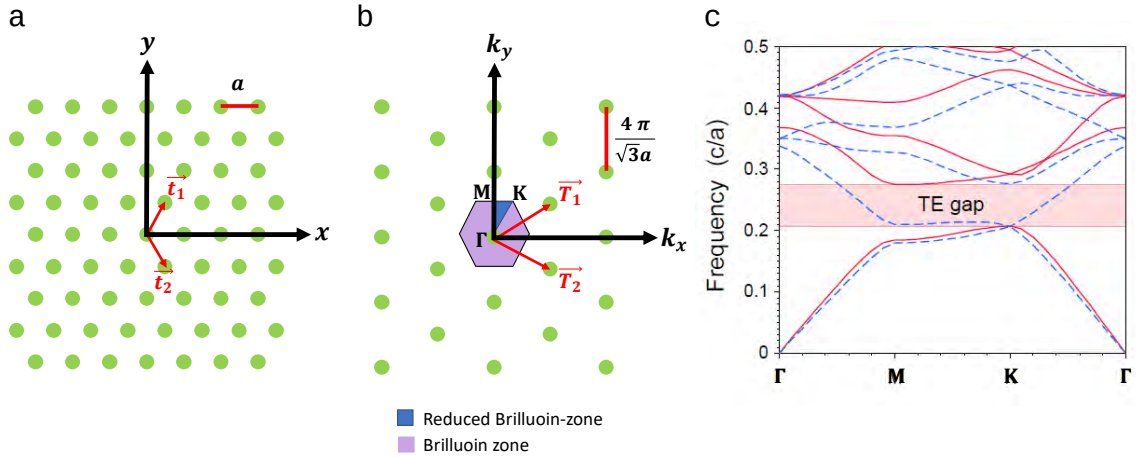

Figure 2.5: Two dimensional photonic crystal. (a) Real-space structure with points arranged in a hexagonal lattice, (b) reciprocal-space lattice with the reduced Brillouin zone in blue shade, and (c) the corresponding band diagram of a two-dimensional hexagonal lattice of air holes in a slab. Image (c) taken from [22].

Photonic crystal slab

A major drawback of two-dimensional photonic crystals is that the model is infinitely extended in the z-direction, and the incident wavevector is also invariant. For practical purposes, this can be realized as a two-dimensional photonic crystal slab by fabricating periodically structured geometric-patterns in a dielectric slab of finite thickness. In these structures, vertical confinement of light is provided by index-guiding mechanism[2] while the lateral in-plane confinement relies on the photonic-crystal band-gap properties. A combination of these two confinement mechanisms

and $\vec{T_2}$ are the reciprocal lattice vectors.

[2]as long as the photonic crystal slab is enclosed in a low-index medium.

allows us to realize localized and high quality-factor optical modes which can also be guided. Some energy can leak out as absorption or be dissipated into the environment. This can be resolved by designing photonic crystals for specific frequencies over which absorption is minimal [50].

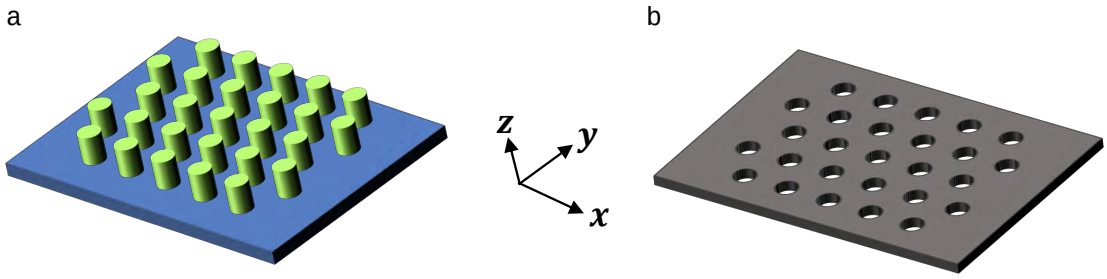

Figure 2.6: Two-dimensional photonic-crystal slab. An array of (a) vertical pillars and (b) air holes arranged in a hexagonal lattice-structure can be realized on a slab of finite thickness, where the geometry has dimensions comparable to the wavelength of incident light.

The ease of fabricating these structures and the ability to engineer the photonic dispersion has resulted in the development of several new systems compared to their two-dimensional counterparts [37, 51–53]. A simple photonic crystal slab can be either an array of vertical pillars in air, or more commonly an array of air-holes in a high dielectric medium like semiconductor (Fig. 2.6). Commonly used materials are silicon-on-insulator (SOI), gallium arsenide (GaAs), indium phosphide (InP), and silicon nitride (Si_3N_4) [54, 55]. These materials are transparent to wavelengths ranging from 600 nm to 1600 nm, making them ideal for various linear and non-linear applications over a broad spectrum [56]. It is important to note that the thickness of the semiconductor slab, the dimensions of various geometries, and the structural periodicity are comparable with the wavelength of the incident light.

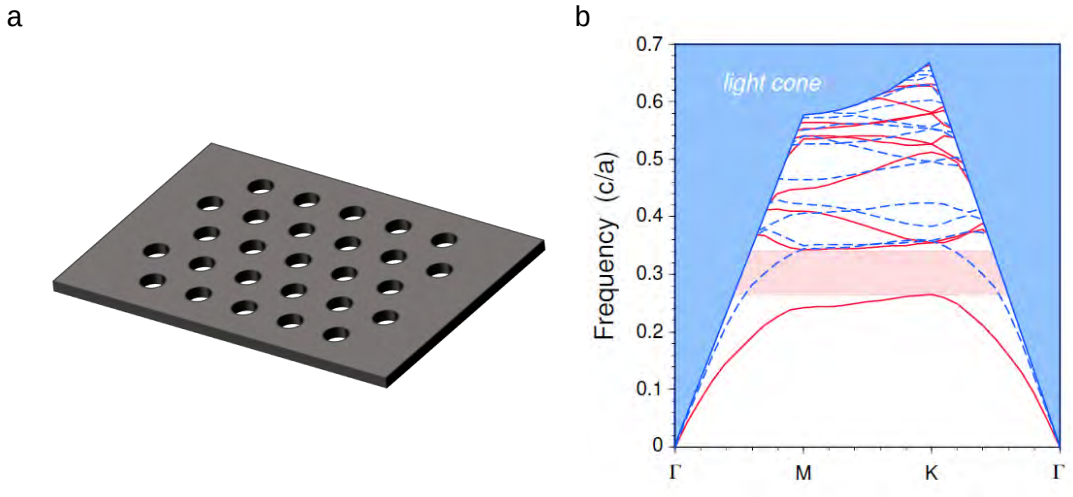

Figure 2.7: Band diagram for a photonic-crystal slab. (a) A two-dimensional photonic-crystal slab with air-holes arranged in a hexagonal lattice structure. (b) The corresponding band-diagram showing the TE-like (red) and the TM-like (blue) polarized guided modes. The red shaded area represents the band-gap in the TE-like mode where no states can exist. The blue shaded area represents all the states than can leak out-of-plane as radiation modes. Image (b) taken from [22].

In free space, the dispersion relation for a two-dimensional photonic crystal slab is given by $\omega = c\sqrt{k_x^2 + k_y^2}$. Since the Bloch wavevector k is conserved, the bulk and in-plane components projects a set of all the states which can radiate out of plane. This is depicted by the light cone which can be visualized as the light line in the projected band diagram. A light cone typically consists of a continuum of states existing in the bulk of the slab and is used to distinguish between leaky and non-leaky modes in a photonic crystal. Since the permittivity of the semiconductor is larger than that of air, guided modes which are lying below the light line are formed. These modes are confined to the slab and hence cannot couple to any vertically radiating mode [57]. If the photonic-crystal has a horizontal plane of mirror-symmetry at the center of the slab, then the polarization of the modes that can exist inside the slab can be even (quasi-TE) or odd (quasi-TM) [3] [22]. For a hexagonal lattice of holes, we can observe the formation of a band-gap for the TE-like modes while no

[3] At $z = 0$ plane, they are purely TE- and TM-modes in the case of an ideal two-dimensional photonic crystal structure.

gaps appear for the TM-like propagating mode (Fig. 2.7). The thickness of the slab and the regions surrounding the slab also plays an important role in determining whether the band gaps can exist or not [58]. Photonic-crystal slabs serve as a good starting point for developing numerous applications based on band-gap engineering. Guiding waveguides, optical resonators, and low-loss LED's are few photonic devices that have been demonstrated [59–61].

2.1.1 Defects in photonic crystals

Defects can be created in a regular photonic-crystal lattice by introducing random perturbations. This discontinuity breaks or destroys the translation symmetry leading to new optical observations. These defects act as scattering centers for the electromagnetic fields leading to cross-coupling between different Bloch modes [22]. Multiple scattering also means that they encounter different loss paths which leads to reduced propagation of light. However, depending on the nature of the defect, new states can be localized or guided with their frequencies lying in the photonic band-gap.

Photonic crystal cavities

A point-like defect can be formed by modifying the radius of a single air-hole or displacing its position slightly in a regular photonic-crystal lattice [62]. This creates a modulation of dielectric at the defect center which eventually leads to the transition of a dielectric (or air) band into the band-gap. Most of the field energy is concentrated around the defect. If sufficient number of reflective crystal-centers are not present around the defect, the mode is not localized and leaks into the external environment. By increasing the number of lateral crystal sites, a true bound state can be achieved by reducing the coupling of light into lossy modes. This forms a cavity resonator with perfectly reflecting walls and light does not leak in the lateral directions. The nature of this cavity is indicated by the quality factor, which is determined by the energy that a photon loses when it bounces back and forth within the resonator. The quality factor is defined as a ratio of energy stored in

the resonator to the energy dissipated per round-trip cycle. It depends on reflection losses at the interface of the cavity and external environment. Photonic crystals have the ability to strongly confine light in small volumes and this feature has led to many innovative devices for practical applications of light trapping. Wavelength filters [44,63], tunable lasers [14,45,64], high-Q cavities [65,66], nonlinear optics [19], and quantum information processing [46] are few areas where point-defect cavities have been employed.

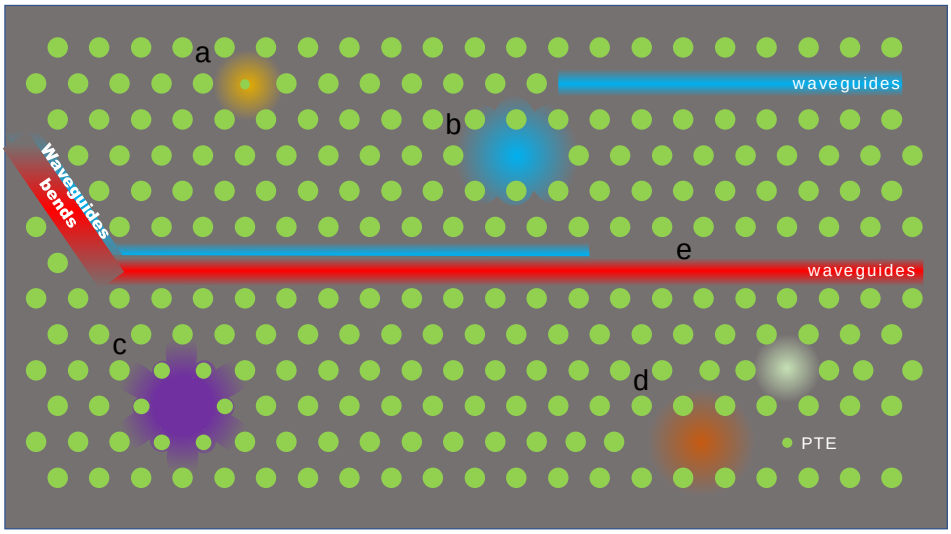

Figure 2.8: Localized defects in a photonic-crystal slab. Defects can be broadly classified as line-defect or point-defect and depending on the applications there can be many variations. Point-defects can be used for constructing (a) nanocavity laser (b) resonant-tunneling drop filter (c) cavity resonator and (d) Fano laser. (e) Waveguides, both straight and bent are a classic example of line-defect and can support propagation of modes.

Photonic-crystal waveguides

A line defect is formed by removing a row of holes in a regular photonic-crystal lattice. This forms a photonic-crystal waveguide, which can support propagating modes in a volume much smaller than optical fibers. Breaking the translation symmetry in the y-direction creates a set of photonic states in the photonic band-gap. These states or waveguide modes are forced along the direction of the linear defect, since they cannot propagate though the photonic crystal lattice. The guiding mechanism uses a combination of index guiding in the vertical out-of-plane direction and Bragg reflection confinement in the lateral in-plane directions. It has also been shown that these waveguides can provide strong confinement and are capable of guiding optical signals along tight bends with curvature angles as large as 60° [67]. Spatial confinement can also be realized by introducing a nanoscale slot along the line-defect direction [68]. Slot-geometries provide a promising architecture to realize index-sensitive sensors on a small platform [16, 69].

By combing waveguides and cavities, a resonant-tunneling drop filter can be constructed [70, 71]. This device can function as a wavelength division multiplexer on a photonic integrated-circuit platform. When a broadband light is coupled into the system, only the wavelengths which resonates with the cavity are coupled and exits through the output waveguide section, enabling the selection of light of certain wavelengths. Further, a multi-channel drop filter can also be realized using the same construction strategy [72].

2.2 Dispersion engineering

Dispersion is a characteristic property that causes different wavelengths to propagate with different velocities. This can be advantageous for some applications [20, 73], while detrimental for others. It is well known that photonic crystals are generally very dispersive owing to their periodic arrangement. Dispersion engineering allows us to tailor the material components for practical applications. From a spectral point of view, dispersion engineering allows us to target the telecom range of 1550 nm by

scaling the structure for the optical domain [50]. This involves modulating the permittivity as well as the effective refractive index of the periodic structure. There are many approaches to tailor dispersion in photonic crystals: modifying the air holes radii [28], shifting rows of air holes towards or away from the waveguide section [62], immersing slow-waveguides in different fluids [16], and symmetry modification [53] to mention few. Dispersion engineering represents one of the most researched areas in the field of photonic crystals. It can be used to allow or obstruct specific frequencies for a given photonic crystal design or to confine and guide light using self-collimation effect [74, 75]. In other cases, this can be used to create artificial materials with exotic states, which otherwise would not have existed in nature [76]. The interaction between light and matter has a strong impact on the dispersion of the propagating medium. An interesting consequence of this strong dispersion is the slow-light phenomenon.

2.3 Slow light

The speed of light travelling in vacuum is a constant value ($c = 299\,792\,458\,\mathrm{m\,s^{-1}}$) and is limited by the laws of physics. However, there is no lower limit to the speed of light [77]. When light enters into a homogeneous medium, it interacts with the charges in the material at the atomic scale, causing light to slow down. Though not a dramatic reduction, but it propagates with a speed which is lower than it's value in free space [27]. The slow-down factor of the propagating wave can be characterized by its phase refractive-index n. The phase velocity ν which determines the speed of light is given by,

$$\nu_p = \frac{\omega}{k} = \frac{c}{n}, \tag{2.2}$$

It is defined in terms of ω the angular frequency, and k the wavenumber. This applies to a wave propagating at a single frequency. Since pure sine waves do not convey much information for experimental analysis, we consider a combination of multiple plane waves oscillating at different frequencies. Multiple frequency components superimpose to form an envelope or a spectrum of frequencies, which travels

at a different group speed than that of individual frequencies. The group velocity describes how fast does the envelope of the wave's amplitude propagates.

$$\nu_g = \frac{\delta\omega}{\delta k} = \frac{c}{n} - \frac{ck}{n^2} \cdot \frac{dn}{dk} \tag{2.3}$$

where c/n is the phase velocity. For a non-dispersive media, the refractive index does not change with respect to k ($\frac{dn}{dk} = 0$) and hence phase velocity and group velocity are the same. The situation is different for a dispersive media where refractive index is a function of frequency. Based on the previous equations, the group velocity for a dispersive media is given by,

$$\nu_g = \frac{\delta\omega}{\delta k} = \frac{c}{n(\omega) + \omega\frac{dn}{d\omega}} = \frac{c}{n_g(\omega)} \tag{2.4}$$

Where n_g is the group-velocity refractive index or group index of the dispersive media. It defines the factor by which the envelop of modulated wave slows down. Under restricted conditions, the group velocity might exceed the limit of speed of light, but it is not very useful for practical applications.

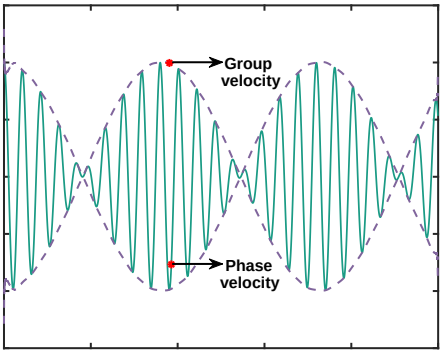

Figure 2.9: Group velocity and phase velocity. Illustration of a propagating wave, where the envelop travels with the group velocity and the carrier travels with the phase velocity.

We define the slow-wave in terms of group velocity. As seen in Eqn. 2.3, the sign of the derivative term that quantifies dispersion, determines if the group velocity is slower or faster. Slow waves cannot occur in vacuum and strong dispersion is necessary to observe this phenomenon. There is an increased interaction of the light

waves traveling through the dispersive medium, and that is what is slowing down the wave [78].

How do we slow the waves in practical media? We have to induce dispersion to observe slow waves. We can either rely on naturally occurring dispersive materials or we can cause dispersion with structural optical elements like gratings and photonic crystals. In both cases, refractive index is changing and that is the fundamental mechanism that is slowing down the wave. In order to bring the wave to a complete halt, we must have infinite dispersion at a pure frequency ω i.e., $\frac{1}{dn/d\omega}$ has to be zero.

There are two broad schemes for slowing down electromagnetic waves. Material-based slow-wave devices where we can choose materials which produce the required dispersion at the atomic scale, and structure-based slow-wave devices where the geometry of the structure dictates the dispersion properties. Material dispersion systems require extreme environment like cryogenic temperatures and high pressure to generate media with highly dispersive optical properties. This has been demonstrated in Rubidium-based vapor cells and Bose-Einstein condensates where extreme slow down factors have been measured [77, 79]. However, their complex systems make them irrelevant for realizing slow-light devices integrated on a chip. Devices whose dispersion can be tuned easily by structural modifications are the preferred platform for studying the slow-wave phenomenon owing to the simplicity of their construction and their compatibility with on-chip integration. Systematic design of geometry has led to the observation of slow light in both passive and active optical devices like ridge waveguides, photonic crystals, and resonators.

The phenomenon of slow-light has been extensively studied for its potential applications in time-domain signal processing for optical delay lines [80], optical switching [81, 82], and on-chip spectrometers [83–85]. Silicon-based slab waveguides were one of the earliest researched optical device to study the slow-light effect. It is known that interesting phenomena arises at the cut-off region [30]. For a slab waveguide, the waveguide modes tend to be dispersive owing to the high index contrast between silicon core and air. The slope at this point, $d\omega/dk$ which is the group velocity approaches zero implying that light can be slowed down. Likewise, the group-velocity

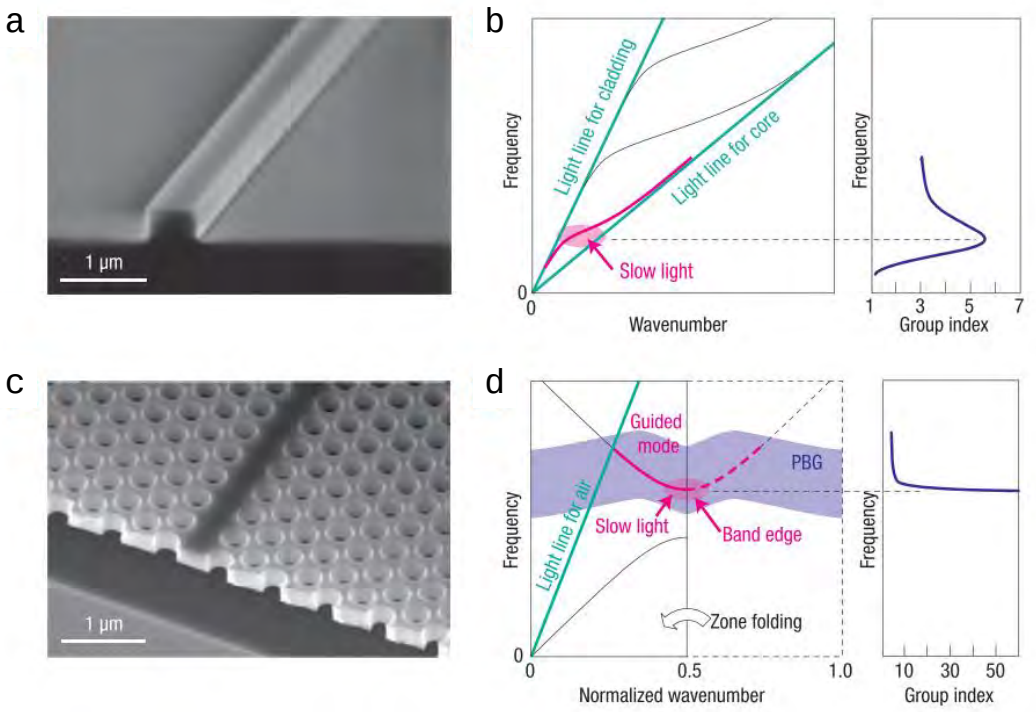

Figure 2.10: Observation of slow-light in photonic waveguides. Dispersion diagram and the group index characteristics for a photonic-slab waveguide (a) and photonic-crystal waveguide (c) fabricated on silicon are shown in (b) and (c) respectively. Image taken from [30].

diverges and gives us an estimation of the slow down factor. The structure can be further modified to have low group velocity and strong dispersion over large bandwidths. This can be done by considering a standard W1 photonic-crystal waveguide where there is an additional interaction mechanism because of the periodic structure and dispersion diverges to infinity at the band-edge where slow-light can be observed [30].

A number of effects observed in optical waveguides can be enhanced by the slow-light phenomenon [61, 86, 87]. The electromagnetic wave interacting with the material has more time, which means that the interaction strength between light and matter increases. This can be used to enhancing a number of linear and non-linear effects such as enhanced interferometers [87], mesoscopic self-collimation [88], spontaneous four-wave mixing [89], single-photon emission [32] and photon entanglement [90].

Slow-light for chiral quantum optics

Another line of research has focused on exploiting slow-light effects to increase the local density of optical states towards manipulation and control of light in quantum photonic systems [91]. Photonic-crystal waveguides have been employed in studies of chiral quantum optics where the main goal is to achieve direction-dependent propagation, where the local polarization of light is locked to the direction of propagation [4]. This can be achieved by maximizing the circular local density of optical states in a given medium. To this end, the glide-symmetry waveguides, in which the photonic lattice on one side of the waveguide core is shifted by half a lattice constant along the waveguide axis [53], has been shown to be very beneficial [32]. Although any confinement of light to waveguides such as W1 waveguides results in local points with some degree of elliptical or circular polarization [92], the glide symmetry generates points with local circular polarization in the regions with a slow-light-enhanced local density of optical states. A key figure of merit for chiral quantum-optics is the directional β-factor, which describes the fraction of emission events that end up in one particular direction and mode relative to the emission events into all modes. Directional β-factors of $\beta \gtrsim 98\%$ have been demonstrated in glide-symmetric photonic-crystal waveguides [32]. Glide-symmetric waveguides have been the subject of theoretical studies due to their interesting properties with regards to suppressing out-of-plane scattering [23] and their photonic spin-orbit interaction [24]. The experimental reports on glide-symmetric waveguides are limited [25], and the group velocity and its dispersion, which play a most crucial role for the chiral quantum-optical properties have not been investigated experimentally so far. More on glide-symmetry waveguides will be discussed in the final section of this chapter.

2.4 Limitations of slow light in photonic crystals

Though photonic crystals have established themselves as a reliable platform for slow-wave related applications, they still suffer from undesirable features. Numer-

ous studies on slow-light transport in photonic crystals have shown that surface roughness and defects arising due to unavoidable fabrication imperfections can have a negative impact on the propagation of light [61, 93, 94], even for nanometer-scale imperfections. As light is slowed down, the increased sensitivity to disorder leads to different scattering processes and hence Anderson localization [95]. Out-of-plane scattering, in-plane lateral scattering, backward scattering, and intermodal scattering are few mechanisms that contribute towards the total loss. While backward scattered waves adversely affect transmission and introduce undesirable losses, the formation of random localized modes around these nanoscale imperfections limits the functionality of slow-light devices [96]. It is also known that disorder shifts the spectral position of the optical devices [97]. In the following sections, we briefly understand the role of disorder in slow-light photonics and ways to overcome some issues.

2.4.1 Role of disorder

The effect of a disorder or defect can be best captured via coupled mode theory, which investigates the superposition of different modes via a disorder in the waveguide [98]. In the vicinity of a nanoscale defect along the waveguide, the translational symmetry would be broken and no guided mode can be supported in general. The presence of the defect would lead to the mixing of the guided modes inside the waveguide, hence the scattering of the modes into other modes. In other words, the modes get scattered in the presence of a defect and instead of a propagating mode we now have forward and backward propagating modes emerging from the disorder. This uncontrolled scattering is detrimental to the transport of light waves and can degrade the performance of the photonic crystal structure.

It has been well established that the lithography process causes nanometer-scale imperfections in the crystal structures. This surface roughness causes light to scatter in all directions leading to propagation losses. The main scattering mechanisms contributing towards the losses are out-of-plane scattering and backward scattering. Considering that the vertical symmetry is still intact, the out-of-plane scattering leads to losses proportional to $1/v_g$. On the other hand, loss due to the backward

propagating modes is more dispersive and varies as $1/{v_g}^2$ and is considered as the dominant factor in the total propagation loss [94, 96]. In other words, slower the light propagates, the larger are the propagation losses. Since their contribution towards the total loss is superior, much efforts have been dedicated to realizing backscatter-immune optical waveguides. A number of approaches have been proposed to overcome this limitation, but none seem to offer a practical solution like photonic topological insulator.

A perspective on topological insulators

The search for robust waveguides that are immune to backward scattering has led researchers to the exotic field of topological photonics. Photonic topological insulators are a photonic analogue of electronic topological insulators. These are materials which are characterized by a bulk band-gap, but can support surface states that cross the bulk band-gap; meaning that current can flow along the surface but is restricted inside the bulk. The amazing property of these surface states that exist in the middle of the bulk band-gap is that they are immune to any form of scattering and are highly directional. This property makes these materials robust since no electron deviates during its propagation. This was first observed in quantum Hall effect, where geometry-insensitive Hall resistance was measured with high accuracy in two-dimensional systems [99]. The attempt to realize an equivalent topological system without using an external magnetic field led to new physics where edge states are protected by virtue of a strong electron spin-orbital interaction instead of an external field [100].

Haldane proposed bringing this topological physics which is very robust into the context of photonics [101,102]. However, there was a fundamental difference between the two realizations. Electrons are fermions that interact with each other under the influence of strong magnetic field, while photons are neutral bosons that do not interact. The main idea was to take a photonic crystal that is made out of a material which has a magnetic response. This breaks time-reversal symmetry and gives the necessary conditions for the realization of topological insulators in optics. Soljačić and group realized one-way propagation in the microwave regime

where a strong magnetic response can be found [103]. For optical frequencies, the magnetic response is quiet weak and hence we cannot strongly break the time-reversal symmetry [4]. Another method had to be devised to realize topologically protected one-way propagating modes for wavelengths on the scale of a micron.
This launched new proposals to bypass time-reversal breaking to be able to realize topological protection at optical frequencies [104–106]. The flexibility and diversity of photonic crystals make it possible to observe these exotic states with light [107, 108]. In one realization, geometry or the topology of photonic structures are exploited to control and shape the behavior of light [106, 109]. Here, regions of two distinct topologies with opposite band properties are realized by rearrangement of structural geometry. The interface between these two topologies causes the bands to cross over supporting chiral edge-states which are orthogonal and bidirectional [5]. In other words, the doubly degenerate crossover point is said to be immune to certain kinds of disorder and strongly protected by the topology of the photonic crystal structure. In another system, similar topological properties have been realized by breaking parity symmetry [110]. These kinds of systems can be considered as a possible contenders for generating slow-light which is immune to backward scattering [111].

2.4.2 Impact of Anderson localization of light

Another important consequence of disorder on the transport properties of light is the formation of random localized modes. From condensed matter, we know that for a regular crystal lattice, the Bloch waves fills the entire system depending on the periodicity. Philip Anderson showed that solving the eigenfunctions of a disordered system, the Bloch waves become localized [112]. In other words, the diffusive transport that existed in the random potential suddenly comes to a standstill and conductivity drops. The conductance becomes zero if the disorder is increased beyond a certain value. The wave nature of the electrons is the driving force behind

[4] There are devices where time-reversal symmetry can be broken (optical isolators), but they are typically few centimeters long and impractical with photonic crystals.

[5] These states posses certain properties similar to that of electronic topologial insulators.

the observation of Anderson localization in solid crystals. Sajeev John proposed that similar effects could be observed by characterizing classical electromagnetic waves in disordered dielectric-periodic-lattices [42]. Light exhibiting strong localization under the condition of strong scattering led to a new fundamental phenomenon in classical optics.

Although current fabrication methods have matured tremendously, there is always some finite residual imperfection in real structures. Photonic nanostructures are sensitive to these imperfection as enhanced multiple scattering in these systems leads to backscattering and strong Anderson localization. In one-dimensional waveguide systems, these localized modes would remain confined around the defect and the propagation would come to a halt. Irrespective of the disorder strength this would be the case for an infinitely long system, but in finite-systems this crossover is determined by a key parameter called localization length, ξ, or backscattering mean-free-path. There have been a number of attempts to measure the localization length, which shows a signature of the onset of Anderson localization [113–115]. However, these results do not include different strengths of disorder [6]. Anderson localization is a statistical quantity and hence require confirmation through an ensemble of sufficiently large random disorders. Although Anderson localization is not feasible for device applications which involve propagation of light, it has found applications in cavity-quantum electrodynamics where cavities and random lasing form the main ingredients [116].

2.5 Glide-symmetry waveguide

Dispersion engineering allows us to modify the optical properties of photonic crystals to cater to applications ranging from optical communication to quantum electrodynamics. At the same time, devices also suffer from various sources of losses which ultimately degrades their performance. Improving the performance and robustness of a functional photonic crystal is the cornerstone of any waveguide research and

[6] localization becomes insignificant when the structural imperfections are smaller than the wavelength.

this led us to a new design called the glide-symmetry waveguides. In this section, we will try to get an overview of this design and its practicality in the field of quantum electrodynamics.

Coupling an atom-like system to a one-dimensional waveguide can greatly enhance the interactions between matter and light. Quantum electrodynamics studies the dynamics of such interacting systems at the most fundamental level. This theory has proved to be accurate and has been used to demonstrate single-photon emission [32], photon non-linearities [117] and other quantum phenomena for a wide range of quantum optics applications. An interesting concept that has caught the attention of many researchers is the field of chiral light-matter interaction. The ability of nanophotonic structures to couple differently to left- and right-mode excitations is quite remarkable. This interaction depends on the coupling strength between spin and orbital angular momenta [118]. Under specific conditions, this phenomenon can also become unidirectional i.e, the emit photons in specific directions.

An important parameter central to this concept is the ability to maintain circular polarization along the plane of the waveguide. If a circularly polarized emitter is placed inside such a waveguide, at a position where the local polarization is also circular, then the emitter will emit only along one direction. One of the main requirement for realizing in-plane circular polarization in a one-dimensional waveguide is that the longitudinal component of the mode must be out of phase by $\pi/2$ compared to its transverse counterpart. It has been shown that photonic crystal waveguides with glide-plane symmetry exhibit a well preserved circular polarization along the waveguide plane [119]. Deterministic directional emission of upto $\beta \gtrsim 90\%$ has also been demonstrated in this design [32].

2.5.1 Design considerations

One of the main objectives of this thesis was to fabricate these devices on silicon and characterize their optical properties for chiral applications. For our waveguide design, we follow the work of Mahmoodian et al. [119] who have shown that the group index, $n_g = c/v_g$, can be enhanced by about an order of magnitude compared to previous experimental state of the art [32]. Mahmoodian et al. introduced a

series of transformations and structural modifications to the geometry of a regular W1 photonic-crystal waveguide.

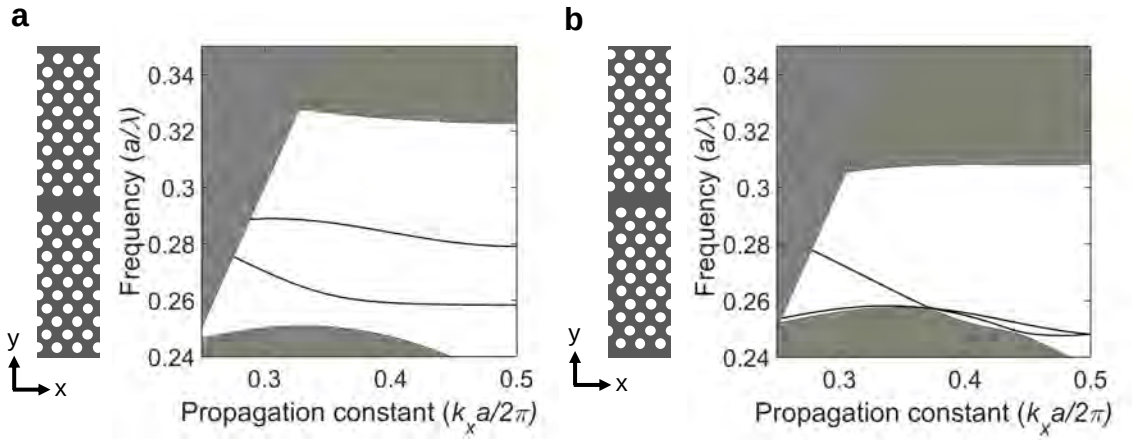

Figure 2.11: Waveguide dispersion diagram for photonic crystals.
(a) Primitive cell of a regular W1 photonic-crystal waveguide and the corresponding dispersion diagram highlighting the two waveguide modes. (b) Primitive cell of a shifted photonic-crystal lattice introducing the glide symmetry. The corresponding dispersion diagram highlights the formation of crossover points at $k_{\mathrm{x}}a/2\pi = 0.37$ and $k_{\mathrm{x}}a/2\pi = 5$.

The glide symmetry is introduced by shifting one side of the photonic-crystal cladding by half-period. This directly leads to the formation of pairwise degeneracies of the waveguide bands at the Brillouin zone-edge due to the non-symmorphic nature of the glide symmetry [53]. Unlike the W1 waveguide modes, these modes cannot be strictly considered as even or odd, but a linear combination of both with closely related symmetric properties [53]. The modes also crossover at $k_{\mathrm{x}}a/2\pi = 0.37$ which can create issues with the directionality in the system. We can also observe that the fundamental mode has been shifted to lower frequencies at the crossover point, which can lead to significant leakage into the cladding. The dispersion diagram of the transverse-electric modes of a W1 waveguide and glide-symmetry waveguide are shown in Fig. 2.11, which has been obtained with the MPB software package [120]. It has also been shown that the out-of-plane optical radiation losses can be significantly suppressed by spatially translating one side of the photonic crystal by half a lattice constant [23, 121]. This is because of the elimination of the Fourier compo-

nents of the radiation peaks. It has been shown that this geometry can also be used for building edge-emitting photonic crystal lasers [122].

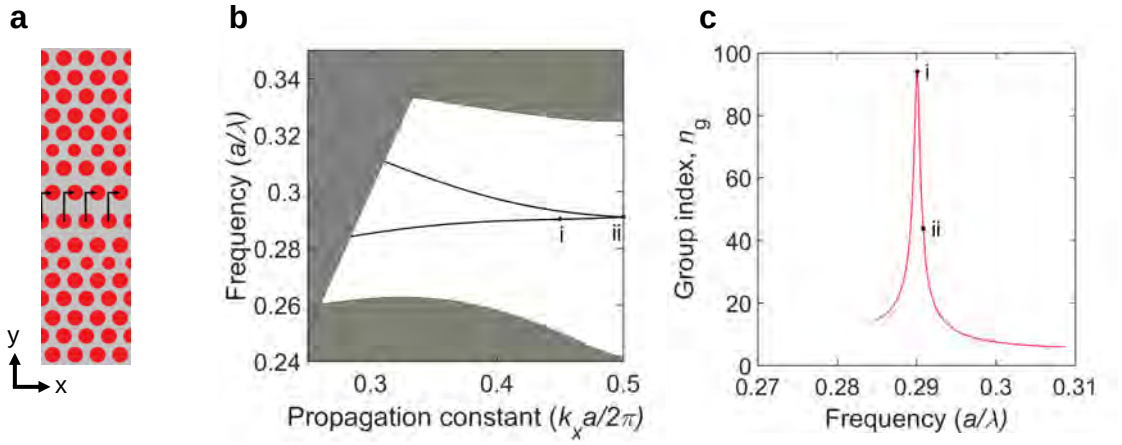

Figure 2.12: Glide-symmetry waveguide. (a) The unit cell of a glide-symmetry waveguide indicating the glide-plane along with shifts in radii and position of air-holes around the waveguide section. (b) The dispersion diagram of a glide-symmetry waveguide illustrating the single-moded waveguide modes. (c) The group index of the corresponding dispersion is plotted as function of frequency. The two main features of interest are also highlighted, where (i) is the slow-light region which peaks at $n_g = 94$, and (ii) is the band crossing at the Brillouin-zone edge.

In order to ensure that the modes are single moded and do not leak into the slab modes, significant modifications were made by employing dispersion engineering techniques like changing the radii and position of the holes around the waveguide section [62]. First, the effective index of the waveguide mode is lowered by decreasing the width of the waveguide section to $0.75w$. This should bring the fundamental mode to higher frequencies [50]. Second, the three rows of holes in both claddings near the waveguide section are shifted and their radii are modified, which increases the group index at certain points and ensures that the spectral features of interest are single-moded below the light line within the entire bandwidth of interest. The two points of main interests are labeled (i) and (ii) in Fig. 2.12b and denote (i): the point of maximum group index, which peaks at $n_g = 94$ and (ii): the band crossing point at the Brillouin-zone edge. We note that although the degeneracy at the Brillouin-zone edge is also a salient feature of interface states between topologically different

materials [123], the origin in our case is entirely different: the degeneracy is rooted in the non-symmorphic character of the glide symmetry and the two claddings are not only topologically trivial, they are also identical.

This emphasizes the engineering potential of photonic crystals because of the various degree of freedom available to design the structure. A structure which is designed for unidirectional emission can be used for interfacing spin and photons, and spin-photon entanglement. With the aim of realizing chiral properties on a chip, several correlated photon pair generation experiments based on slow-light enhanced spontaneous emission have already been reported [32]. These experiments achieved a significant enhancement of photon generation compared with conventional single-photon sources based on trapped atoms [124]. Here, we fabricate and investigate the slow-light properties of the glide-symmetry waveguide which could possibly be useful for integrated quantum photonics, where quantum-information processing functions are integrated on an optical waveguide.

3

Waveguide coupling

A key factor in realizing integrated photonic circuits is the compact size and submicron scale geometries of optical components. Coupling of light into these optical structures from an external source has been a challenge and hence is an active area of research [52, 125–127]. Mode mismatch and index mismatch are the main limiting factors to the efficient coupling of light. The size mismatch between the external optical fiber and the photonic structures can be very large resulting in coupling losses (Fig. 3.1). The index mismatch can further deteriorate the coupling process. It is necessary that light from an optical fiber is coupled into the photonic structure without losing much of its optical power and over a wide bandwidth. For slow-light devices, where the group index can reach high values, this issue can be far more pressing [22, 128]. Large impedance-mismatch at the coupler-waveguide interface can hinder efficient coupling of light into the slow-light regime and scatter light into different lossy modes.

Conventionally, light is routed between various optical components using rectangular channel waveguides (Fig. 3.2). These waveguides are characterized by a high index-contrast between the guiding material and the surrounding material, which facilitates efficient confinement of light. A difference in group indices of optical components in the circuit can create interfaces with poorly matched modes. These interfaces act as scattering points for the propagating mode. Every optical component behaves like a stand-alone resonator and resonates with its own Fabry-Pérot frequency. This further causes interference of different resonant frequencies generating spectral features that are difficult to interpret in an experiment.

It has also been shown that a more efficient coupling can be obtained by the spatial

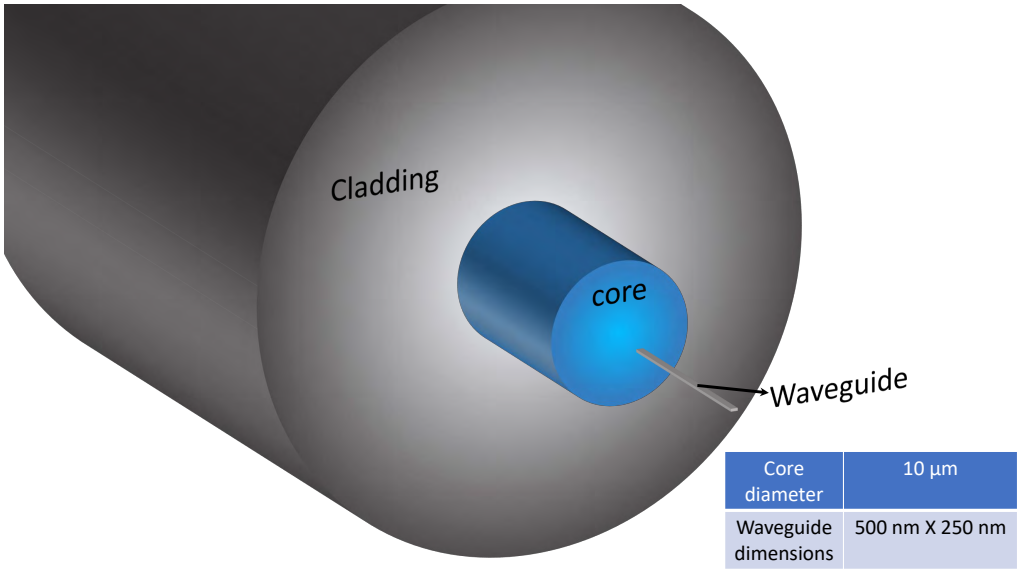

Figure 3.1: Size mismatch comparison. A comparison of the dimensions of a single mode fiber and a channel waveguide. The core width has a diameter of 10 µm while the waveguide geometry has dimensions of 500 nm x 250 nm.

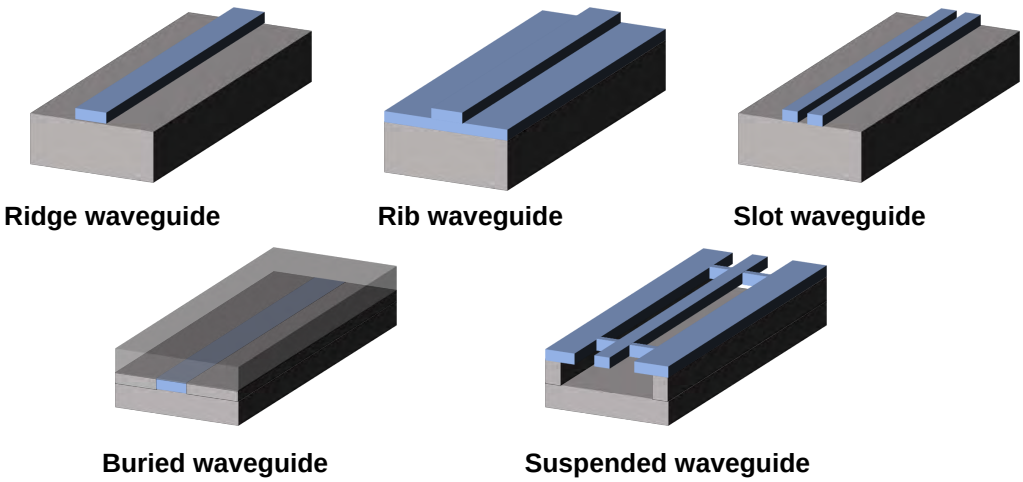

Figure 3.2: Optical waveguides classified according to different geometries. Different forms of two-dimensional channel waveguides can be conceived for various applications.

variation of refractive index of the interfacing material. Several designs have been proposed such as periodically-segmented waveguides [129], inverse-tapered waveguides [130], and adiabatic waveguides [52]. These designs are also simple to fabricate, as they involve small modifications to the waveguide geometry and the same fabrication process techniques. In the case of photonic crystals, it has been shown that the terminations of crystal sites at the coupling interface can also influence and minimize the impedance mismatch [131, 132].

Different characterization setups require modified coupling strategies and in our case, vertical free-space coupling was the preferred choice because of the out-of-plane scattering from coupler gratings. In the final section of this chapter, we also discuss a mode converter. The mode-converter project was conducted in collaboration with Accelink, Denmark, where the main goal was to develop a planar mode converting structure for coupling the light in and out of a silicon waveguide on a silicon-on-insulator (SOI) platform. I perform numerical simulations to calculate different conditions for single-mode propagation of light.

3.1 Grating coupler

One of the main objectives of this thesis is to characterize and quantify the slow-wave nature of light in glide-symmetry waveguides. The simplest technique to measure the group velocity is to construct a cavity in a one-dimensional Fabry-Pérot resonator setup (Fig. 3.3). The strongly reflecting boundaries cause light to resonate back and forth resulting in the formation of standing waves of different orders. The group index properties can be extracted from the free spectral range ($\Delta\lambda_{\mathrm{FSR}}$) of the fundamental mode Fabry-Pérot oscillations which depend directly on the length of the cavity. The free spectral range in terms of wavelength is given by the equation,

$$\Delta\lambda_{FSR} = \frac{\lambda^2}{n_g L} \tag{3.1}$$

Here, n_g is the group index of the propagating medium, λ is the free-space wavelength, and L is the total distance covered by light in one round trip around the cavity length, l. The physical structure of a one-dimensional waveguide resonator

imposes boundary restrictions which supports only a limited number of guided longitudinal-modes.

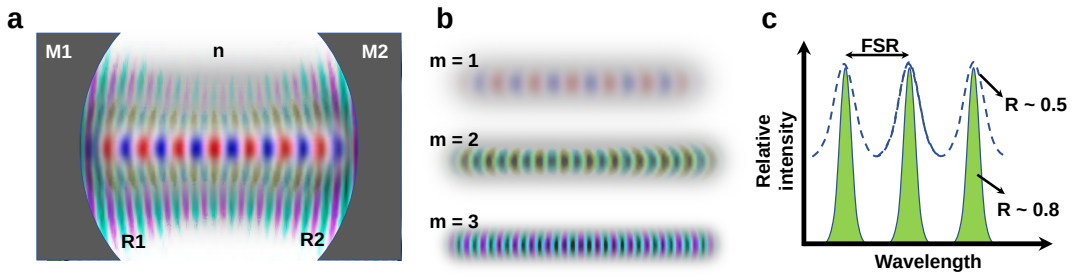

Figure 3.3: Schematic of a Fabry-Pérot resonator setup. (a) Illustration of a simple optical resonator with the reflective mirrors having coefficients R_1 and R_2. (b) Some stable standing-wave-patterns of different wavelengths are formed because of multiple reflections. (c) The intensity of the transmission through the resonator. R is the reflectance coefficient of the mirror. The lower the value of R, the higher are the losses, which will result in broadening of the transmission peaks.

This implies that we should try to avoid cascading many optical components if we want to characterize a stand-alone resonator. This would ensure a pure spectral signal arising from the waveguides under consideration. Hence, we had to rely on a more primitive method to probe these resonators.

3.1.1 Facet-coupling

For the first design, we used the surface coupling approach, where a one-dimensional photonic-crystal waveguide is terminated at both boundaries creating end-facets. Light from an objective is impinged onto the edge of the waveguide structure, which is then scattered in all directions. Few scattered wavevectors are coupled into the waveguide and transmitted. However, light propagating in the waveguide has to make a substantial change in direction towards the objective for measuring. This is unreliable and the measured signal has a reduced extinction ratio. Few measurements can be seen in Appendix B, Fig. B.1. Another major drawback in this method is that these facets forms a strongly reflecting mirror because of the high index-contrast between silicon and air. This means that the transmission spectra which scatters at the output end is attenuated which further deteriorates the finesse of the transmitted signal [133].

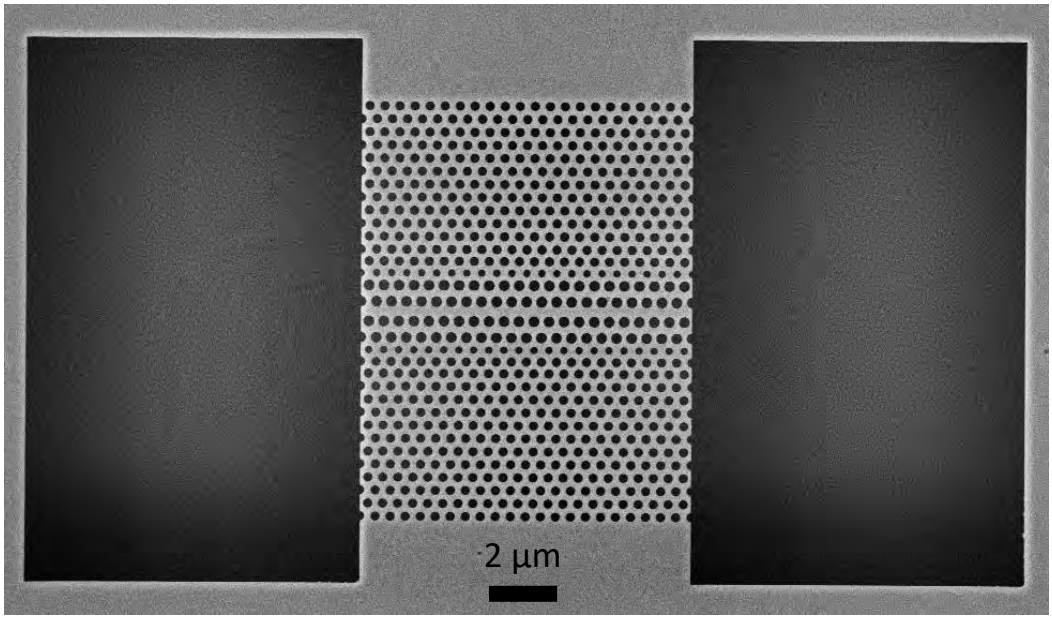

Figure 3.4: Terminated-facet coupling. A scanning electron microscope image of a 10 µm long glide-plane waveguide resonator with terminated ends. The underlying oxide layer is chemically etched leaving behind a silicon-membrane structure.

3.1.2 Circular coupler gratings

To further improve coupling and scale up the finesse of the transmitted signal, periodic gratings were appended to the terminated ends. These grating couplers are similar to the design proposed in [134]. They are based on a second-order Bragg gratings and consists of semi-circular rings with a pitch of $\lambda_0/(2n)$. This causes destructive interference in the direction of propagation and scatters light out of the plane. Using this circular grating, we can inject light into the resonator from the top using an objective setup. Via the same objective, the on-chip transmission can be probed from the other end of the cavity. However, the emitted field does not have a Gaussian profile but a complex field distribution. This means that there exists a mode mismatch with the optical fiber and hence chip-to-fiber coupling can be challenging. The grating shown in Fig. 3.5 is designed for operating in a spectral bandwidth of 100 nm around 1550 nm, which is where the waveguide modes were designed for transmission.

The goal is to probe the transmission in a cavity resonator with high finesse. This requires a fine balance between the transmission and reflection coefficients at the mirror interfaces. If the reflection coefficient of the mirror is very high, then the cavity cannot leak out any photons. At the same time, if the transmission through the mirror is high, then most of the photons leak out and no standing waves are formed. It is hence desirable to include a mirror with transmission and reflection properties, such that few photons leak out of the resonator structure, while still being able to form standing waves inside the cavity. The circular grating couplers have a rather low coupling efficiency and high reflectivity, which is just sufficient for building resonator devices. At the same time, they direct a sizable amount of light out of the chip plane, which is useful for transmission measurements [134].

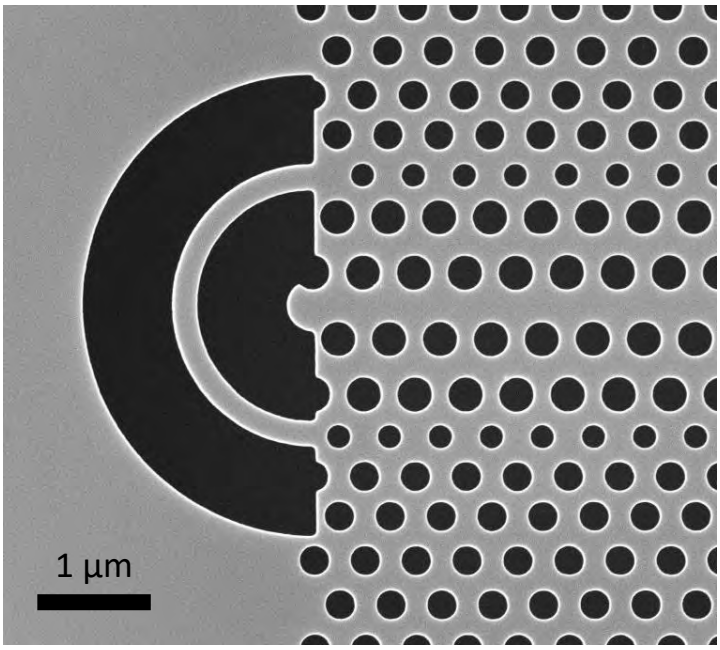

Figure 3.5: Circular grating coupler design. A scanning electron micrograph of a circular grating coupler appended to a glide-symmetry waveguide. The asymmetry of the glide-plane causes the first layer of the circular grating to slightly distort. This distortion is absent in circular gratings interfaced to a standard W1-waveguide.

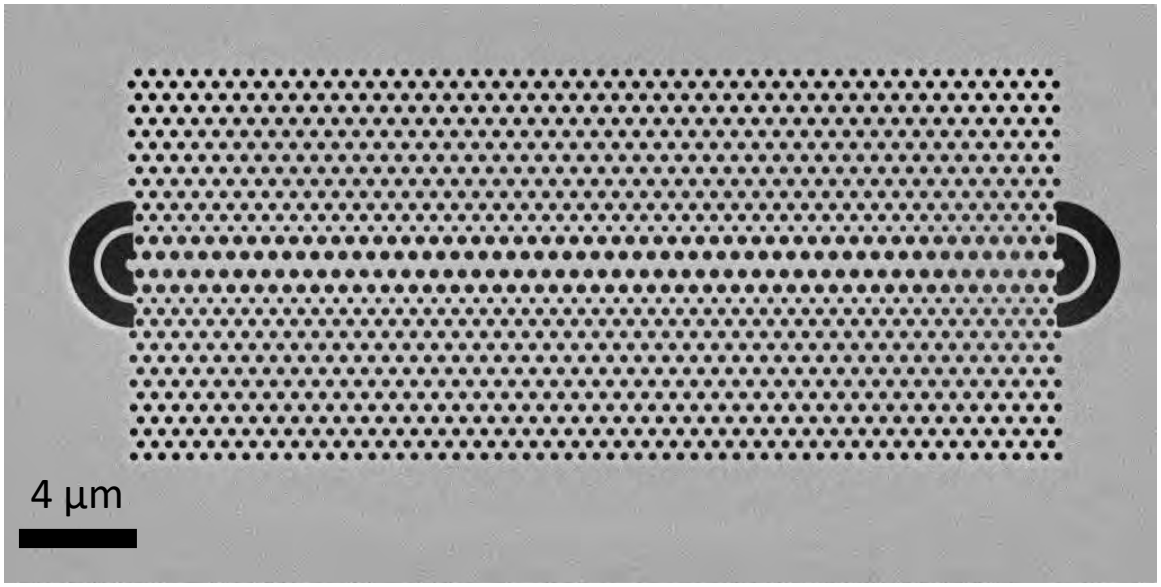

Figure 3.6: Glide-symmetry waveguide resonator. A scanning electron micrograph of a 30 µm long glide-symmetry waveguide in a resonator setup, interfaced with in-out circular grating coupler design.

3.1.3 Orthogonal coupling design

A third coupler design had to be fabricated to study the on-chip propagation of light in millimeter-long glide-symmetry waveguides. Here, the Fabry-Pérot fringe contrast is not important for the analysis, and hence other elements have been added. As shown in Fig. 3.7, this circuit consists of suspended channel-waveguides or nanobeams, photonic crystal waveguide, and the in-out grating couplers. Any photonic-crystal design can be connected to the circular gratings via the suspended channel-waveguides. The waveguides are suspended with the help of tethers which are positioned 30 µm from each other. The entire structure is fabricated on a suspended membrane to maintain horizontal symmetry for the propagating mode in the waveguide. An interesting feature of this circuit is that the excitation and collection grating couplers are positioned orthogonal to each other. This configuration prevents the objective from directly capturing stray light that scatters from the input grating and stray oscillations arising from undesirable cavities [1].

When light starts to propagate from access waveguides into the photonic crystal section, it experiences a sudden change in the group index at the interface for a wide range of frequencies. This abrupt change in the group index stems from the difference in their energy densities and results in a large impedance mismatch at the interface [29]. Consequently, a large amount of energy is reflected and scattered at the interface.

There have been several proposals to overcome this issue: based on Adiabatic transitions [132], optimised hole terminations [126], and fast-light tapers [135]. Among these methods, the fast-light tapers has been found to be the most effective method to couple light into the slow-light region. This involves introducing an additional photonic-crystal section of 5 periods with the lattice stretched by a small factor of $1.07a$. This has the effect of shifting the dispersion curve to lower energies. Hence, for a given frequency, the group index of the fast section is lowered, which ensures that the impedance mismatch between the access waveguide and the stretched

[1] When the laser penetrates through the silicon device layer (250 nm) and impinges on the silicon substrate, it behaves like a resonator and scatters light in all directions.

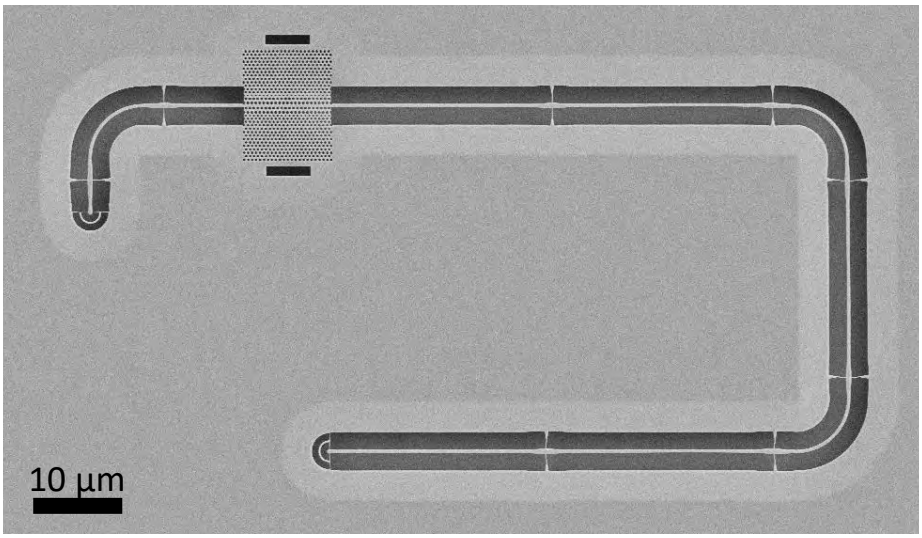

Figure 3.7: Orthogonal coupling scheme. A scanning electron micrograph of a photonic circuit used to measure transmission in a 10 µm long photonic-crystal waveguide. The main components are suspended channel-waveguides, photonic-crystal waveguide, and circular grating couplers. The couplers are positioned orthogonal to each other.

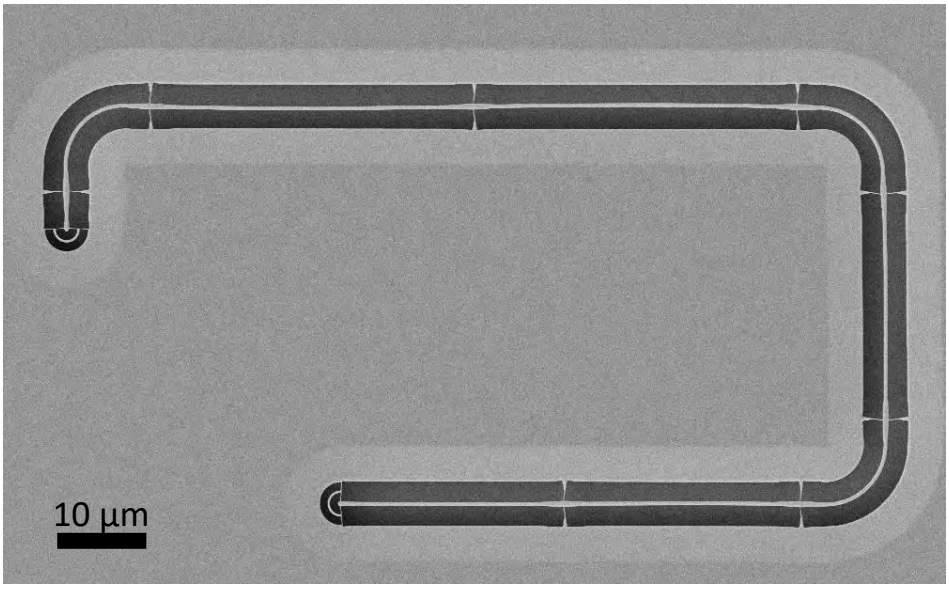

Figure 3.8: Orthogonal coupling scheme. A scanning electron micrograph of a suspended waveguide used as a reference to measure transmission in a 10 µm long photonic-crystal waveguide. The length of the suspended waveguide-section remains unchanged, while the length of the photonic-crystal waveguides can be varied.

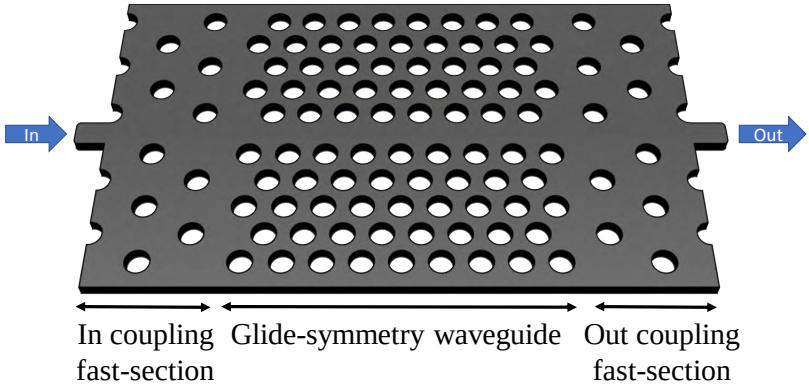

Figure 3.9: Fast-light interface design. An illustration of a regular glide-symmetry waveguide lattice coupled to a stretched glide-symmetry lattice at both ends.

section of the waveguide is reduced (Fig. 3.9). A new junction is formed at the stretched-regular interface, where for a given frequency, the group index of the stretched lattice is smaller than the group index of a regular lattice glide-symmetry design. This minimizes the degree of impedance-mismatch between the two boundaries ensuring an efficient evanescent coupling [136, 137].

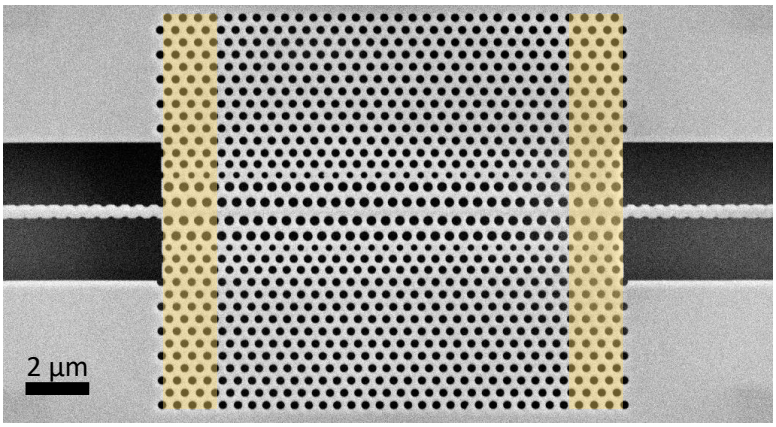

Figure 3.10: Fast-light taper section. A scanning electron micrograph of a fast-section coupled to a 10 µm long glide-symmetry waveguide on both ends. The fast section is highlighted in yellow and has 5 periods of photonic crystals, stretched by a factor of $1.07a$.

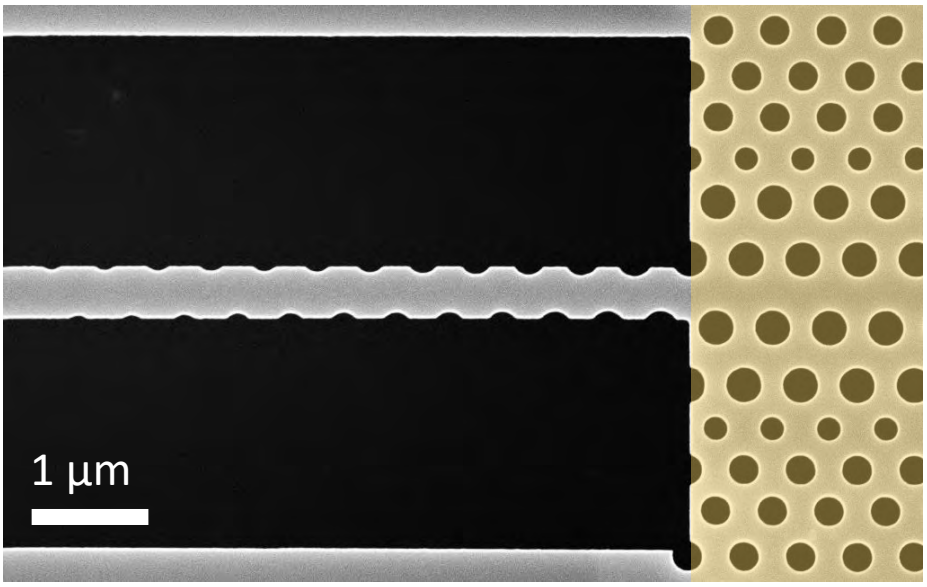

Figure 3.11: Glide-symmetry waveguide mode converter. A scanning electron micrograph of a mode converter illustrating the circular indentations which assists the mode transition from a rectangular channel-waveguide to the fast-section of the glide-symmetry waveguide.

For the glide-symmetry waveguides, special considerations have to be taken since the upper and the lower photonic crystal sections are not mirrored. In order to facilitate a smooth transition from access waveguide into the fast-section of the glide-symmetry waveguide, a mode adapter was proposed [119]. Fig. 3.11 shows an electron micrograph of a mode adapter which couples light from the access waveguides into the fast-section of a glide-symmetry waveguide. This has been realized by removing part of the dielectric on both sides of the access waveguide which would break the mirror symmetry along the x-direction. The radii[2] of the holes removed on the access waveguides changes adiabatically from $R_1 = 0.23a$ to $R_2 = 0.35a$. This manipulates the flow of light and introduces an adiabatic transition from symmetric to non-symmetric mode profile. The modified access waveguide is then connected to a stretched glide-symmetry design spread over 5 periods.

[2]The radius of the first row of holes in the glide-symmetry waveguides is $R = 0.35a$.

3.2 Mode converter

Historically, silica has been the preferred material for constructing optical interconnects for integrated optical circuits [18]. They showed negligible coupling losses because their geometry matched with the core size of the single-mode optical fiber and had similar refractive indices. The development of CMOS fabrication pushed silicon-on-insulator (SOI) technology into the foray and waveguides made from silicon were found to be more promising [138]. The waveguides could be made more compact and the high-index-contrast ensured tight confinement of the propagating mode. However, these devices suffer from high coupling losses because of the mode size mismatch between the nano-scale silicon waveguide and the single-mode fiber and this was unacceptable for practical purposes.

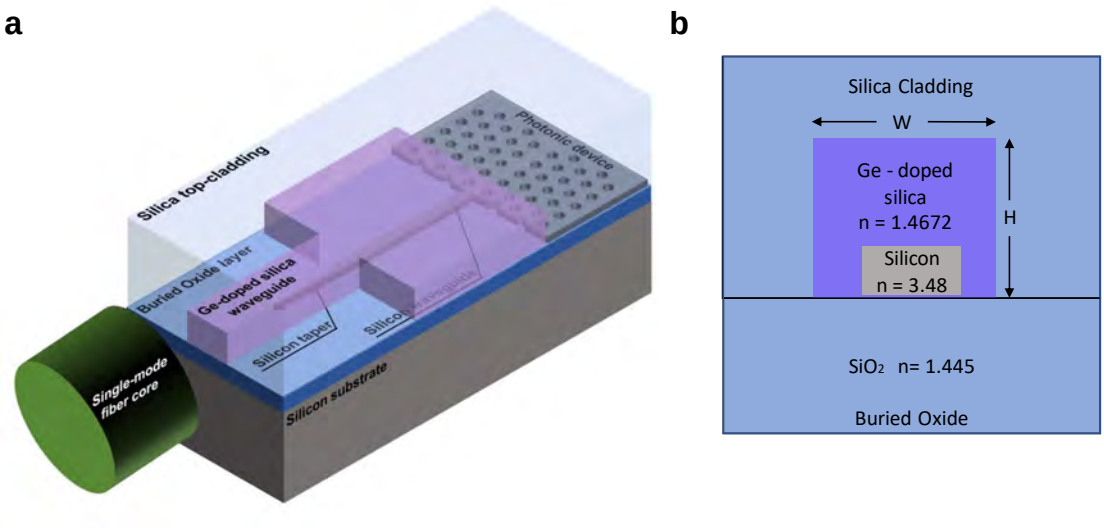

Figure 3.12: Schematic view of the mode converter illustrating various components. (a) The mode in the photonic device propagates through the waveguide section and is adiabatically transformed to that in the germanium-doped silica waveguide which has comparable mode size as that of single-mode fiber. (b) Cross-section view of the various layers of a mode converter. The width of the silicon waveguide changes adiabatically as it proceeds from rectangular to tapered section.

An interface is, therefore, necessary to fulfill this gap in mode mismatch. A mode converter solves this issue and has been studied by several groups. Lensed fiber,

inversed taper [130], and adiabatic taper [52] are few configurations that have been proposed to realize a smooth transition. However, these techniques are not suitable for high volume production because of costs, packaging issues, and fabrication limitations. Accelink Denmark A/S has many years of experience in processing and fabricating silica waveguide based products. Here, they were keen on developing a silicon-silica mode converter to couple light in and out of their SOI-based planar optical products. The challenge was to optimize the design parameters and optimize a robust fabrication recipe for high volume production. The preferred lithography system was deep-UV stepper, which is designed for 150 mm and 200 mm wafers and has a throughput of up to 90 wafers per hour.

The mode converter structure was based on a tapered design proposed by Jia et al. [139]. This is shown in Fig. 3.12a. The entire structure was proposed to be fabricated on an SOI platform which has a device thickness of 260 nm and a buried oxide layer of 3 µm. It consists of four main components: photonic device, rectangular channel-waveguide, tapered channel-waveguide, and the germanium-doped silica waveguide. The idea was to couple light from a photonic device into a single-mode fiber by transforming the mode adiabatically. This is done by employing a transitioning structure that expands the ultra-small mode in silicon to a comparable size in germanium-doped silica waveguide. A taper structure that adiabatically narrows the silicon waveguide from 500 nm to around 100 nm is enclosed by a 4.4 µm × 4.4 µm germanium-doped silica waveguide. The tapered geometry causes the mode to leak out into the doped-silica waveguide region until the high-index silicon can no longer support the propagating mode. The taper region acts as a transition section between silicon and ge-doped silica. The entire structure is buried in a 12 µm thick silica cladding which acts as a protective cover. The germanium-doped silica has a refractive index which is 1.5% higher than that of silica, and hence the mode is well confined in the doped-silica region.

There are a few considerations that need to be addressed. The dimension of the tip of the taper is usually limited by the resolution of the lithogrpahy tool. In this case, since the preferred choice of lithography equipment was deep-UV stepper, we had to determine the minimum dimensions of the tip that would support a

smooth transition without causing much losses. The mode-mismatch between the silicon-taper and doped-silica waveguide would give us a quantitative measure of the coupling efficiency of the taper structure. This is calculated by using the following equation [139].

$$\eta(dB) = 10\log\left(\frac{|\int E_1^* E_2 dA|^2}{\int |E_1|^2 dA \int |E_2|^2 dA}\right) \tag{3.2}$$

where E_1 and E_2 are the mode field profiles in silicon waveguide and doped-silica waveguide respectively. The critical parameter is the dimensions of the tip of the taper section and their effects to the coupling efficiency is shown in Fig. 3.13. We can see that a coupling efficiency of more than 90% can be achieved with a taper width of 100 nm and quickly reduces to $\approx 2\%$ for a taper width of 200 nm.

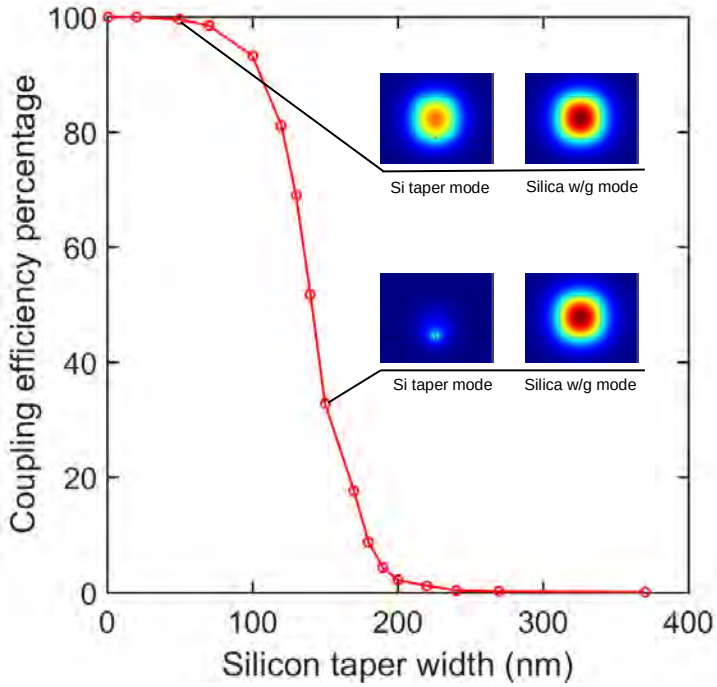

Figure 3.13: Simulated coupling efficiency. Coupling efficiency for a silicon taper and doped-silica waveguide is plotted against silicon-taper widths. Inset images shows the mode profile for silicon taper and doped-silica waveguide, simulated for different widths of silicon taper.

We also had to ensure that no higher order modes were coupled into the silicon waveguide. This was verified by studying the first two modes for various core-

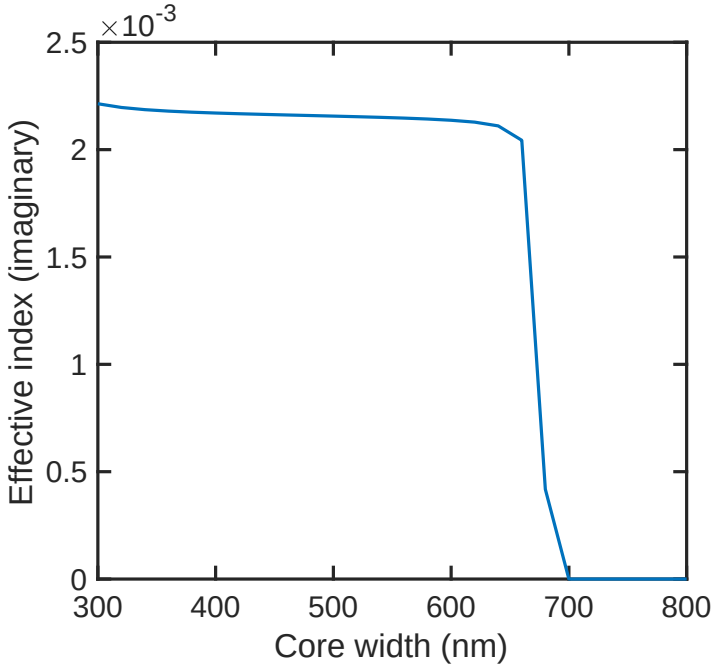

Figure 3.14: Single-mode condition. The imaginary part of the effective mode-index for a higher-order mode is plotted for different widths of silicon channel-waveguides. A non-zero imaginary part indicates that the mode is lossy and cannot be supported by the channel-waveguide.

widths of silicon channel-waveguide. For the higher-order mode, the imaginary part of the effective mode-indices are plotted as shown in Fig. 3.14. From this, we can determine the cutoff at which the higher order mode becomes significant. Below this cutoff ($Si_{width} = 680\,nm$), the higher-order mode is very lossy (as can be seen from the imaginary component of the effective index) and even if the mode exists, it cannot propagate and dissipates into the underlying silica substrate layer. This satisfies the single mode condition. Above this cutoff, only the real part of the effective index exists indicating the presence of higher order mode confinement.

Fabricating such a taper structure with deep-UV lithography process can be quiet a challenge. I did not get to optimizing a reproducible recipe, but there were few challenges that needed to be addressed. The critical dimension (CD) of structures that can be patterned using a deep-UV stepper is specified at around 250 nm. However, the best achievable resolution is different for each pattern type, pattern shape,

and pitch. With an alignment accuracy of 50 nm, it would be unreasonable for a single lithography step. Hence, a double exposure lithography step was proposed to overcome this issue [140].

4

Nanofabrication

As discussed in previous chapters, the glide-symmetry waveguides are intended for applications that operate at near-infrared wavelengths. The feature size of the devices intended for telecom applications is dictated by the wavelength of light and usually scales down to a few hundreds of nanometers for the c-band. This implies that the requirements on their precision are in the order of nanometer. Such stringent conditions call for a mature nano-scale processing technology, that allows for robust and repeatable processing.

Fabricating compact photonic devices on a silicon-on-insulator (SOI) platform has become pervasive across many research groups today [26]. SOI substrates with a silicon (refractive index, $n \approx 3.476$) device layer of 220 nm, and a 3 µm low refractive-index buried-oxide layer ($n \approx 1.55$) are most commonly used [96, 141]. The choice of silicon is mainly driven by advanced processing techniques, mature pattern transfer processes, and the need to work with high index-contrast material for band-gap formation. High-index dielectric materials also enable the miniaturization of optical components for various end-user applications. At the same time, removing the buried oxide layer enables the creation of vertically symmetric membrane structures and increases the vertical index contrast, thereby improving the optical mode confinement [121]. In this chapter, the basic processing techniques to fabricate photonic crystal devices are examined; and optimization strategies to achieve higher precision are discussed.

A generic framework for fabricating a photonic crystal waveguide membrane can be described by the following steps.

- Pattern generation: A lithography process is used to expose a pattern on a photosensitive resist covering the substrate. A subsequent development process creates a mask of the structures to be fabricated.
- Pattern transfer: An etching process transfers the pattern from the resist mask to the device layer.
- Membranization: Subsequent wet-etch process removes the buried oxide-layer resulting in suspended membrane structures.

This is a robust process since it gives the same results even if there are minor changes in the overall processing conditions. However, there can be variations in the thickness of the top silicon device layer in different locations on the same wafer [142]. This variation in the thickness has to be be considered during characterization since it can cause varying shifts in the operating wavelengths of the fabricated photonic crystal waveguides. A pictorial representation of the process flow used for fabricating SOI-based structures in this thesis is shown in Fig. 4.1. A detailed description of the process recipe is given in Appendix A.

4.1 Surface preparation

Since the lithography process is done in a class 10-100, ISO 9001-certified cleanroom at DTU Nanolab, the SOI wafer must be carefully conditioned before it is prepared for lithography. The most commonly found irritants are traces of dust, bacteria, oil and other organic particles. A Piranha solution is used to clean different traces of contaminants [143]. This solution is very aggressive and directly attacks organic materials and other forms of contamination. It is a mixture of concentrated sulphuric acid (H_2SO_4) and hydrogen peroxide (H_2O_2) mixed in a ratio of 4:1. This is a highly exothermic reaction and the temperature of the solution can usually exceed 100 °C. Since it is a strong oxidizing reagent, most of the traces of contaminants are oxidized,

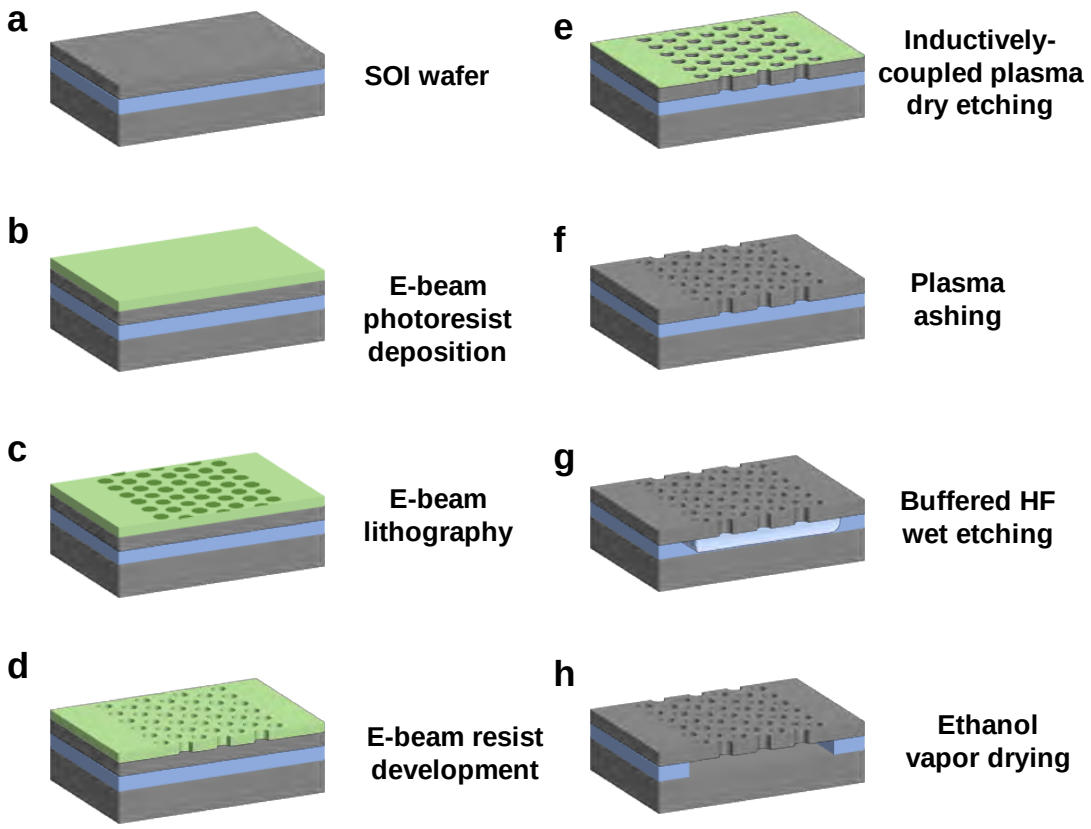

Figure 4.1: Process flow outline. (a) A 2 cm × 2 cm chip is cleaved from a thoroughly cleaned SOI wafer. (b) Positive-tone e-beam resist AR-P 6200 is spin-coated on the sample. (c) The resist is exposed at specific areas using electron-beam lithography system. d) The exposed areas on the resist is dissolved by the developer AR-600-546. (e) The resist pattern is transferred to the active silicon layer using a Bosch-process on deep reactive-ion-etching (DRIE) tool. (f) The remaining resist is stripped off using an oxygen plasma. (g) Wet etching agent buffered-HF is used to etch the underlying oxide layer. g) The sample is dried in a ethanol vapour chamber at 70 °C to reduce stress due to surface tension. This entire process was realized at the class 10-100, ISO 9001-certified cleanroom facility at DTU Nanolab.

leaving behind a reasonably clean silicon surface[1]. Using a diamond scriber, the SOI wafer is then cleaved into smaller chips of 2 cm x 2 cm, which is compatible with a particular chip cassette holder for the electron-beam lithography system.
Theses sample can collect dust and other contamination over time. This has to be removed before coating it with the electron-beam resist. The samples are cleaned by immersing it in a beaker filled with acetone for 60 s, followed by a thorough rinse in 2-propanol (IPA) solution. The acetone is a strong solvent which removes most of the contaminants. However, it leaves behind unwanted residue after drying. Hence, the acetone is further cleaned by treating it with IPA solution. The sample is then blow-dried with a jet of nitrogen gas and transferred immediately to a chip casing.

4.2 Resist preparation

The standard method for applying resist on the substrate is spin coating. This can be done either manually or using a specialized automated machine. After the chip is carefully cleaned, the positive photoresist AR-P 6200.09 (CSAR-62)[2] is applied manually using spin coating equipment. The e-beam resist CSAR-62 is characterized by a higher sensitivity and substantially improved resistance to plasma ion etch compared to regular e-beam resist like PMMA.
The chip is mounted inside the spinning chamber on a rotating holder, where a pocket of vacuum holds the sample in place. A few milliliters of resist is dispensed on the chip using a pipette, until the entire chip is covered by a puddle i.e, spread to all the corners. This is done in order to reduce the formation of edge beads on the resist film. The chip-holder is set for spinning at an acceleration of 4000 rpm and a spin speed of 3000 rpm, for 60 s inside a vacuum chamber. The photoresist forms a thin film of uniform thickness, while the excess flying off during spinning.
After spin coating, the chip is subjected to soft baking at a temperature of 200 °C for 60 s on a preheated hotplate. This evaporates most of the solvent (anisole) and

[1] It will also result in the formation of a significant native oxide layer. This will be removed during HF release.

[2] This is equivalent to the conventional e-beam resist ZEP520, but with additional polymeric groups.

solidifies the photoresist. Special care has to be taken in order to optimize the baking temperature. Higher temperatures can break down the active components leading to reduced sensitivity to electron energy.

The variable-angle ellipsometric spectroscopy (VASE) is used to measure the thickness of the thin film of resist deposited on top of the substrate. Since an SOI wafer is made up of a stack of different layers, appropriate fitting parameters is put in to get a reasonable value for the thickness of the resist. This is shown in Table. 4.1. A resist thickness of 215 nm was measured with the above-mentioned spin coating parameters.

Spin speed (rpm)	Accleration (rpm)	Thickness (nm)	Duration (sec)
3000	4000	215	60
2000	4000	275	60
1500	4000	310	60

Table 4.1: CSAR-62 resist spin parameters. Different resist thickness was measured by varying the speed of the rotating chip-holder.

4.3 Lithography

Photolithography is a standard microfabrication process used to make submicron-scale structures on a bulk substrate, or patterns that needs to be made repeatedly on wafers. Depending on the applications, the minimum-size or resolution with which patterns can be lithographed is very important. The pattern transfer process depends on two things: the lithographer agent, and the material which is used to fix the pattern over the sample. The lithographer agent will be light and the material to fix the pattern will be the photosensitive resist.

Different wavelengths from the high energy spectrum are used for optical lithography. Traditionally, ultraviolet (UV) light is the most commonly used agent for photolithography technique. The wavelength properties and characteristics of UV light make it an ideal source for sub-micron pattern generation[3]. However, owing

[3]Diffraction limit is set by $\lambda/2$, so UV has 2x resolution of red wavelength, and 4x resolution

to their longer wavelengths, fabricating nanoscale structures can offer serious challenges. The resolution of lithography process directly depends on the wavelength associated with the lithographer agent. Shorter wavelengths of light can produce sharper features. However, as wavelength decreases, the optical lithography suffers from various effects associated with shallow focal length and dispersive optics. These issues can be circumvented by using non-optical lithography techniques. Electrons have shorter wavelengths (0.1 Å) and high energy densities than visible light spectrum [144]. This makes them a possible candidate to write patterns with nanometer feature-size.

4.3.1 Electron beam lithography

The electron beam lithography is a direct writing technique that uses a beam of accelerated electrons to pattern features down to few nanometers. This is done by accurately directing a focused beam of electrons to positions over a sample, which is coated with positive- or negative-tone resist. The focused electron beam changes the solubility of the resist enabling the selective removal of resist by immersing it in a developer, and thus forming a pattern. The e-beam machine at the DTU Nanolab facility is a JEOL JBX-9500FSZ, which was installed in the year 2012. The system was designed for use in writing patterns as small as 12 nm feature size. The electron beam is accelerated with a 100 keV ZrO/W emitter and can reach a maximum scanning speed of 100 MHz.

The main advantage of e-beam lithography over standard UV photolithography is that it is very flexible and can pattern features down to 10 nm and also does not require expensive masks. E-beam lithography is a maskless technique which has a higher resolution and lower throughput. Hence, its use is limited to fabricating devices in lower volumes. Creating dense patterns over a large area can have a serious effect on the throughput, which raises serious concerns for using e-beam lithography. The drawback is slow exposure speed that results from the serial nature of the writing process, where the pattern is exposed point by point, and a relatively

of telecom wavelength. Deep UV has even shorter wavelengths, but optics and hardware becomes more expensive.

small area that can be exposed in one step. Additionally, there are many statistical errors and systematic errors that can affect the resolution and quality of exposure. These are briefly discussed below.

4.3.1.1 Stitching errors

The e-beam lithography usually has a limited area of exposure, called the writing field. For larger designs, the size of a pattern exceeds the size of the writing field. To overcome this issue, large designs are split and patterned into multiple writing fields, which are exposed side by side. To accommodate the design rule of trapezoids and polygons, the pattern is further broken down into smaller rectangles by a process called fracturing. Each field is exposed at the precise chip location with the help of stage movement and stage alignment markers. Stitching error is the small deviation at the interface of two such consecutive writing fields. This is a random error since it originates from the uncertainties in positioning and beam alignment, but usually can be rectified by taking corrective measures [145, 146].
The simplest strategy is to use the floating field feature in the file preparation software (Beamer). This feature uses an intelligent algorithm to optimize the stage movement and sorts the writing fields such that stitching errors can be reduced. These stitching errors causes large effects on the scale of a photonic-crystal, which can further lead to significant loss during propagation of light.

4.3.1.2 Proximity effects

One of the most important factors limiting resolution in many e-beam lithography systems is the proximity effect. It is the phenomenon where electron beam scatters due to interaction with the photosensitive resist and the substrate material. Hence, it is important to understand the electron-material interaction at the atomic level. There are two important aspects: the forward and backward scattering events. When the beam of electrons impinges on the resist, it experiences small angle forward scattering, which spread the beam spot size. As can be seen from simulations (see Fig. 4.2), forward scattering is very dependent upon the energy of the electron. As the electrons travels through the resist, it transfers part of its energy to the atoms, breaking the molecular chain in the resist. Eventually, these electrons enter into the substrate, where some of them undergo wide-angle scattering events. This leads to backscattering where the electrons return back to the resist at a distance far away from the incident beam, thereby breaking additional molecular chains in the resist. In other words, the electron scattering can influence or lead to undesired exposure of other features tens of microns away, leading to changes in the dissolution rate of the resist. It is these backscattered electrons which causes proximity effects.

Another important piece of this puzzle is the electron mean-free-path which is the average distance between scattering events. This is a random quantity but has a mean value depending on the energy of the electron and the atomic weight of the materials involved. This electron scattering process is mainly influenced by the energy of the electron and the material properties of the resist and substrate. For lower electron energy, the probability of scattering events goes down, i.e, the electrons start to move around without much scattering and for higher electron energy, they tend to travel fairly large distances between scattering events [148].

Combining all these complex mechanisms of scattering, the Monte Carlo model can be developed to calculate the resulting energy distribution in different layers (see Fig. 4.2). It accurately shows the diffusion process of electrons in the resist and the silicon substrate, for beam energies of 30 keV and 100 keV. The forward and the backward scattering can be described by the sum of two Gaussian-shaped

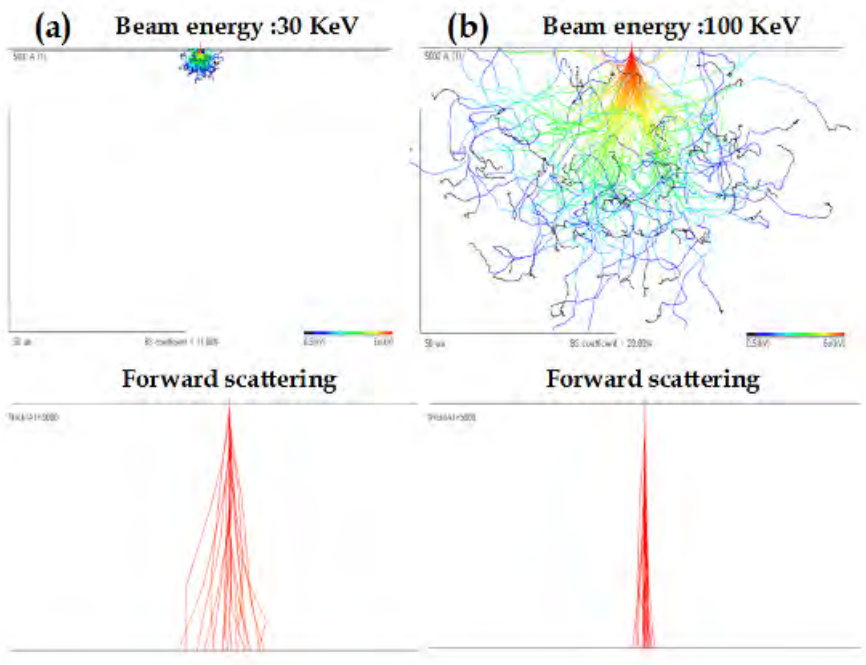

Figure 4.2: Monte Carlo simulations for a forward scattering event. Simulated trajectories of forward electron-scattering events for beam acceleration voltage of (a) 30 keV and (b) 100 keV. Image taken from [147].

distributions as is described in the subsequent paragraphs.

Proximity effect correction and calibration

Proximity effects must be corrected to get good line-width control. Pattern size can also be adjusted to compensate for this effect. However, this strategy stops working at the edges and corners of dense patterns. There are other considerations that have to be taken into account such that the dose of features to be cleared can be adjusted accordingly [149]. One common practice is to fine-tune the electron energy and assign dose, in such a way that the absorbed energy at threshold, lands at the edge of the intended design. A double Gaussian fit can precisely calculate the spatial distribution of absorbed energy intensity in the resist. The important parameters that have to be experimentally calculated are the optimum exposure dose and the Gaussian fit parameters.

Dose test

The various parameters of the e-beam resist are usually provided in the product

information brochure provided by the company. However, these are to be considered only as guideline values, since they are generated from product-specific standard tests. A preliminary test exposure, also called dose tests are hence necessary to determine the optimum exposure dose for the SOI wafers used in this experiments. This requires the exposure of a large area without structures and developed over a predetermined time. In this test, an array of square patterns measuring 100 µm × 100 µm are repeated on the SOI test substrate. Each square is exposed with dose energy ranging from 70 - 270 $\mu C\,cm^{-2}$ creating a matrix of different exposure conditions. Once the pattern is developed, the correct base dose can be obtained through inspection of the resist opening under a microscope. The base dose is the amount of energy just enough to clear the resist in a given area. From Fig. 4.3, we can see that for a base dose of 220 $\mu C\,cm^{-2}$ all the resist has been removed revealing the substrate layer for further processing.

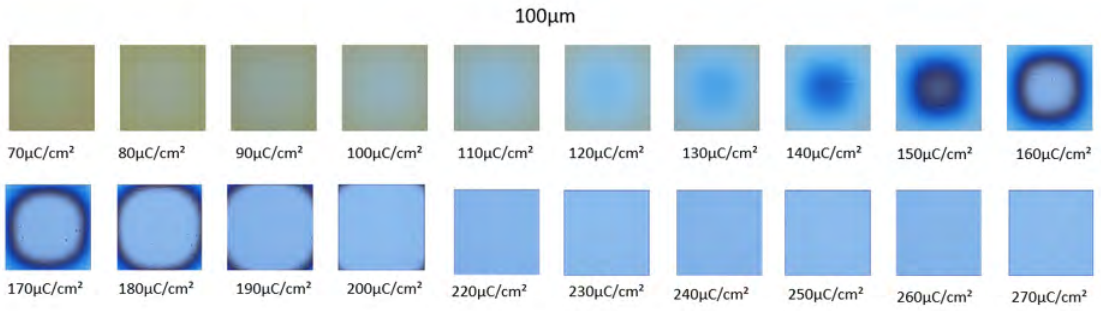

Figure 4.3: Experiment to determine the base dose. Microscopic image of an array of square areas that have been exposed with different dose energies and further developed.

Point spread function

The electron scattering behavior and the additional process parameters are specified using a point spread function (PSF). This distribution is described using a mathematical fit, often a sum or combination of two Gaussian functions. The PSF specifies the relative energy deposited at a distance r from a point exposure, and is mathematically summarized by the equation[4] [151]:

[4] A third exponential term Nu(ν) is sometimes used to represent mid-range scattering events in more complex stacks. [150]

$$\text{PSF(r)} = \text{Short range (r)} + \text{Long range (r)} \tag{4.1}$$

$$\text{PSF(r)} = \frac{1}{\pi(1+\eta)}\left[\frac{1}{\alpha^2}e^{-r^2/\alpha^2} + \frac{\eta}{\beta^2}e^{-r^2/\beta^2}\right] \tag{4.2}$$

The main parameters contributing towards the PSF are:

- Alpha(α) specifies the forward scattering (short) range of electrons.
- Beta(β) specifies the backwards scattering (long) range of electrons.
- Eta(η) is the ratio between the energy in beta-Gaussian to that of alpha-Gaussian.

The point spread function is strongly dependent on the acceleration voltage of the e-beam machine and the stack of materials and their thickness. To compensate for the proximity effects, only two terms in the above equation, α and β are adequate to describe the electron scattering events (in an SOI stack).

For a 100 keV e-beam gun, the long-range backscatter parameter is the main contributing parameter in the PSF. Hence, it can be approximated with a single Gaussian (of width β) and can be characterized independently. There are several ways to determine the correct parameters for the PSF. A search on the available literature could provide a good starting value. Monte Carlo simulations can be considered, which uses computational models to give a good estimate provided the stack of materials have been well defined. Generally, the scattering of electrons which causes the proximity effects can be modeled by using dose-convolution methods [150–152], Doughnut Method [153], Dose-modification by self consistent method [154, 155], transform-based PEC method [156], and others [157].

The dose-convolution technique has been used to extract the long-range β-parameter and gives a good approximation. The point spread function described in Eqn. 4.1 is a normalized distribution and hence the total energy should be equal to one. The PSF can then be convoluted with the pattern in order to generate a characteristic dose profile in the resist (see Fig. 4.4). This is done experimentally by depositing a uniform dose on a square pattern. Using the dose convolution technique [5], the energy

[5] dose (e-beam energy) convoluted with a proximity function

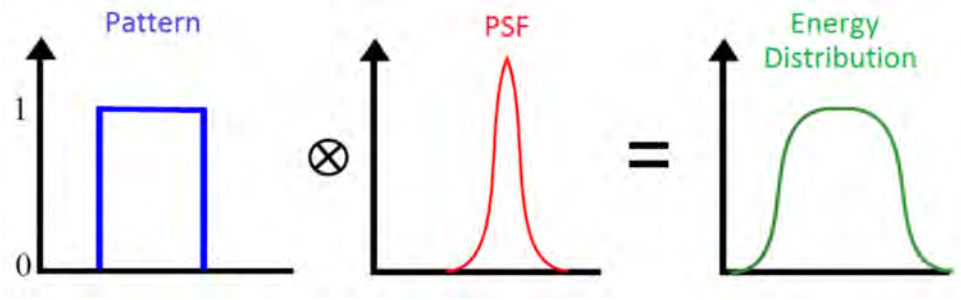

Figure 4.4: Convolution of point spread function. An illustration of the convolution of a pattern and a PSF model to generate an energy distribution [158].

distribution on this square pattern is generated with appropriate fitting parameters. This results in a non-uniform energy distribution. Contour plots of energy simulation is overlapped with optical images (see Fig. 4.5) and tried to fit with the β parameter. This can be simulated with different squares and verified if the ring is followed by the fit.

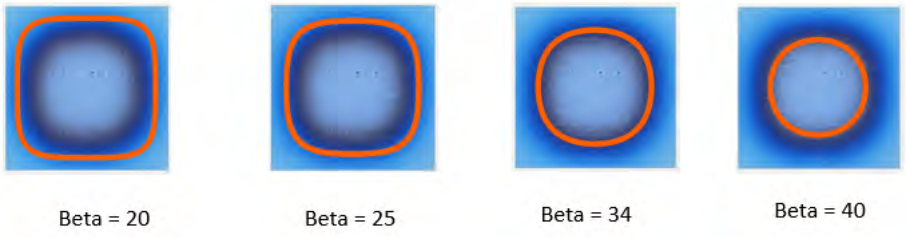

Figure 4.5: Simulated contour plots. Contour plots of energy simulation overlapped with optical images taken from microscope. A parametric value of $\beta = 34$ shows a good fit with the resist developed-area in the optical image.

Using these PEC parameters, proper dose modulation was done by BEAMER PEC module [159] as illustrated in Fig. 4.6. It ensures that the absorbed energy at the feature edges is uniform through out the mask. This leads to the uniform development over all the edges at the same time, resulting in uniform removal of resist from intended areas.

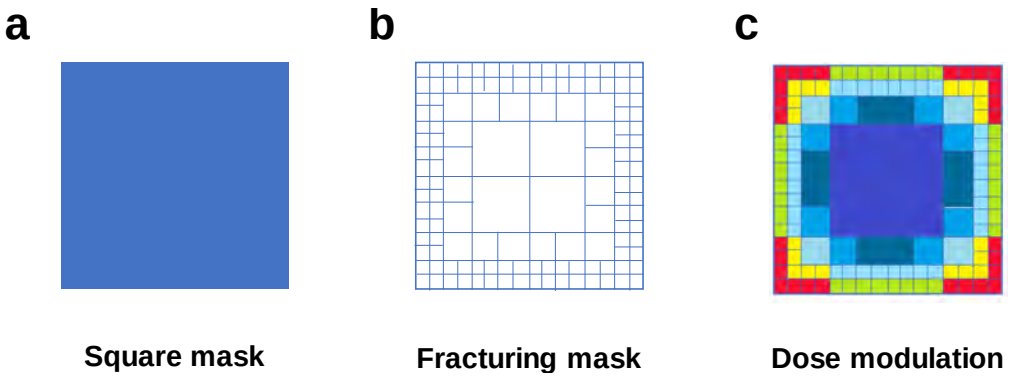

Figure 4.6: Relative dose modulation. Illustration of a square mask (a), being fractured (b) followed by dose-energy modulation (c).

4.3.1.3 Charging effects

The charge-up phenomenon in electron-beam related systems is well known and has been studied in great detail for applications of scanning electron microscopy. When the conductivity of the substrate is erratic, high electron-beam currents can usually lead to heating of the substrate and induce charging effects. This is a highly undesirable artifact. As discussed in the previous section, during exposure, electrons are accelerated towards the resist and substrate at high speeds. However small islands of accumulated charge on the substrate cause these incoming electrons to deflect in random directions, resulting in the pattern distortion (Fig. 4.7) and pattern placement errors.

There are many anti-charging schemes to overcome this problem. It has been shown experimentally that charging effects can be mitigated by carefully rearranging the sequence of exposure and also by using a highly conductive substrate (like doped silicon wafer) [160]. Thin membrane of electron traps which can capture small amounts of backscattered electrons have also been found effective, leading to significantly lowered proximity effects [161]. However, a more direct approach is to coat the resist with a metal layer or a conductive polymer thin film which can dissipate the unwanted build-up of charge [162].

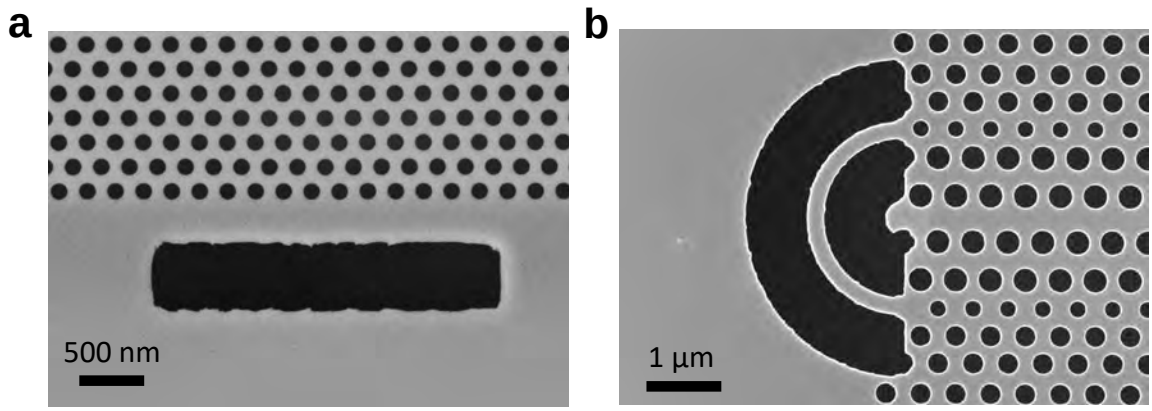

Figure 4.7: Issues caused due to charging effects. A scanning electron micrograph of a rectangular geometry (a) and semi-circle geometry (b) with rough side walls caused do to charging effects.

4.4 Etching process

Etching is one of the most important steps in semiconductor fabrication. An etch process removes selective materials from the wafer's surface, below the wafer's surface or within the substrate material to create a specific design. A combination of multiple etch processes allows for the construction of complex designs on the same chip. To create photonic-crystal free-standing membrane structures, the developed sample is treated with two different etch processes. The first etch step involves surface etch, which removes exposed regions of the silicon layer to create a structural pattern in the slab. The second step involves bulk etch process, which removes the material from underneath the silicon layer to create a membrane structure. The two etch processes have been described in detail below.

4.4.1 Inductively-coupled-plasma dry etching

Inductively-coupled-plasma (ICP) dry etching is a highly anisotropic etch technology that is widely used to create high aspect-ratio trenches and vertical side walls in substrates. A combination of chemically reactive ions and accelerated ion-bombardment processes makes it possible, either mechanically or chemically, to remove atoms from

the exposed areas. Further, the tool also provides the flexibility to vary coil and electrodes power to control the ion flux and momentum, enabling high process flexibility.

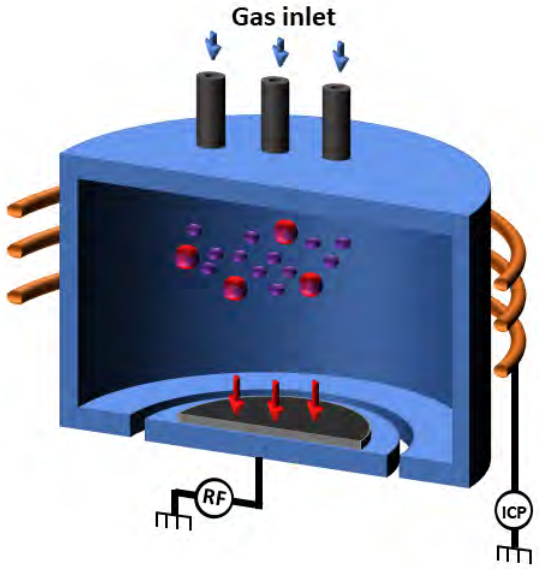

Figure 4.8: Inductively-coupled plasma source. Cross-section of an inductively-coupled plasma source illustrating the stream of reactive ion species accelerated towards the electrically-isolated substrate.

The inductively coupled plasma source is illustrated in Fig. 4.8. To create and sustain a plasma, some form of energy is required. A time-varying RF antenna inductively delivers power to the ions in the plasma discharge chamber, which then starts a collision sequence with the gas molecules. This generates a high-density of reactive ion species which are ready to take part in the etching process. These ions do not have any preferred directions. The RF power source is therefore connected to the platen electrode generating a DC bias. This imparts momentum to the ions which are then accelerated towards the substrate. The low pressure inside the plasma chamber ensures that ions undergo less scattering events and have a sufficiently longer mean free path. This results in a highly anisotropic etching process giving vertical etch profiles.

A typical dry etch chemistry can be broadly classified as unpassivated and passivated. As the name suggests, unpassivated etch chemistries do not involve the depo-

sition of any passivation layer and usually contain etchant gas constituents. They do not provide any means to prevent the sidewall erosion from stray ions. Passivated etch chemistries, on the other hand, have the provision to prevent the sidewalls from spontaneous lateral etching. Typically flourocarbons are preferred due to their non-reactive characteristics. The thickness of the passivation layer strongly depends on the concentration of oxygen in the gas chamber and the temperature at which the platen is maintained.

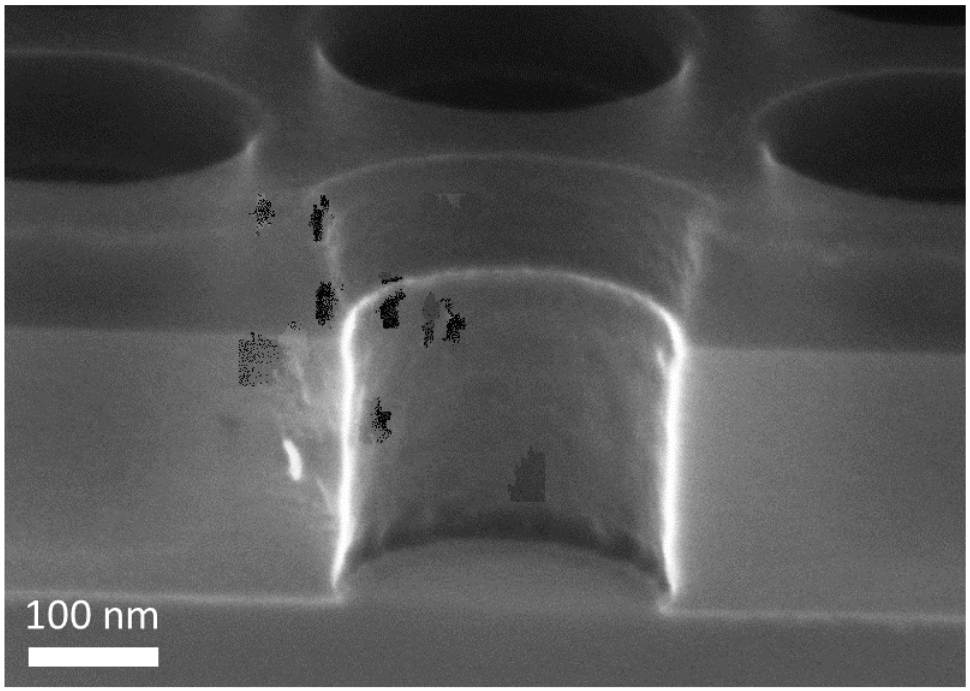

Figure 4.9: Resist selectivity. A scanning electron image showing the cross-section of an etched air-hole in silicon substrate. The side walls are vertical but with visible scallops. The etching process also shows a good selectivity towards silicon compared to the resist CSAR-62. Also, the notch at the bottom of the air-hole is formed due to insulator charge build-up [163].

Advanced silicon etching (ASE®) is a deep reactive-ion etching technique which can achieve high aspect-ratio plasma etching process in silicon using the STS-developed switched process. This technology uses fluorine-based chemistry for etching and is

based on Bosch process, which uses the concept of alternate etch and passivation steps [164].

As mentioned earlier, SF_6 is the main etchant gas and C_4F_8 is the passivant gas. At the beginning, SF_6 is injected into the plasma chamber, where gases bombard with each other giving rise to fluorine ions. These ions are accelerated towards the silicon substrate, where the exposed areas are etched producing volatile etch product SiF_4. Next, C_4F_8 gas is injected into the chamber, which is then ionized creating a fluorocarbon chain of polymer F_2. This polymer is deposited as a thin film of passivation layer all over the silicon substrate. Typically, lower temperature improves the passivation of fluorocarbons on the substrate surface.

In the subsequent step, the polymer protects the surface of the silicon from chemical etching. However, since the ions are accelerated with high energy in the vertical direction, this results in a much higher rate of removal of the passivation layer from horizontal surfaces than from vertical faces. After the removal of the polymer, the horizontal silicon surface is exposed to the etchants. The silicon at the base of the trench (holes) and the exposed resist is etched in this period, while the vertical sidewalls remain protected by the passivation layer coating. Similar to the Bosch process, the scallop features are visibly present because of the switched process. On the other hand, the vertical sidewalls and slower etch rates make this etching process ideal for nanostructures.

After silicon has been etched, the remaining resist covering the rest of the substrate has to be stripped. This can be seen in Fig. 4.9. The same etching tool is used to further strip the remaining resist layer. Oxygen plasma is generated in the chamber which reacts with the resist molecules reducing them to ash. This is further flushed out of the chamber with a vacuum pump.

4.4.2 Buried oxide wet etching

After the dry etching process, the photonic-crystal slab is still resting on top of the oxide layer. Removing this oxide layer creates vertically symmetric photonic-crystal structures where no TE-TM polarization mixing occurs [22], and moreover, it results in an increased vertical index contrast.

$$SiO_2 + 6\,HF \longrightarrow H_2SiF_6 + H_2O \tag{4.3}$$

A wet etch process selectively removes the material through a chemical reaction between a liquid etchant and the layer to be etched. In many wet etch process, the etch is isotropic and can result in undercutting. The concentration of the etchants and the temperature can directly affect the etch rates.

The processed sample is immersed in a bath of etchant and slowly agitated to achieve good process control. A buffered hydrofluoric acid (BHF) with a wetting agent is used to to selectively remove the silica cladding. It is a mixture of 12% HF with the buffering agent,NH_4F and a wetting agent, H_2O. Silica or SiO_2 readily dissolves in HF producing hexafluorosilicic acid (H_2SiF_6), which is soluble in water. A cross-section of the underetched oxide later can be seen in Fig. 4.10. The BHF has a more stable etch rate of about $110\,nm\,min^{-1}$ at room temperature. The structures are usually overetched, forming cavity under the perforated silicon slab.

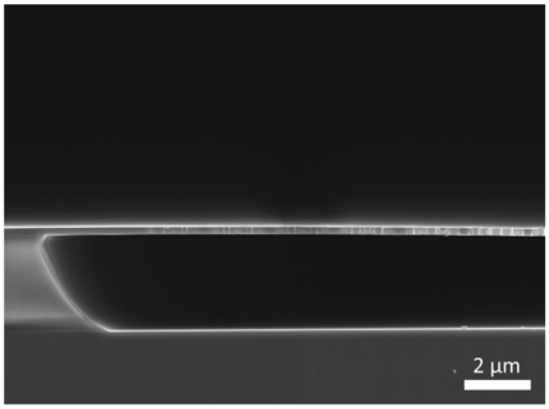

Figure 4.10: Underetched oxide layer. Cross-section scanning electron micrograph of a photonic-crystal membrane illustrating the underetched oxide layer.

4.5 Sample drying

This is the final step in the processing of photonic-crystal membrane structures. The membrane design of the photonic-crystals can increase the risk of collapse or breakage due to the surface tension of the liquid (water). The samples are thus immediately dried in ethanol fume dryer after the water-rinsing process. The samples are placed in a chamber filled with the fumes of Ethanol, which is heated to about 70 °C. This will cause the water to evaporate from the surface keeping the membrane safe from collapse.

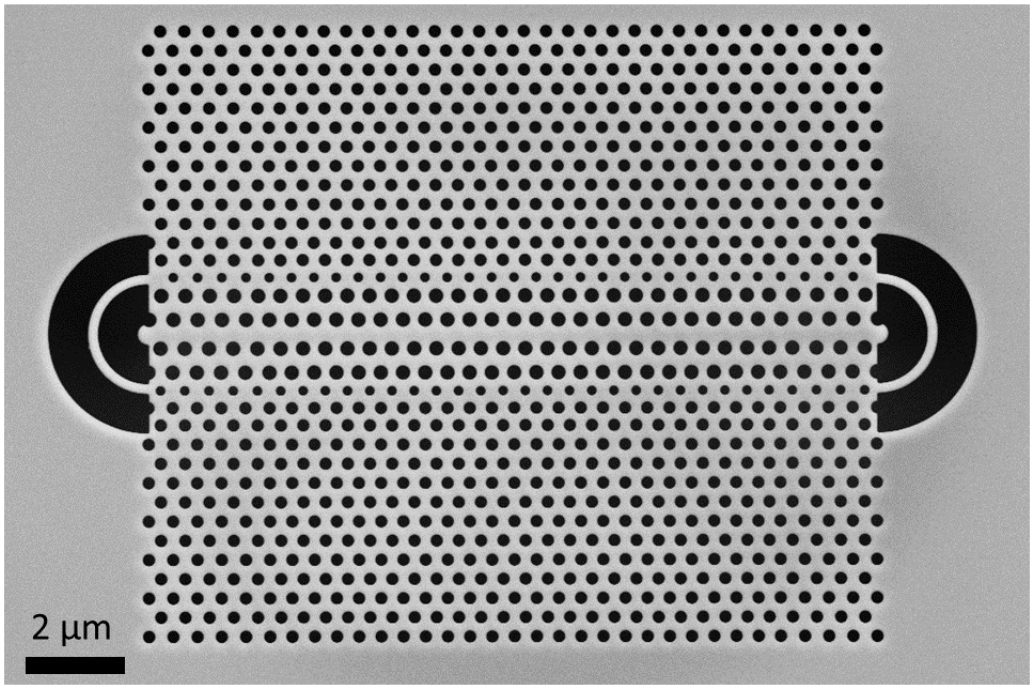

Figure 4.11: Glide-symmetry waveguide resonator design. A scanning electron micrograph of a 20 µm long glide-symmetry waveguide resonator with circular gratings.

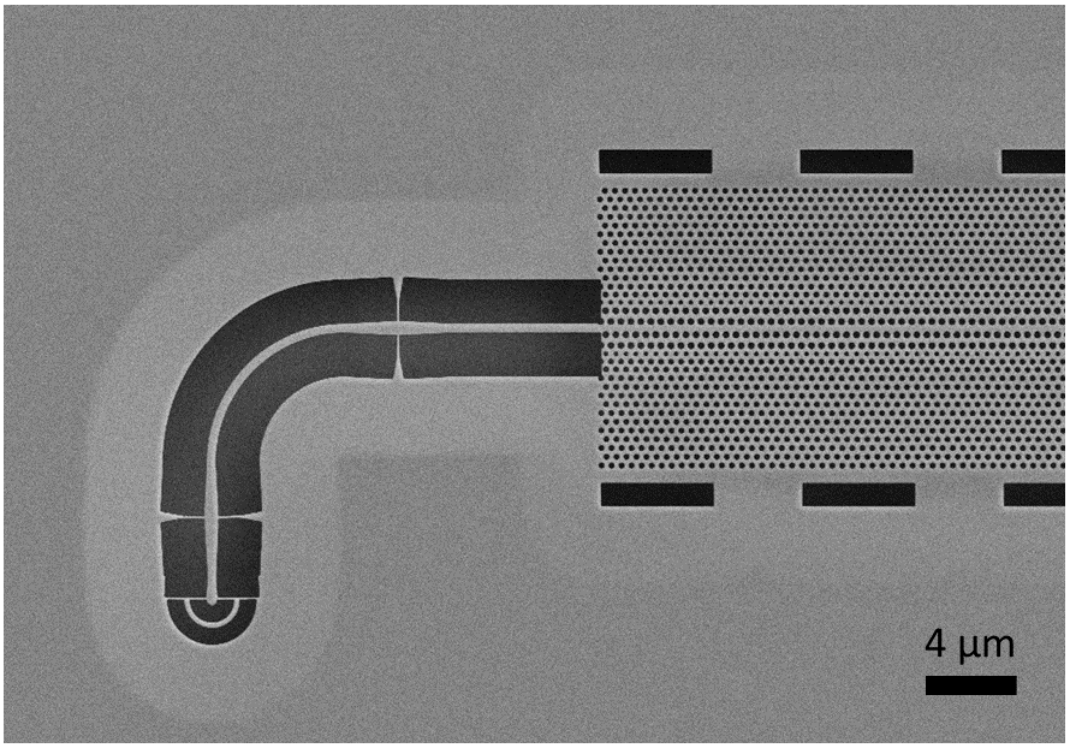

Figure 4.12: Glide-symmetry waveguide and access waveguides. A scanning electron micrograph of a glide-symmetry waveguide interfaced with suspended access waveguides supported by tethers. The access waveguide makes a 90° turn before it is terminated by circular gratings. Rectangular openings around the photonic-crystal releases excess stress and also functions as an opening for the etchants to reach the oxide layer.

5

Experimental characterization

Coupling light into photonic devices which are of the order of submicron length scales can be complicated. Here the setup was designed[1] for probing guided modes of a planar photonic crystal resonator using transmission measurements. These modes are excited from one end of the cavity and collected from the other end at the same time. The fine balance between the transmissivity and reflectivity of the resonator boundary ensures that some modes leak out. The setup consists of free space optics and is based on top-excitation method. The setup can also be used in a wide variety of transmission measurements though. This chapter describes the design of the setup, and the considerations behind it.

5.1 Overview

The setup is based on the free-space coupling of light into the photonic crystal waveguides. A supercontinuum light source from NKT (NKT SuperK EXR-15) is used for probing the waveguides. The emission spectrum ranges from 400 nm - 2400 nm, which allows for characterization over a much broader range than a tunable laser, which usually has a range of 150 nm. The SuperK is a high-powered pulsed laser where the maximum output power is around 5 W. Since only a small part of the spectrum is necessary for characterizing silicon waveguides, the output is connected to a dichroic mirror which splits the spectrum at 1180 nm. The lower wavelengths are then safely redirected towards a beam dump while the longer wavelengths are coupled to a polarization-maintaining fiber.

[1] This setup was designed and built by Morten Herskind as part of his M.Sc. project work [165].

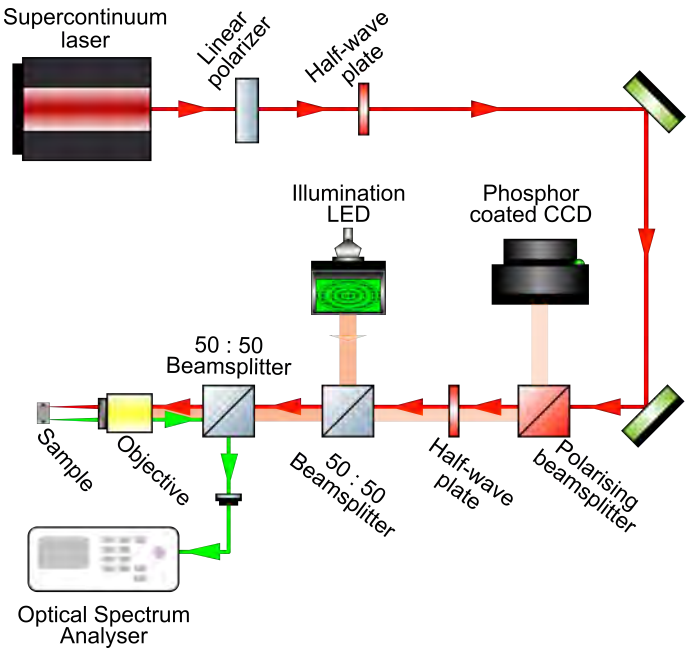

Figure 5.1: Schematic of the experimental setup. The resonators are excited by a supercontinuum light source, which is directed on the device by polarized confocal microscopy. This is indicated by the path of red line. The transmitted signal is collected from the other end of the resonator through the same objective, and then redirected into the optical spectrum analyzer via the outcoupling path which is indicated by the green line.

Light is launched into the free-space optics setup through a fiber coupler. The light from SuperK has random and elliptical polarization. After careful collimation, this beam of laser passes through a linear polarizer to change it into a linearly polarized light. Now, the polarization of the laser beam must be matched with that of the output of the polarization beamsplitter. This is done with a half-waveplate which can be optimized for maximum transmission. In other words, the half-waveplate along with the linear polarizer functions as a power controller. After optimizing the input beam for maximum power, the polarization must be further rotated by 90° to couple into the TE modes of the resonator device. The second half-wave plate performs this operation and gives us control over the modes that we want to excite. This enables experimenting with both TE- and TM- mode excitation.
Further, the light runs into two 50 : 50 beamsplitter. The first beamsplitter is required to direct LED light towards the sample for illumination which is further redi-

rected towards the imaging system. The second beamsplitter redirects the probed transmission signal into the outcoupling path (Fig. 5.1, green). Since the optical devices are few microns in area, this beam is further narrowed down using an objective. This objective is mounted on a linear translation stage which allows us to focus the laser beam on the surface of the sample. A series of four mirrors are placed along the path of the collimated beam. These mirrors can be optimized to ensure that the laser beam remains in the same horizontal plane throughout the setup. It is highly desirable to have a good imaging camera with high quantum efficiency and low noise for visualizing the alignment of the excitation spot. The image quality of the live feed is rather low. This is because all the optical elements in the setup are chosen for high transmission in the 1200 nm - 1700 nm range. There is not enough visible light transmitted to allow the use of a regular camera, so instead, a regular charge-coupled device (CCD) camera with a phosphorous coating is employed. The sample is illuminated with a infra-red LED, and the infra-red image is then incident on the coating which upconverts the light to visible wavelengths which can be detected by the CCD. The resolution of the CCD is low, and the coating also distorts the image slightly which is the reason for the low image quality (See Fig. 5.2).
The sample is fastened onto a chip-carrier which is directly mounted on a translation stage which can travel in x- and y-directions. The sample is directly placed orthogonal to the path of the laser beam. The range of the translating stages allows us to scan over the entire chip, which is around 2x2 mm in area. Since we are trying to probe the guided mode resonances, both excitation and collection occurs at the same time. The same objective is used to excite the transverse-electric modes at the input gratings and collect the guided resonance at the output gratings. The collected optical signal is further redirected towards the output path through a 50 : 50 beamsplitter. Two mirrors ensure that the optical signal is directed efficiently into the optical spectrum analyzer via a fiber-outcoupler.

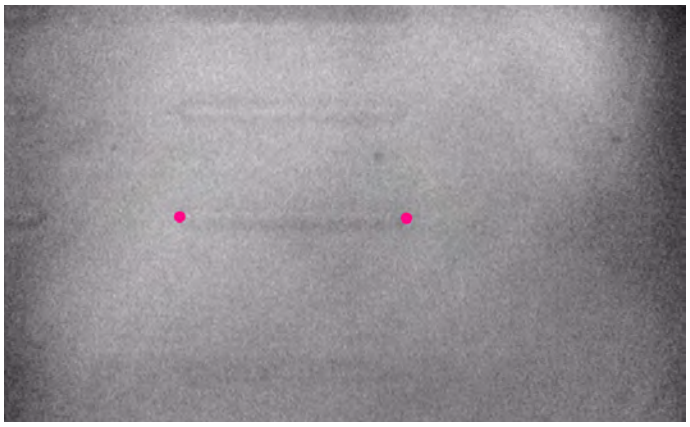

Figure 5.2: Screenshot of the sample with reference markings. A screenshot of the live-image feed from the CCD camera showing different waveguides. The gratings are marked with a drawing tool on the computer screen, and further the laser spot is aligned with the markings to excite the waveguide modes. Appropriate labels have been made on the sample to identify all the devices.

5.2 Probe techniques

The transmission measurement approach relies on exciting and capturing reflection from an optical Fabry–Perot cavity. The excitation light is directed onto one of the grating couplers on each device using a polarizing confocal setup to ensure that only transverse-electric modes are excited. This can be achieved by fine-tuning the two alignment mirrors in the input path and making sure that laser impinges on the sample at an oblique angle. On the same lines, the two alignment mirrors in the output path can be tuned to ensure that light transmitted through the cavity is extracted from the second grating coupler. The position of the beams can be seen in the live image feed. For measuring the resonances in a W1 waveguide, this method of fine-tuning the in-out coupling path ensures optimized transmission. The objective translation stage can also be moved linearly to focus for better transmission. It requires further optimization of alignment to measure the resonances in a glide-symmetry waveguide.

The asymmetry introduced by the glide-plane in the photonic crystal changes the symmetry of the circular coupler gratings. This deformity introduced a new degree of freedom and changes the acceptance angle for the circular gratings. Along with the oblique angle, horizontal degree of freedom should also be optimized. This not only increases the coupling efficiency, but also excites the guided modes into the slow-light regime. In other words, there is a high probability to excite transverse-electric modes in both bands of the glide-symmetry waveguide if light were to be angled within this acceptance cone.

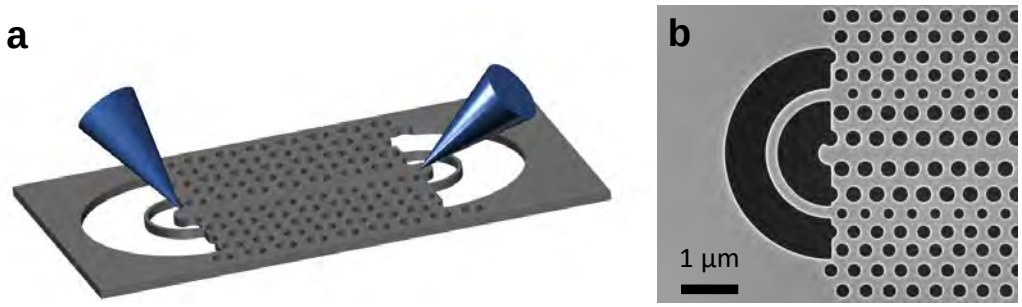

Figure 5.3: Schematic of probing technique. (a) An illustration of the angle of incidence and collection while exciting and measuring the transmission signal in a glide-symmetry waveguide resonator. (b) A scanning electron micrograph of a distorted circular grating coupler design caused by introducing glide-plane symmetry.

After both the input and the output paths are aligned, the captured signal is characterized with an optical spectrum analyzer with a spectral resolution of 0.5 nm, which scans for a span of wavelengths and measures the optical power levels. This method is highly reproducible if the same optimization scheme is maintained for all the devices. Once the signal is optimized, a slow scan on the optical spectrum analyzer gives a high-quality data with higher resolution of 0.02 nm.

6

Transmission measurements on photonic-crystal waveguides

A proper optical characterization of slow-light device structures typically requires the measurement of two quantities: optical transmission and the group index. The spectral features of these measurements provide essential information about the properties of the photonic-crystal waveguides. The following chapter is dedicated to studying and analyzing the transmission spectra of glide-symmetry waveguides. The glide-symmetry waveguides are novel and their behavior has not previously been studied, and hence it is important to benchmark their behavior against a known design.

In order to make sure that the transmission measurements of the glide-symmetry waveguides are justified, a known W1-waveguide resonator fabricated on the same chip is also probed. W1 waveguides have been studied extensively and well established [27, 29, 30, 96, 166]. This ensures that the measurements are not out of bound and also helps to identify systematic errors. The optical properties of fabricated devices can often diverge from their expected behavior in spite of having advanced simulation results and precise fabrication techniques. This mismatch can usually stem from technological challenges related to subnanometer precision or approximate computation-based simulations. Appropriate measures have been adopted to take these shifts into account. In the final section, I also explore the different regimes of transport in slow-light devices and discuss a novel method to measure the localization length.

6.1 W1 waveguide

The W1 waveguides are conceived from a photonic-crystal slab by inserting a line disorder in the form of a row of missing holes along the propagation direction. This creates waveguide modes whose eigenfunctions are strongly localized along the defect [22]. These localized defect modes are illustrated in the dispersion diagram of the W1 waveguide in Fig. 6.1a. It can also be observed that two defect states appear in the transverse electric (TE) band-gap which exists between the normalized frequency range of $a/\lambda = 0.2304$ and 0.3226. These defect modes are guided by the presence of photonic band-gap as long as they are well below the light line. Above the light line, these modes become very lossy and hence radiate in the out-of-plane direction contributing to intrinsic loss. These two modes can be classified as even (blue) and odd (red) depending on their mode symmetry.

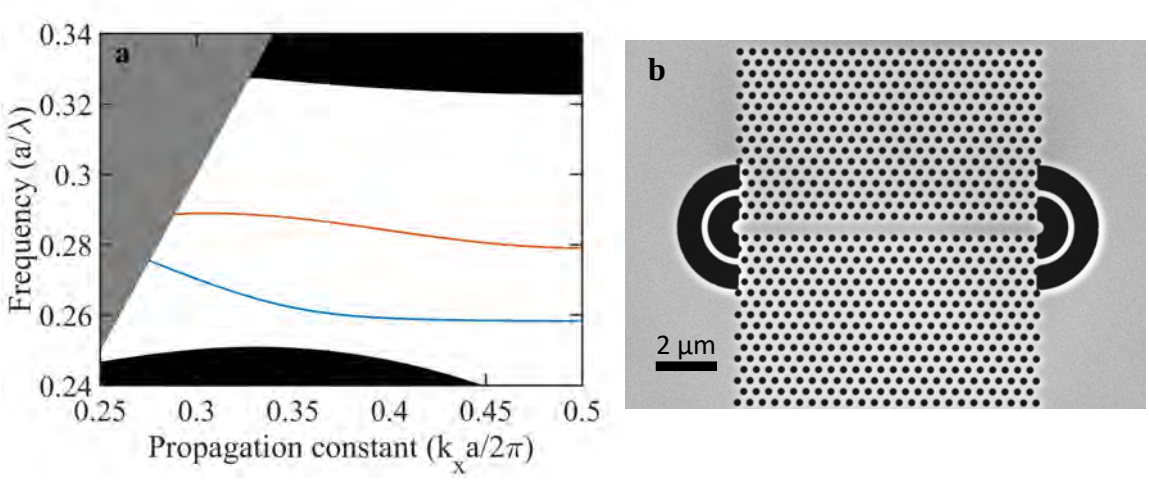

Figure 6.1: W1 photonic-crystal waveguide. (a) Dispersion diagram of a W1 photonic-crystal waveguide showing the different waveguide modes and regions. The blue and red curves illustrate the even and odd waveguide modes respectively. The blue mode is investigated in the main text. The area shaded in black and gray represents slab modes and radiation modes respectively. (b) The scanning electron micrograph of a fabricated W1-waveguide resonator (length, $L = 10\,\mu m$) illustrating the array of missing holes.

To characterize these waveguides, Fabry-Pérot resonators of different lengths were

fabricated on the same chip. Circular grating couplers were used to excite and collect modes from these resonator devices. For statistical analysis, multiple realizations of each device were fabricated and measured. A total of 60 resonator devices consisting of 12 different lengths ($L = 10\,\mu\text{m}, 20\,\mu\text{m}, ..., 120\,\mu\text{m}$) with 5 identical copies of each device were fabricated. A scanning electron micrograph of a fabricated device is shown in Fig. 6.1b. The photonic crystal slab under investigation consists of air holes with a radius $r = 120\,\text{nm}$, positioned in a hexagonal lattice with a periodic spacing of $a = 400\,\text{nm}$. This gives a well-balanced r/a ratio of 0.3. The band diagram for the waveguides was calculated using an open-source software package called MPB which can solve Maxwell's equations in periodic dielectric-structures [120]. From the dispersion curve diagram Fig. 6.1a, the cutoff wavelength for the even guided mode is seen around $a/\lambda = 0.2583$.

Figs. 6.2(a-f) shows normalized raw data for devices of different lengths along with the calculated dispersion relation. Transmission measurements were performed using a supercontinuum coherent white-light source with long-pass filtering to excite the fundamental TE-mode. The wavelength was scanned from 1400 nm to 1600 nm, centered around 1500 nm for excitation. A wide span was chosen keeping in mind the large frequency range of the TE band-gap and random shifts that arise due to variations in the hole radii during fabrication. The light transmitted through the cavity is extracted from the second grating coupler and characterized with an optical spectrum analyzer with a spectral resolution of 0.5 nm. The choice of resolution was based on the signal integrity of the transmission fringes and the influence of stray standing waves arising from the silicon substrate.

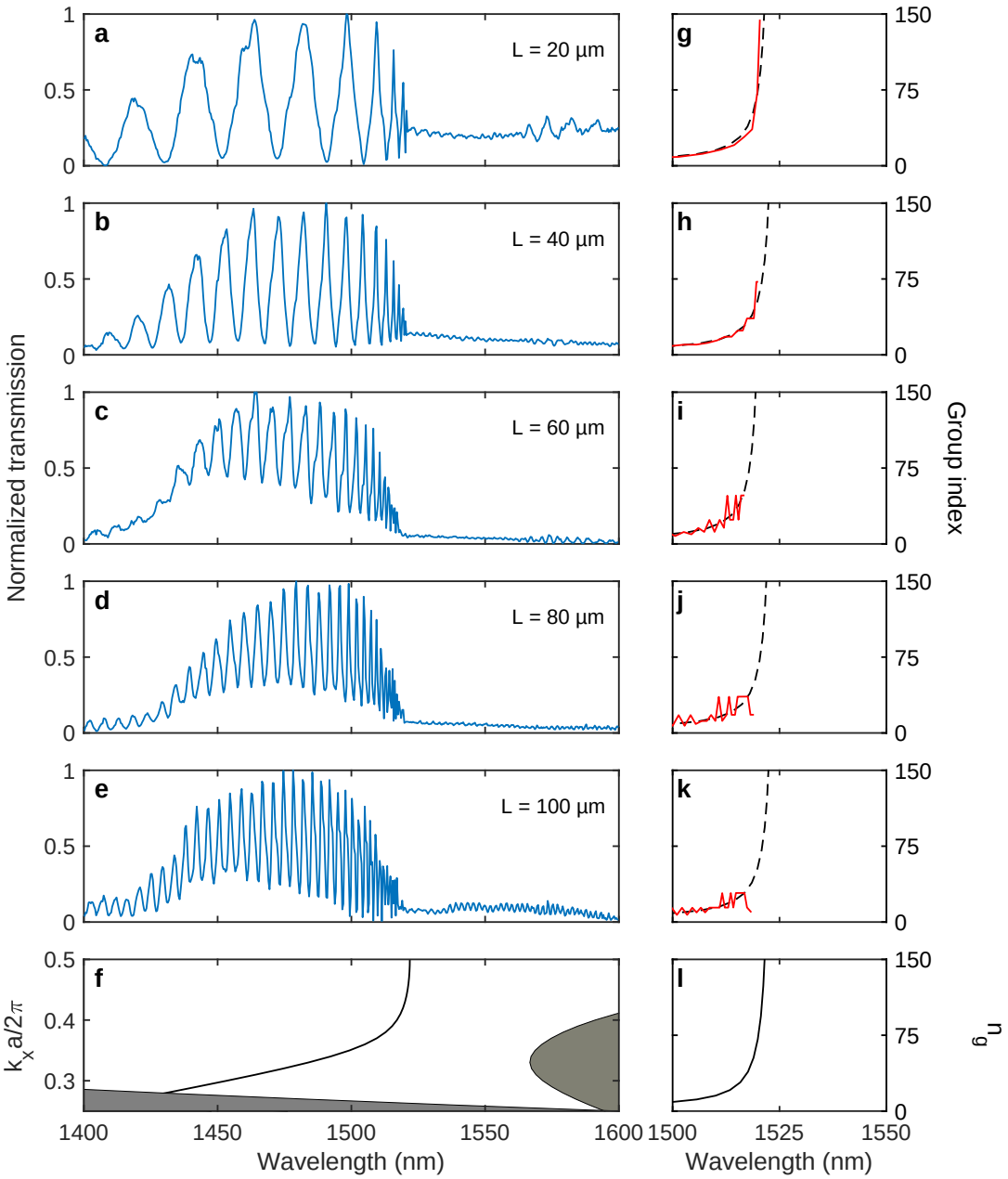

Figure 6.2: Transmission measurements on W1-waveguide resonator devices. (a-e) The experimental transmission spectra for different lengths exhibit clear Fabry-Pérot resonances and a cut-off around 1520 nm in agreement with (f) the calculated dispersion relation. (g-l) The extracted group index agrees very well with theory below the cut-off. The theory curves have been shifted by 21.2 nm to compensate for fabrication uncertainties such as hole size and slab thickness.

For all lengths, the transmission exhibits two important features: fast oscillations and drop in transmission. The fast oscillations are Fabry-Pérot resonances spread over a large range of frequency. These oscillations are induced by multiple reflections at the facets of the waveguide which results in standing waves. We can also observe that only even modes are excited by the incident light source. Low transmission regions correspond to both the band-gap region and regions where even-modes do not exist. The agreement between theory and experiment is generally excellent. The theory dispersion diagram is calculated from hole radii parameters extracted from scanning electron micrograph of a fabricated device[1]. Here the dispersion mapping has been manually shifted to lower wavelength in order to account for discrepancies in the hole radii measured from scanning electron micrograph, nanometer scale variations in hole radii during fabrication, sidewall non-verticality, and variations in slab thickness. This offset is calculated by fitting the experimentally extracted group index with the theory.

By further analyzing the fringe pattern, the frequencies where slow-light manifests can be identified. The transmission spectra of these devices abruptly drop to zero at the cutoff of the waveguide mode. It is difficult to strictly pinpoint at the actual cut-off wavelength. In the vicinity of the cutoff wavelength, a gradual decrease in the spacing between the Fabry-Pérot fringes ($\Delta\lambda$) can be seen, signifying the onset of slow-light behavior. Transmission in the slow-light regime can be suppressed due to several reasons: increased light-matter interaction, the formation of localized modes, enhanced backscattering, or inefficient coupling. The resonator setup and measurement on different lengths allow us to eliminate only a few of the above causes.

Further, the oscillations are analyzed to extract the group index from resonators of all lengths. It is important to note that two transformations have been applied in the group index extraction procedure. Firstly, the calculated dispersion relation and group index have been shifted by an offset of 21.2 nm, which compensates for systematic shifts in hole radii and slab thickness. Secondly, all experimentally extracted

[1]Procedure to measure the hole radii from scanning electron micrograph images is discussed in Appendix C.

group indices have been multiplied by 2. This factor likely originates from the grating couplers, which allows coupling into multiple spatial positions. This correction factor was found to be consistent for all devices. This factor is also immediately visible from the raw data in Figs. 6.2(a-e) as an anharmonic component in the Fabry-Pérot oscillations revealing that only every second oscillation is resolved. This was also confirmed by a sequential Fourier-transform analysis of the raw data [165], but since the waveguide is highly dispersive, the Fourier transformation cannot give reliable information about the points of interest close to the slow-light regime. Instead, an automatic peak-search algorithm was adopted where peak prominence and distance are used to extract the group indices. This was also confirmed by transmission measurements done on the same sample using an evanescent-coupling method [167]. The measurements were performed by an external collaborator, Guillermo Arregui, a doctoral student from Pedro David García Fernández's group at the Catalan Institute of Nanoscience and Nanotechnology (ICN2), Barcelona. A detailed explanation about the missing peaks and group-index extraction is given in Appendix D. All results presented in this thesis have been subjected to these two transformations.

The group index profiles are extracted and plotted for the transmission of all the lengths in Fig. 6.2(g-k). It can be observed that in all the cases the group index follows a similar trend and starts at a value around $n_g = 6.5$. For shorter devices, a sharp increase in the group index value exceeding $n_g = 100$ can be seen, until the transmission is terminated close to the band-edge of the waveguide mode. However, as the length of the resonator increases, a general trend can be observed in the behaviour of n_g. The maximum measurable group index falls gradually from $n_g = 100$ in 20 µm to $n_g = 30$ in 100 µm, as transmission drops well before the W1-cutoff wavelength. The fluctuations in the measured group indices arise from the limited signal-to-noise ratio in particular around the slow-light maximum. This indicates that the behavior is not artificial, but a consequence of localized mode formation. In addition, minor fluctuations in the group index can be attributed to dispersion in the optical feedback of the resonator[2] [168].

[2]This can be strictly distinguished from the strong peaks that arise due to localized modes by using a numerical criterion.

It is well-known that W1 waveguides exhibit a strong dispersion [27, 61] and the group index diverges. In experiment, this divergence is cut-off by the enhanced backscattering in the slow-light regime, which ultimately induces Anderson localization [95, 113, 166]. The localization length or the length over which light can propagate unhindered is a reasonable parameter to quantify this effect. There is no easy way to measure the localization length. However, we show that it can be simplified using the modified Thouless criterion for resonators [169]. This will be discussed in the final section of this chapter.

6.2 Glide-symmetry waveguides

The characterization of the glide-symmetry waveguides has been the central theme of this thesis. As explained in section 2.5, the slow-light region and the presence of a degenerate cross-over point are the main salient features of these devices that need to be investigated. The glide-symmetry waveguides and W1 waveguides were fabricated on the same chip to maintain the same process variations over the entire sample and to avoid any minor differences between different fabrication processes.

The dispersion diagram illustrating the transverse-electric modes of a glide-symmetry waveguide is shown in Fig. 6.3(a). The gray region describes the continuum of bands supported by the photonic crystal bulk, while the light gray shaded region corresponds to the light line. Similar to the W1 waveguide, it is interesting to study the waveguide modes that appear in the frequency range below the light line. The two points of main interests are (i): the degeneracy point at the Brillouin-zone edge $a/\lambda = 0.2909$ and (ii): the point of flat-band region where slow-light is observed, which appears at $a/\lambda = 0.2901$.

Similar to W1 waveguides, Fabry-Pérot resonators of different lengths were fabricated with the glide-symmetry waveguide design on the same chip. A total of 60 resonator devices consisting of 12 different lengths ($L = 10\,\mu\text{m}, 20\,\mu\text{m}, ..., 120\,\mu\text{m}$) with 5 identical copies of each device were fabricated. In order to reduce systematic errors and compensate for stage drifts, the setup was realigned every time before a device was measured. A scanning electron micrograph of a fabricated device is

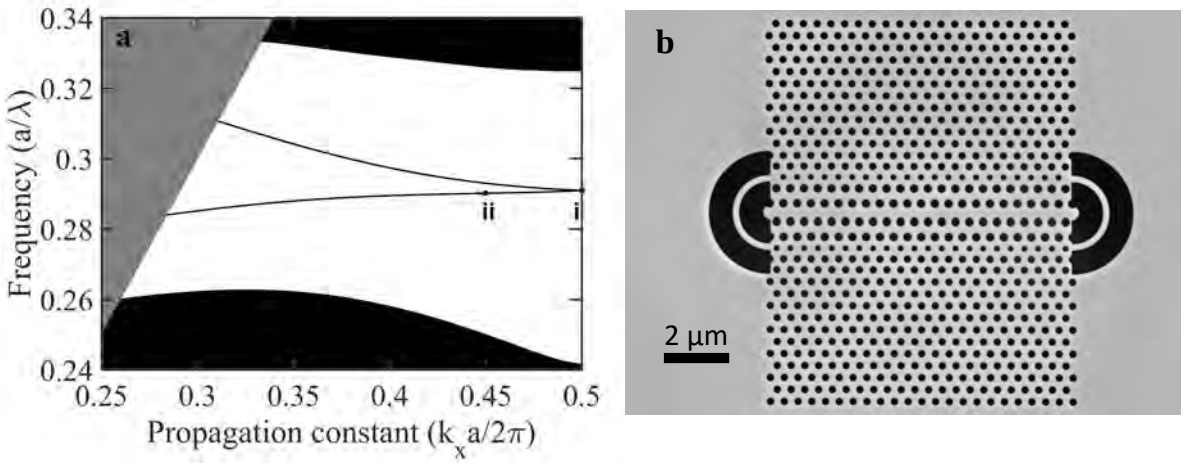

Figure 6.3: Glide-symmetry waveguide. (a) Dispersion relation of the glide-symmetric waveguides exhibiting two waveguide bands below the light line. The important points are highlighted as (i): the zone-edge degeneracy and (ii): the region of flat-band where slow light is observed. (b) Scanning electron micrograph of a 10 µm long glide-symmetric waveguide terminated by high-reflection grating couplers to form a resonator.

shown in Fig. 6.3b.

The devices were characterized using the same setup that was used for measuring the transmission in W1 waveguides. The same supercontinuum white-light source was used and the polarization setup ensures that only transverse-electric modes are excited. Coupling light to the modes present on the right side of the slow-light section has been a major challenge [165]. However, with appropriate alignment strategies (sec. 3.1.2), a full transmission over the entire bandwidth was recorded.

Fig. 6.4(a-e) and Fig. 6.5(a-e) shows normalized transmission for five nominally identical devices of two different lengths, 30 µm and 90 µm respectively. It can be observed that the transmission spectra are almost identical and highly reproducible, both in terms of transmission intensity and observation of special features. Consider the transmission measurements for a particular case of two different waveguide lengths, 30 µm and 90 µm shown in Fig. 6.4(f) and Fig. 6.5(f). For both cases, strong Fabry-Pérot oscillations are observed indicating multiple reflections at the waveguide facets. Since the glide-symmetry waveguides are not characterized by any gaps between the waveguide modes, a broadband transmission spectrum spanning over 100 nm can be seen. The dispersive properties due to the structural geometry can be observed. For 30 µm long device, on tracing the oscillations from lower to higher wavelengths, it can be seen that the Fabry-Pérot oscillations become more pronounced i.e, fringes get closer to each other signifying the onset of the slow-light regime, and eventually spreads out again at higher wavelengths. For 90 µm long device, Fabry-Pérot oscillations are observed for all the wavelengths, except for the region around the slow-light regime where the transmission drops. When light enters into the slow-light regime, the low group velocity increases the strength of interaction between light and matter leading to losses through various scattering mechanisms. Thus, propagation is halted around wavelengths 1525 nm.

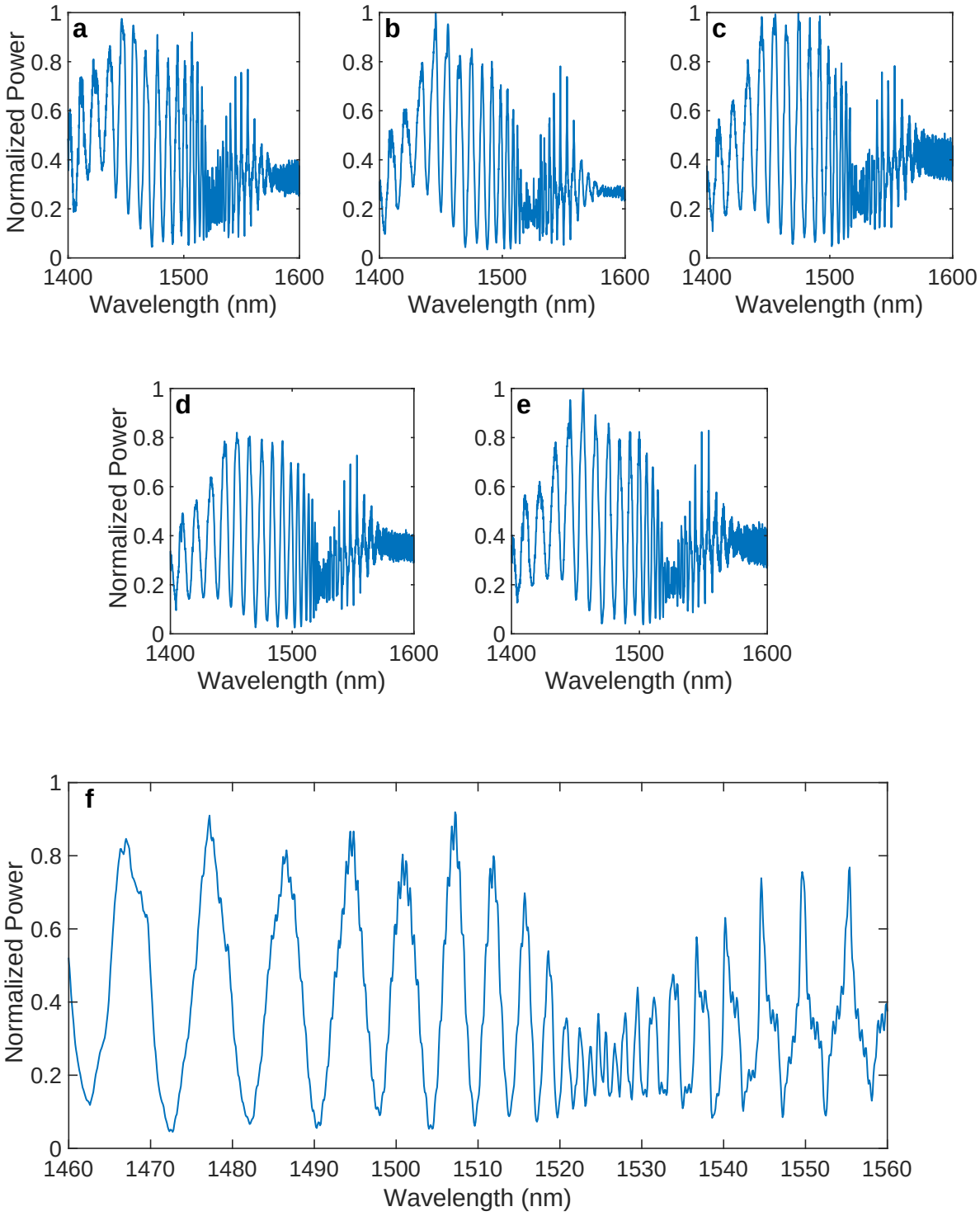

Figure 6.4: Multiple measurements on an ensemble. (a-e) Transmission measurements of five different nominally identical copies of a 30 µm long glide-symmetry waveguide fabricated on the same substrate. The transmission curve is normalized to the maximum intensity. (f) Transmission zoomed around the slow-light regime for sample (a).

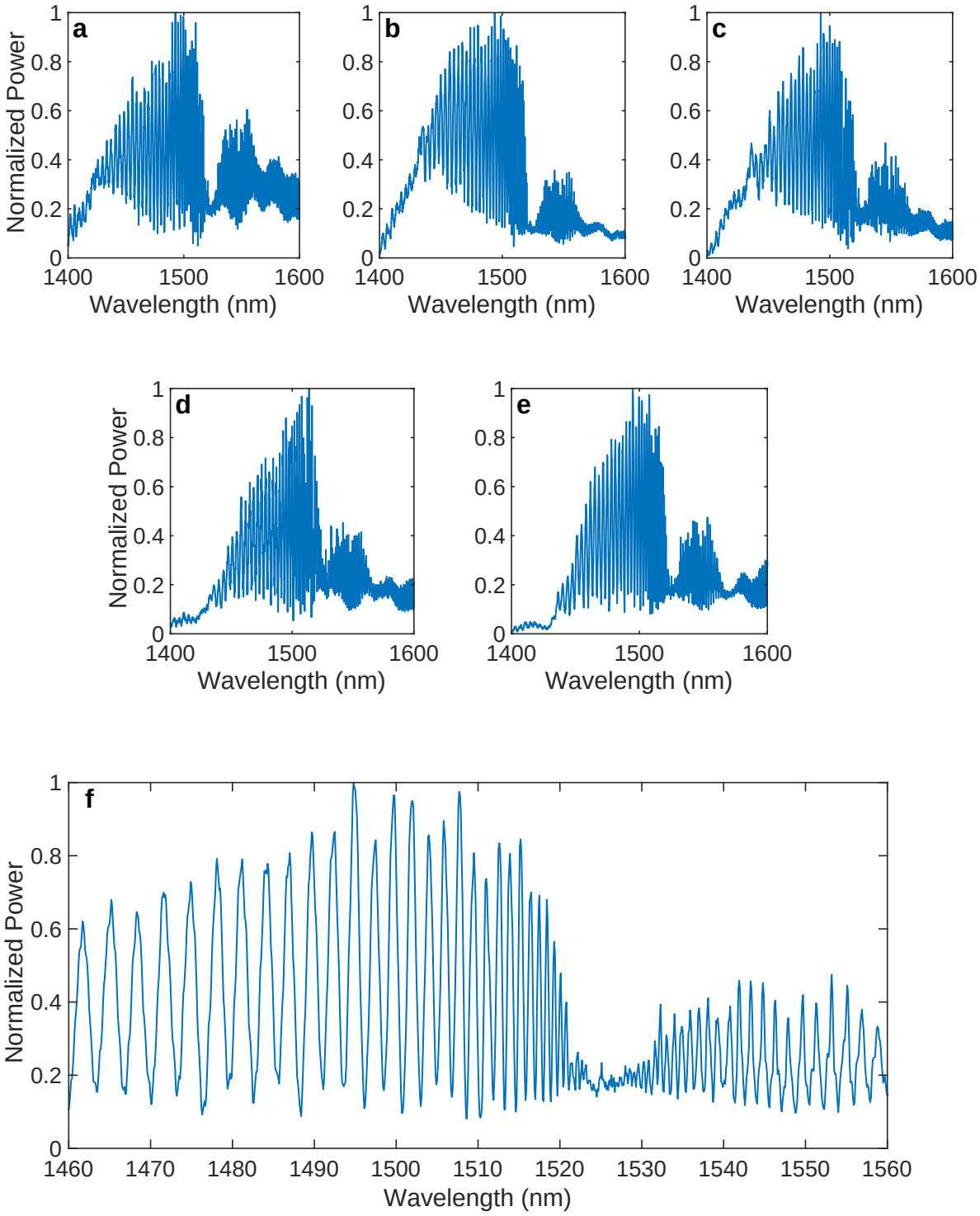

Figure 6.5: Multiple measurements on an ensemble. (a-e) Transmission measurements of five different nominally identical copies of a 90 µm long glide-symmetry waveguide. (f) Transmission zoomed around the slow-light regime for sample (e) shows that it has a limited signal-to-noise ratio owing to multiple scattering events and relatively shorter localization lengths.

Consider the transmission measurements and group index extracted for different lengths of glide-symmetry waveguides shown in Fig. 6.6. For all the lengths, it is observed that the group index starts at a value of $n_g \approx 12$, traverses through the slow light region and drops back to a value of $n_g \approx 14$. The behavior of light in the slow-light regime follows a very interesting trend. For the shorter devices, the group index peaks at $n_g = 92$ and there is a good agreement between the measured group indices and the theoretical prediction. For longer devices, the limited signal-to-noise ratio around the group-index maximum makes it difficult to discern between losses originating from transmission or Anderson localization. Since Anderson localization in photonic-crystal waveguides depends sensitively on the group index [166], the reference experiments earlier done on conventional W1 waveguides should provide hints about suppression of light-propagation in the slow-light region. This is a unique setup that exhibits a clear picture of the delocalization-localization transition since only the size of the system is changing for a fixed disorder. To further investigate the impact of high group-index on the light transport in glide-symmetric waveguides, a new approach is conceived for estimating the localization length which will be discussed in the final section of this chapter.

We now turn our focus to the transmission spectra of a particular set of glide-symmetry devices, which showed improved coupling into both the waveguided modes. Coupling light into the glide-plane waveguide resonator devices with the circular gratings has been a challenging task [165]. The proper alignment to direct the excitation light onto the grating couplers has been a major challenge. To avoid issues with the misalignment, a systematic approach was used and the alignment of the mirror were positioned in such a way that showed significant coupling into both the branches of the glide-symmetry waveguide.

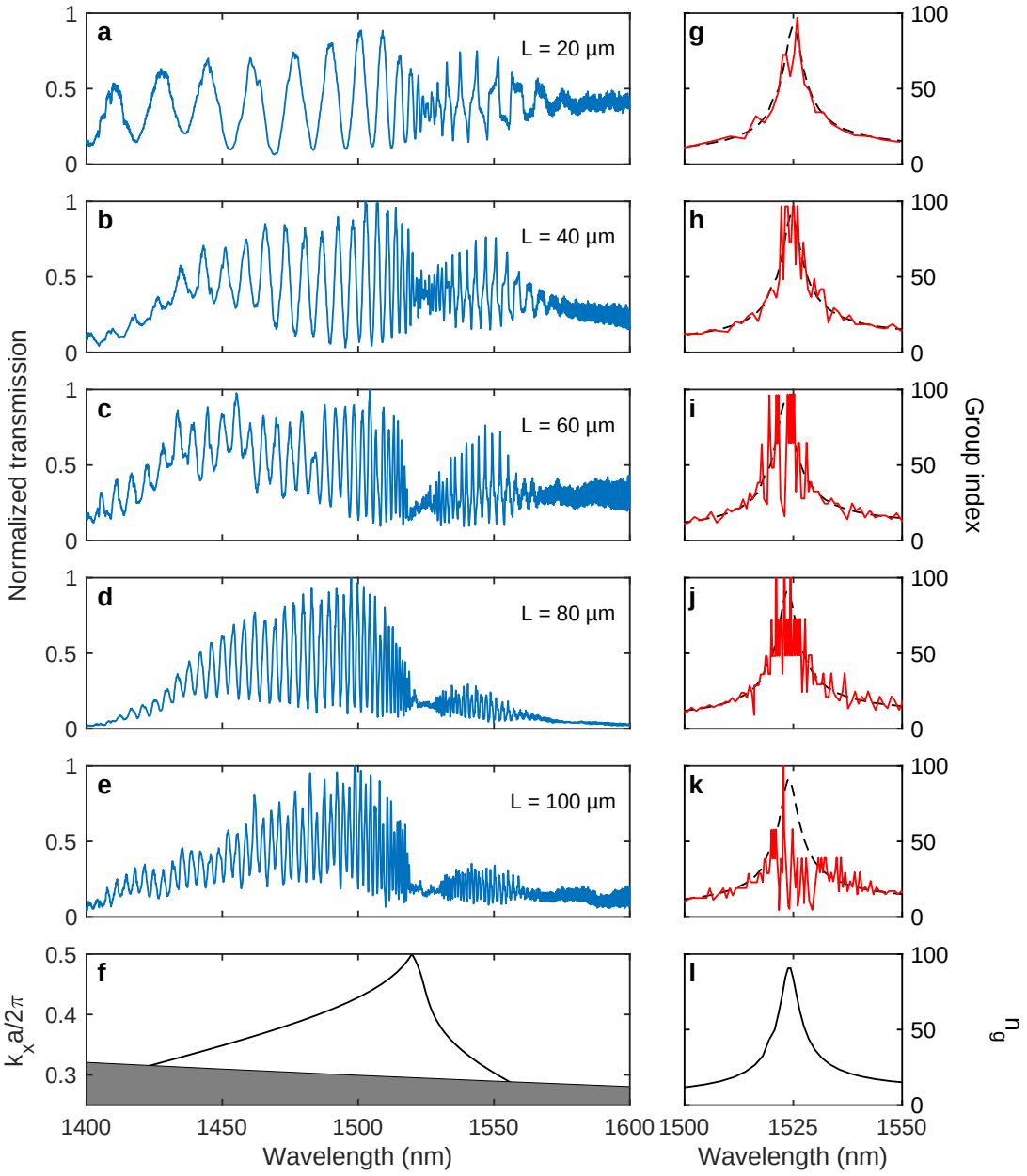

Figure 6.6: Transmission measurements on glide-symmetry waveguide resonator devices. (a-e) The experimental transmission spectra for different lengths exhibit clear Fabry-Pérot resonances in both bands in agreement with (f) the calculated dispersion relation. (g-l) The extracted group index agrees very well with theory for the shorter devices, but for longer devices, the limited signal-to-noise ratio around the group-index maximum makes it difficult to discern between different loss mechanisms. The theory curves have been shifted by 21 nm to compensate for fabrication imperfections.

This device was a 40 µm long waveguide, and the transmission signal is shown in Fig. 6.7(a). The group index extracted from the experiment shows a very good correspondence with the theory as shown in Fig. 6.7c. This transmission could be reproduced in the 5 different realizations of the same device (Appendix B, Fig. B.2) with the same alignment. However, after realigning the mirrors, this transmission could neither be reconstructed or be reproduced for any lengths.

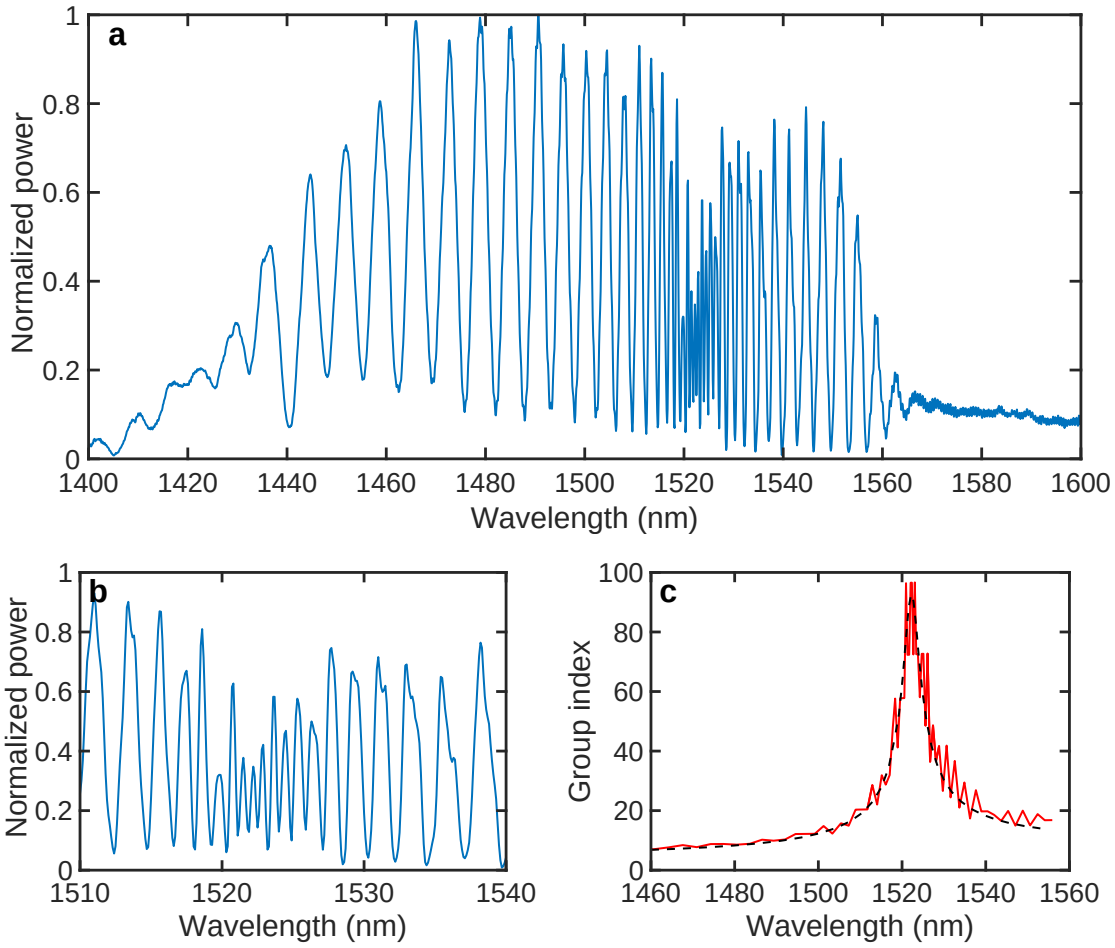

Figure 6.7: Test case with improved coupling. (a) A high quality transmission reading was measured on one of the several glide-symmetry waveguides measured. (b) The transmission spectrum narrowed around the slow-light region shows a noise-free high-quality Fabry-Pérot fringe pattern. This spectrum maps out a smooth group index as shown in (c): the solid red line is the experimental group index, and the dashed black line is from theory. Theory and experiment show good correspondence.

6.3 Coupling through nanobeam waveguide

The resonator setup raised a number of challenges in terms of coupling and observation of important features like the band crossing at the Brillouin zone edge. This setup also failed to characterize long devices ($> 160\,\mu m$) as it was restrained by the limitations set by the field of view of the objective; and hence changes had to be made in coupling strategies. A schematic of the basic setup is shown in Fig. 6.8. The standard photonic-crystal waveguide is connected to the circular grating via a suspended access waveguide or nanobeams. The two gratings are oriented orthogonal to each other to filter out scattered light at the input grating which would otherwise impair the quality of the collected signal. Another improvement to this device was the addition of a fast section at the photonic-crystal and access-waveguide interface, which improved the coupling of light into slow-light modes (see Sec. 3.1.3).

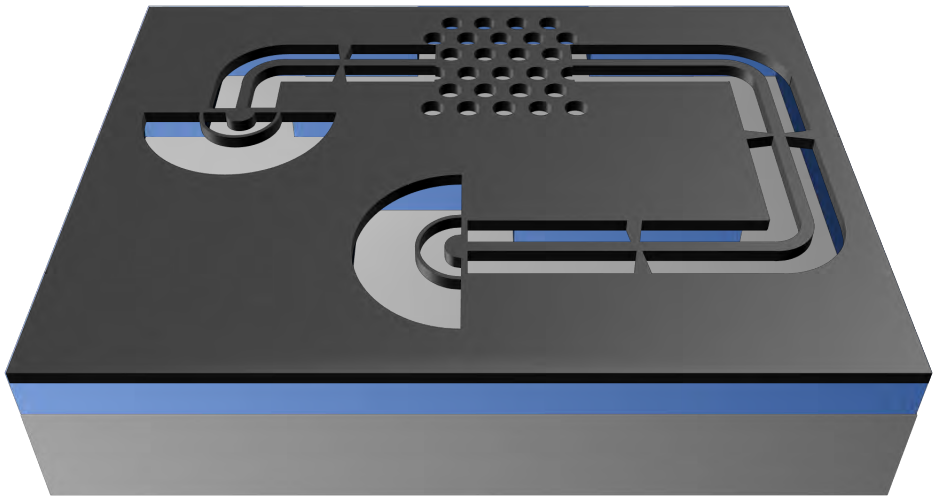

Figure 6.8: Waveguide circuit illustration. Image showing the circuit of the current design on a silicon-on-insulator platform.The photonic structure is fabricated as a free-standing membrane structure. The circular grating is connected to the photonic-crystal waveguide via a tethered waveguide section. The incident and collection gratings are positioned orthogonal to each other in order to suppress the collection of light from direct laser scattering.

Figure 6.9: Cut-back method. A bright-field microscopic image of the fabricated devices in the orthogonal setup. The length of the photonic-crystal waveguide varies from 200 µm to 1000 µm, whereas the net-length of the access waveguide remains unchanged.

A cut-back measurement technique is used where the length of the access waveguides are kept the same, but the lengths of the photonic-crystal waveguides are changed (Fig. 6.9). This makes it possible to measure waveguides varying from micrometer to millimeter in length. This technique has the unique ability to determine the optical transmission characteristics without introducing any errors due to inconsistent coupling conditions. Transmission through plain suspended waveguides of similar lengths were also measured for reference.

Fig. 6.10(a-b) shows the TE-mode transmission spectra of glide-symmetry waveguides (blue) for two different lengths of 25 µm and 250 µm along with the spectrum from a reference suspended waveguide (red). Comparing the spectra of glide-symmetry waveguides with the reference waveguide, it can be clearly seen that the transmission is dominated by the photonic crystal spectrum. The spectra is modulated by interference fringes that arise from small cavities formed by suspended waveguides, spurious reflections at tethers or mode mismatch at dissimilar structures. The corresponding dispersion diagram is plotted in Fig. 6.10(c) which shows a good agreement with the experiment. Here, the important spectral features ob-

served in the transmission spectrum can be clearly mapped with the features in the dispersion curve.

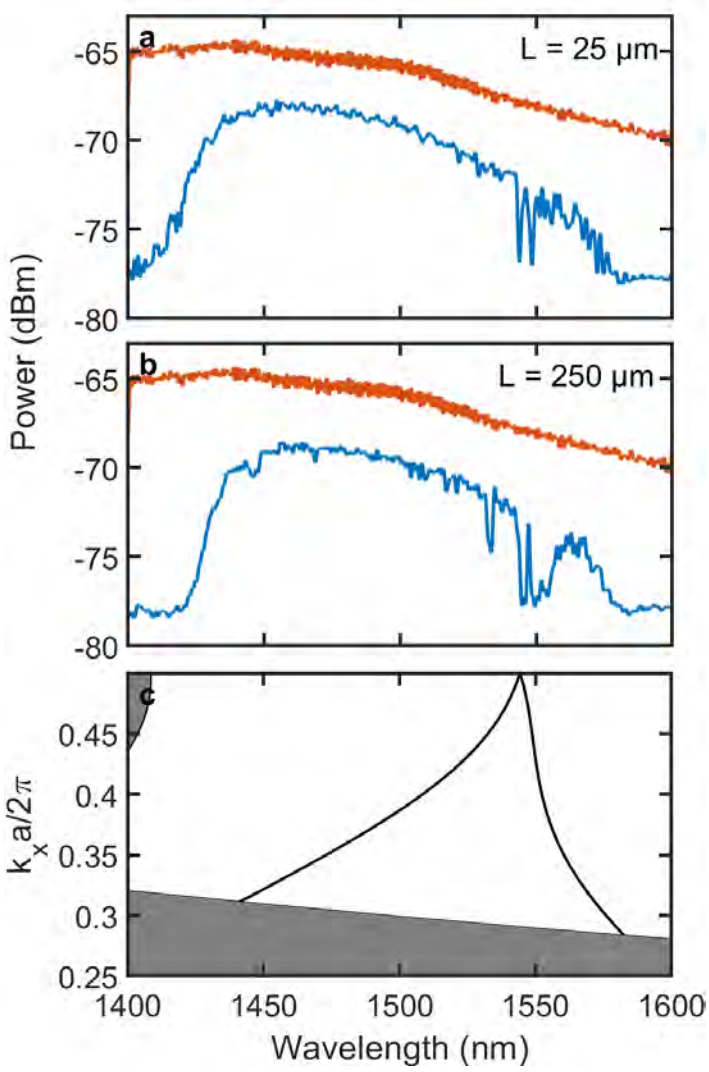

Figure 6.10: Transmission spectra comparison. Transmission spectra of a 25 µm and a 250 µm long glide-symmetry waveguide through the setup is shown in (a) and (b). A drop in transmission is observed at 1544 nm and 1549 nm for both the waveguides. For long waveguide, both cross-over point and slow-light region shows sufficient broadening. (c) The dispersion diagram has been shifted by 18.5 nm. The band-crossing and slow-light regions are located at 1544 nm and 1549 nm respectively.

For the shorter device, a narrow drop in transmission is observed at 1544 nm and 1549 nm which appear to correspond to the band-crossing feature (1544 nm) and the slow-light region (1548 nm) in the dispersion map. For the longer device, these two features are still observed at 1545 nm and 1549 nm respectively, but slightly broadened. The development of the trough coinciding with the maximum group index raises a number of questions. This is a single realization and hence not much can be inferred from these transmission dips. However, the sharp features emerging around the slow light could indicate the formation of Anderson-localized modes and this calls for further investigations.

This experiment was repeated with devices, which were on the order of few millimeters in length. The transmission spectra for 0.5 mm (blue) and 2.5 mm (red) long devices is shown in Fig. 6.11(a) along with the dispersion diagram Fig. 6.11(b). Referring to the dispersion diagram, the transmission spectrum can be distinguished into three different sections:

- 1425 nm - 1450 nm: Transmission is strongly attenuated. This is the region above the light line, where the slab modes are considered to be leaky and can no longer propagate as they suffer from radiation losses [170].
- 1450 nm - 1540 nm: Transmission remains high with significant propagation losses. These are the guided modes that propagate as Bloch waves and suffer from losses induced by nanometer-scale disorder.
- 1545 nm - 1550 nm: Transmission is strongly suppressed. It is difficult to discern among various scattering mechanisms because the transmission is very close to the noise floor and not much information is available. The work presented in the final section is motivated by the possibility to study multiple scattering in slow-light regime such as these.

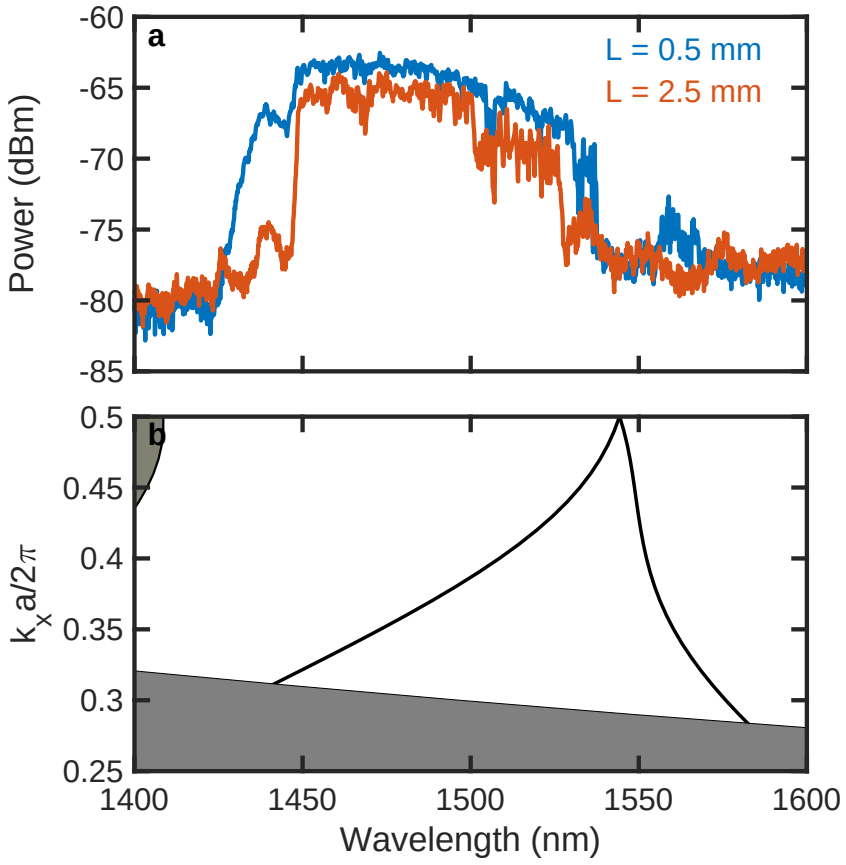

Figure 6.11: Transmission spectra comparison of millimeter long devices. (a) Transmission spectra of 0.5 mm and a 2.5 mm long glide-symmetry photonic-crystal waveguide through access nanobeam waveguide interface. (b) The corresponding dispersion curve can be used to map different points of interest in the transmission spectra. The theory is shifted by 18.5 nm to compensate for irregularities arising from fabrication.

6.4 Measuring localization length and multiple scattering

Disordered systems are characterized by the formation of random localized modes by multiple scattering events. This is known as Anderson localization and was first studied for the propagation of waves in disordered metals [112]. This phenomenon can also be studied in optical systems because of the wave nature of light, and since then has opened new avenues for various applications such as random lasing and cavity quantum-electrodynamics [95, 116]. Photonic crystals are not impervious to this phenomenon and have been an ideal platform for observing Anderson localization in one-dimensional waveguides. The unavoidable fabrication imperfections provide a means of disorder for light to undergo multiple scattering before coming to a standstill.

A key feature to studying this phenomenon is the localization length, ξ. The localized modes are characterized by electric fields whose intensity decays exponentially in space as $e^{-r/\xi}$. It is an ensemble-averaged statistical parameter, which is key to understanding the interaction strength between light and matter in strongly correlated systems.

Most of the attempts to observe Anderson localization have been limited to measuring the transmission peaks by adding artificially created disorder into an ordered system and measuring this key parameter [166, 171]. However, it is quite complex and requires measuring on a number of realizations to include the randomness of localized modes, or ensemble averaging.

Here, a convenient and easy method to measure the localization length is proposed. The ratio of localization length to sample length is a critical criterion for observing Anderson localization. Depending on this ratio, three different regimes can be identified and defined as shown in Fig. 6.12. For device lengths shorter than the localization length, photons have a ballistic transport with high transmission. Close to the localization length, randomly localized cavities are formed, and some of the light will leak out. It will be possible to observe the transmission through these de-

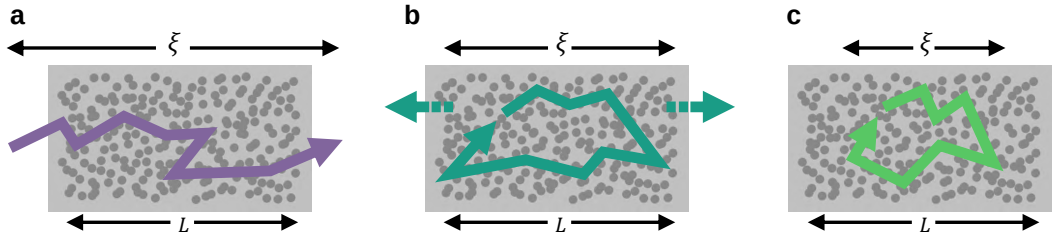

Figure 6.12: Scheme to measure localization length. Different regimes of wave-propagation in a random one-dimensional medium of length L compared to the localization length ξ: ballistic transmission where $L < \xi$ (a), critical leaky-transmission $L \approx \xi$ (b), and halted transmission $L > \xi$(c).

vices, and the cavities would show up as random peaks. For longer devices, modes are strongly localized since they are well within the localization regime and hence no transmission is observed.

In the above context, a simple method to measure the localization length in one-dimensional systems is derived. The dispersion in localization length is a crucial ingredient of this method [166]. It is known that for a photonic-crystal waveguide, the localization length $\xi(\lambda)$ is proportional to the optical density of states $\rho(\lambda)$, and scales as $\xi \propto \rho^{-2}(\lambda)$ [91]. Furthermore, $n_{\mathrm{g}}(\lambda) \propto \rho(\lambda)$ and therefore $\xi(\lambda) \propto n_{\mathrm{g}}^{-2}(\lambda)$. Here, it can be seen that for larger group-index values, the localization length decreases, thus impairing slow-light propagating over long distances. Since all the devices are fabricated on the same sample, a uniform structural-disorder can be considered for all the samples, and hence $\xi(\lambda)$ remains constant for each waveguide design.

The Thouless criterion is a strong criterion used to identify the occurrence of localization in an extended system [169]. Localization can be identified based on fluctuations in conductance brought about by scaling the boundary conditions [172]. The criterion distinguishing localized and non-localized modes can be defined by the Thouless number given by,

$$\delta\lambda/\Delta\lambda_{\mathrm{FSR}} > 1 \tag{6.1}$$

where $\delta\lambda$ is the half-width of the sharp peak and $\Delta\lambda_{\mathrm{FSR}}$ is the spacing between

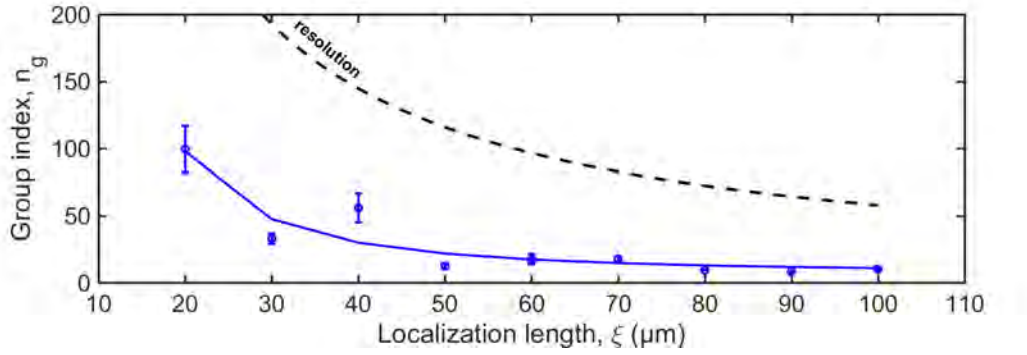

Figure 6.13: Localization length measured in W1 waveguides. (a) The maximum group index along with error bars are plotted for different lengths after ensemble averaging for W1 waveguides of lengths varying from 20 nm to 100 nm. The raw data shows a good fit with the theory. Black dashed line shows the highest possible group index that can be measured with the spatial resolution of 0.1 nm.

the modes. Using this theory, a qualitative criterion can be defined for cavities to determine if the observed transmission has localized modes or not. Before applying this criteria, transmission peaks of the cavity must be subtracted. This information is directly available in the experimentally extracted group index, where random cavities would show up as large deviations from the group index calculated for a perfect structure. A normalized deviation can be defined as,

$$\delta(\lambda) = \frac{|n_{\mathrm{g}}^{\mathrm{exp}}(\lambda) - n_{\mathrm{g}}^{\mathrm{the}}(\lambda)|}{n_{\mathrm{g}}^{\mathrm{exp}}(\lambda) + n_{\mathrm{g}}^{\mathrm{the}}(\lambda)}, \tag{6.2}$$

where $n_{\mathrm{g}}^{\mathrm{exp}}(\lambda)$ denotes the group index extracted from experiment and $n_{\mathrm{g}}^{\mathrm{the}}(\lambda)$ is the group index calculated for an ordered structure. To apply this criterion, the deviation must be more than a chosen value $\delta(\lambda_0) > 0.2$, where λ_0 is the maximum wavelength at which group index behaves well, before it is disturbed by the onset of Anderson localization. The modes are localized when the sample length L almost exceeds the localization length ξ (see Fig. 6.12b. Hence the localization length can be approximated to be the same as the sample length, i.e., $\xi(\lambda_0) = L$. By measuring λ_0 in waveguides of different lengths, the dependence $\xi(\lambda) \propto n_{\mathrm{g}}^{-2}(\lambda)$ can be plotted directly.

Anderson localization is a statistical phenomenon and therefore the entire data set

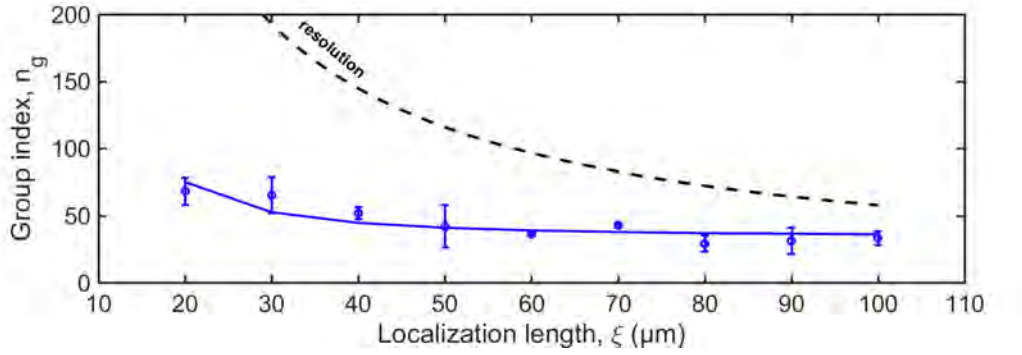

Figure 6.14: Localization length measurement for glide-symmetry waveguides. (a) The maximum group index at the cut-off wavelength is plotted for different lengths after ensemble averaging for glide-symmetry waveguides of lengths varying from 20 nm to 100 nm and show a good fit with the model. Black dashed line shows the highest possible group index that can be measured with the spatial resolution of 0.1 nm.

with five identical samples for each length and waveguide type is used to calculate the average of the maximum group index $\delta(\lambda_0)$ (see Appendix B, Fig. B.4). The result is shown in Fig. 6.13 for a W1 waveguide, where the average maximum group index $\delta(\lambda_0)$ is plotted against localization length, ξ. The error bars are large for the shorter lengths. This is because as the group index diverges rapidly and for shorter devices, microscopic fluctuation along the wavelength would give rise to a large deviation in the group index, resulting in a larger variance in the average values. The plot shows a good agreement with the predicted scaling of $n_g \propto \xi^{-2}$ thus confirming the validity of this model.

Further, the same method is applied to calculate the localization length in the glide-symmetry waveguides where a high group index has been measured and this is shown in Fig. 6.14. It can be observed that the glide-symmetric waveguides exhibits the same scaling as W1 waveguides. However, the localization length for larger group indices is shorter compared to W1 waveguides indicating early onset of Anderson localization, and hence more sensitive to loss channels. For these measurements, a bin-size of 0.1 nm is used, which sets an upper bound to the measurable group index, indicated by the dashed line in Figs. 6.13 and 6.14.

The main ingredients in this method are the dispersive nature of localization length, and the ability to create resonators, where light can bounce back and forth. Hence,it is also important to note that the full extent of the aforementioned method works mainly for one-dimensional systems. For disordered two- or three-dimensional systems, it is formally possible but the complications involved in measuring transmission and building resonators make it practically unfeasible.

7

Conclusion

A reliable and highly-reproducible optimized recipe to fabricate photonic-crystal waveguides on a silicon-on-insulator platform has been developed and reported. Glide-symmetry waveguides have been shown to possess interesting properties which are key towards realizing highly directional emission of photons, hence the interest in characterizing these device. Further, following an experimental investigation, a criterion is developed to qualitatively measure a key parameter, the localization length in one-dimensional disordered structures.

The mature fabrication-process and tailored optical-properties make silicon an ideal platform for high-density integration of photonic devices. A process recipe to fabricate photonic devices on silicon-on-insulator has been developed. The recipe has been optimized for the correct dimensions by following an iterative approach. Practical concerns like stitching errors and proximity effects have been understood and appropriate measures have been proposed to minimize their effects. This process recipe has been successfully employed to fabricate W1-photonic crystals, glide-symmetry photonic crystals and photonic circuits with appreciable good results.

The transmission properties of the glide-symmetry waveguide resonators have been studied and compared to the measurements of a standard W1 photonic-crystal waveguide. Over 120 resonator devices have been measured and studied to get a statistical overview of its behavior. The slow-light phenomenon has been observed and group indices over 90 have been measured in glide-symmetry waveguides, which makes them a promising candidate for slow-light technology and enhancing chiral properties of light.

The increased sensitivity of slow-light to fabrication disorder is known for a while.

It has been shown that this further develops and leads to the formation of random modes that are highly localized around the defects, thus ceasing any propagation. A key parameter to measure this localization effect is the localization length. A novel and simple method to measure the localization length has been proposed. A relation between the group index and the localization length parameter is derived, and measurements show a good agreement with the theory, hence validating the model.

Prospects

The high group indices observed in the glide-symmetry waveguides make them a promising candidate for studying chiral light-matter interactions at the most fundamental level. Other phenomena such as deterministic chiral light-emission and spin-orbit coupling could be conceived using the glide-symmetry design.

The current setup with the combination of supercontinuum light-source and optical spectrum analyzer had some limitations in detecting much finer features. These localized modes would usually appear with a higher prominance for longer devices. Hence using a tunable laser-source to characterize this device would allow the possibility to resolve much finer features with a higher resolution. Christian Anker Rosiek has been working on a setup to use a high performance tunable laser and a photodetector to conduct experiments on the glide-symmetry waveguides. This setup can answer some questions related to the suppression of backscattering effects by glide-symmetry around the linear landscape of band-crossing. It has also been observed that coupling light into the slow light modes of glide-symmetry waveguide has been a challenging task. Christian is working on a further step towards improving the coupling interface between optical elements with large mode mismatch.

Slow-light operating over a large bandwidth is an important requirement for many applications. The dispersion of the glide-symmetry waveguides can be further engineered to realize a hockey-stick shaped band-structure, which should increase the flat band bandwidth for slow-light operations.

Comparative investigations reveal that the glide-symmetric waveguides exhibit the same scaling as W1 photonic-crystal waveguides for localization lengths, but the

localization length for larger group indices is shorter in glide-symmetry waveguides. This indicates that the glide-symmetry waveguides are more lossy than W1 photonic-crystal waveguides. Studying the losses around the band-crossing feature could reveal if the glide-symmetry shows any interesting behavior suppressing backscattering events. The orbital angular momentum of light was for the first time calculated theoretically in a glide-symmetry waveguide [24]. Rigorous investigations of these waveguides can lead to the experimental observation of spin-orbit coupling at the nanoscale levels.

Bibliography

[1] A. L. Schawlow and C. H. Townes, "Infrared and optical masers," Phys. Rev. **112**, 1940 (1958).

[2] T. H. Maiman, "Stimulated Optical Radiation in Ruby," Nature **187**, 493–494 (1960).

[3] H. H. Hopkins and N. S. Kapany, "A flexible fibrescope, using static scanning," Nature **173**, 39 (1954).

[4] P. Lodahl, S. Mahmoodian, S. Stobbe, A. Rauschenbeutel, P. Schneeweiss, J. Volz, H. Pichler, and P. Zoller, "Chiral quantum optics," Nature **541**, 473–480 (2017).

[5] F. Flamini, N. Spagnolo, and F. Sciarrino, "Photonic quantum information processing: a review," Rep. Prog. Phys. **82**, 016001 (2018).

[6] S. Nakamura, "GaN growth using GaN buffer layer," Jpn. J. Appl. Phys. **30**, L1705 (1991).

[7] H. Amano, N. Sawaki, I. Akasaki, and Y. Toyoda, "Metalorganic vapor phase epitaxial growth of a high quality GaN film using an AlN buffer layer," Appl. Phys. Lett. **48**, 353–355 (1986).

[8] E. Betzig, G. H. Patterson, R. Sougrat, O. W. Lindwasser, S. Olenych, J. S. Bonifacino, M. W. Davidson, J. Lippincott-Schwartz, and H. F. Hess, "Imaging intracellular fluorescent proteins at nanometer resolution," Science **313**, 1642–1645 (2006).

[9] A. Ashkin, J. M. Dziedzic, J. Bjorkholm, and S. Chu, "Observation of a single-beam gradient force optical trap for dielectric particles," Opt. Lett. **11**, 288–290 (1986).

[10] D. Strickland and G. Mourou, "Compression of amplified chirped optical pulses," Opt. Commun. **55**, 447–449 (1985).

[11] P. Russell, "Photonic crystal fibers," Science **299**, 358–362 (2003).

[12] S. De Wolf, A. Descoeudres, Z. C. Holman, and C. Ballif, "High-efficiency silicon heterojunction solar cells: A review," green **2**, 7–24 (2012).

[13] M. Ohtsu, *Silicon Light-Emitting Diodes and Lasers* (Springer, 2016).

[14] Y. Yu, W. Xue, E. Semenova, K. Yvind, and J. Mork, "Demonstration of a self-pulsing photonic crystal fano laser," Nat. Photon. **11**, 81 (2017).

[15] D. Pérez, I. Gasulla, L. Crudgington, D. J. Thomson, A. Z. Khokhar, K. Li, W. Cao, G. Z. Mashanovich, and J. Capmany, "Multipurpose silicon photonics signal processor core," Nat. Commun. **8**, 636 (2017).

[16] A. Di Falco, L. O'faolain, and T. Krauss, "Chemical sensing in slotted photonic crystal heterostructure cavities," Appl. Phys. Lett. **94**, 063503 (2009).

[17] M. Arcari, I. Söllner, A. Javadi, S. L. Hansen, S. Mahmoodian, J. Liu, H. Thyrrestrup, E. H. Lee, J. D. Song, S. Stobbe, and P. Lodahl, "Near-unity coupling efficiency of a quantum emitter to a photonic crystal waveguide," Phys. Rev. Lett. **113**, 093603 (2014).

[18] M. Kawachi, "Silica waveguides on silicon and their application to integrated-optic components," Opt. Quant. Electron. **22**, 391–416 (1990).

[19] S. M. Spillane, T. J. Kippenberg, and K. J. Vahala, "Ultralow-threshold Raman laser using a spherical dielectric microcavity," Nature **415**, 621 (2002).

[20] H. Kosaka, T. Kawashima, A. Tomita, M. Notomi, T. Tamamura, T. Sato, and S. Kawakami, "Superprism phenomena in photonic crystals," Phys. Rev. B **58**, R10096 (1998).

[21] T. F. Krauss, "Why do we need slow light?" Nat. Photon. **2**, 448 (2008).

[22] J. D. Joannopoulos, S. G. Johnson, J. N. Winn, and R. D. Meade, *Photonic Crystals: Molding the Flow of Light - Second Edition* (Princeton University Press, 2008), rev - revised, 2 ed.

[23] W. Kuang and J. D. O'Brien, "Reducing the out-of-plane radiation loss of photonic crystal waveguides on high-index substrates," Opt. Lett. **29**, 860–862 (2004).

[24] M. Sotto, K. Debnath, I. Tomita, and S. Saito, "Spin-orbit coupling of light in photonic crystal waveguides," Phys. Rev. A **99**, 053845 (2019).

[25] M. Sotto, K. Debnath, A. Z. Khokhar, I. Tomita, D. Thomson, and S. Saito, "Anomalous zero-group-velocity photonic bonding states with local chirality," J. Opt. Soc. Am. B **35**, 2356–2363 (2018).

[26] L. O'Faolain, X. Yuan, D. McIntyre, S. Thoms, H. Chong, R. De La Rue, and T. F. Krauss, "Low-loss propagation in photonic crystal waveguides," Electron. Lett. **42**, 1454–1455 (2006).

[27] Y. A. Vlasov, M. O'Boyle, H. F. Hamann, and S. J. McNab, "Active control of slow light on a chip with photonic crystal waveguides," Nature **438**, 65–69 (2005).

[28] J. Li, T. P. White, L. O'Faolain, A. Gomez-Iglesias, and T. F. Krauss, "Systematic design of flat band slow light in photonic crystal waveguides," Opt. Express **16**, 6227–6232 (2008).

[29] T. F. Krauss, "Slow light in photonic crystal waveguides," J. Phys. D **40**, 2666 (2007).

[30] T. Baba, "Slow light in photonic crystals," Nat. Photon. **2**, 465–473 (2008).

[31] M. Lončar, T. Doll, J. Vučković, and A. Scherer, "Design and fabrication of silicon photonic crystal optical waveguides," J. Light. Technol. **18**, 1402 (2000).

[32] I. Söllner, S. Mahmoodian, S. L. Hansen, L. Midolo, A. Javadi, G. Kiršanskė, T. Pregnolato, H. El-Ella, E. H. Lee, J. D. Song, S. Stobbe, and P. Lodahl, "Deterministic photon–emitter coupling in chiral photonic circuits," Nat. Nanotechnol. **10**, 775–778 (2015).

[33] S. Barik, A. Karasahin, C. Flower, T. Cai, H. Miyake, W. DeGottardi, M. Hafezi, and E. Waks, "A topological quantum optics interface," Science **359**, 666–668 (2018).

[34] L. Lu, Z. Wang, D. Ye, L. Ran, L. Fu, J. D. Joannopoulos, and M. Soljačić, "Experimental observation of weyl points," Science **349**, 622–624 (2015).

[35] W.-J. Chen, M. Xiao, and C. T. Chan, "Photonic crystals possessing multiple weyl points and the experimental observation of robust surface states," Nat.

Commun. **7**, 13038 (2016).

[36] T. Ma and G. Shvets, "All-si valley-hall photonic topological insulator," New J. Phys. **18**, 025012 (2016).

[37] X.-T. He, E.-T. Liang, J.-J. Yuan, H.-Y. Qiu, X.-D. Chen, F.-L. Zhao, and J.-W. Dong, "A silicon-on-insulator slab for topological valley transport," Nat. Commun. **10**, 872 (2019).

[38] L. Rayleigh, "XVII. on the maintenance of vibrations by forces of double frequency, and on the propagation of waves through a medium endowed with a periodic structure," Philos. Mag. **24**, 145–159 (1887).

[39] C. G. Darwin, "Lxxviii. the theory of x-ray reflexion. part ii," Philos. Mag. **27**, 675–690 (1914).

[40] K. Ohtaka, "Energy band of photons and low-energy photon diffraction," Phys. Rev. B **19**, 5057 (1979).

[41] E. Yablonovitch, "Inhibited spontaneous emission in solid-state physics and electronics," Phys. Rev. Lett. **58**, 2059 (1987).

[42] S. John, "Strong localization of photons in certain disordered dielectric superlattices," Phys. Rev. Lett. **58**, 2486 (1987).

[43] J. P. Vigneron and P. Simonis, "Natural photonic crystals," Physica B **407**, 4032–4036 (2012).

[44] S. Noda, A. Chutinan, and M. Imada, "Trapping and emission of photons by a single defect in a photonic bandgap structure," Nature **407**, 608 (2000).

[45] O. Painter, R. Lee, A. Scherer, A. Yariv, J. O'brien, P. Dapkus, and I. Kim, "Two-dimensional photonic band-gap defect mode laser," Science **284**, 1819–1821 (1999).

[46] P. Michler, A. Kiraz, C. Becher, W. Schoenfeld, P. Petroff, L. Zhang, E. Hu, and A. Imamoglu, "A quantum dot single-photon turnstile device," Science **290**, 2282–2285 (2000).

[47] A. Ovsianikov, A. Gaidukeviciute, B. Chichkov, M. Oubaha, B. MacCraith, I. Sakellari, A. Giakoumaki, D. Gray, M. Vamvakaki, M. Farsari *et al.*, "Two-photon polymerization of hybrid sol-gel materials for photonics applications," Laser Chem. **2008** (2008).

[48] K. Ho, C. T. Chan, and C. M. Soukoulis, "Existence of a photonic gap in periodic dielectric structures," Phys. Rev. Lett. **65**, 3152 (1990).

[49] E. Yablonovitch, T. Gmitter, and K.-M. Leung, "Photonic band structure: The face-centered-cubic case employing nonspherical atoms," Phys. Rev. Lett. **67**, 2295 (1991).

[50] M. Notomi, A. Shinya, K. Yamada, J.-I. Takahashi, C. Takahashi, and I. Yokohama, "Structural tuning of guiding modes of line-defect waveguides of silicon-on-insulator photonic crystal slabs," IEEE J. Quantum Electron. **38**, 736–742 (2002).

[51] E. Chow, S. Lin, S. Johnson, P. Villeneuve, J. Joannopoulos, J. R. Wendt, G. A. Vawter, W. Zubrzycki, H. Hou, and A. Alleman, "Three-dimensional control of light in a two-dimensional photonic crystal slab," Nature **407**, 983 (2000).

[52] S. J. McNab, N. Moll, and Y. A. Vlasov, "Ultra-low loss photonic integrated circuit with membrane-type photonic crystal waveguides," Opt. Express **11**, 2927–2939 (2003).

[53] A. Mock, L. Lu, and J. O'Brien, "Space group theory and fourier space analysis of two-dimensional photonic crystal waveguides," Phys. Rev. B **81**, 155115 (2010).

[54] L. Midolo, T. Pregnolato, G. Kiršanskė, and S. Stobbe, "Soft-mask fabrication of gallium arsenide nanomembranes for integrated quantum photonics," Nanotechnology **26**, 484002 (2015).

[55] N. Le Thomas, H. Zhang, J. Jágerská, V. Zabelin, R. Houdré, I. Sagnes, and A. Talneau, "Light transport regimes in slow light photonic crystal waveguides," Phys. Rev. B **80**, 125332 (2009).

[56] B. Corcoran, C. Monat, C. Grillet, D. J. Moss, B. J. Eggleton, T. P. White, L. O'Faolain, and T. F. Krauss, "Green light emission in silicon through slow-light enhanced third-harmonic generation in photonic-crystal waveguides," Nat. Photon. **3**, 206 (2009).

[57] M. Inoue and K. Ohtaka, "Enhanced Raman scattering by a two-dimensional array of dielectric spheres," Phys. Rev. B **26**, 3487 (1982).

[58] S. G. Johnson, "Photonic crystals: from theory to practice," Ph.D. thesis, Massachusetts Institute of Technology (2001).

[59] K. Tsuruda, M. Fujita, and T. Nagatsuma, "Extremely low-loss terahertz waveguide based on silicon photonic-crystal slab," Opt. Express **23**, 31977–31990 (2015).

[60] S. Fan, P. R. Villeneuve, J. Joannopoulos, and E. Schubert, "High extraction efficiency of spontaneous emission from slabs of photonic crystals," Phys. Rev. Lett. **78**, 3294 (1997).

[61] M. Notomi, K. Yamada, A. Shinya, J. Takahashi, C. Takahashi, and I. Yokohama, "Extremely large group-velocity dispersion of line-defect waveguides in photonic crystal slabs," Phys. Rev. Lett. **87**, 253902 (2001).

[62] L. H. Frandsen, A. V. Lavrinenko, J. Fage-Pedersen, and P. I. Borel, "Photonic crystal waveguides with semi-slow light and tailored dispersion properties," Opt. Express **14**, 9444–9450 (2006).

[63] B.-S. Song, S. Noda, and T. Asano, "Photonic devices based on in-plane hetero photonic crystals," Science **300**, 1537–1537 (2003).

[64] J. Mork, Y. Chen, and M. Heuck, "Photonic crystal Fano laser: terahertz modulation and ultrashort pulse generation," Phys. Rev. Lett. **113**, 163901 (2014).

[65] Y. Akahane, T. Asano, B.-S. Song, and S. Noda, "High-Q photonic nanocavity in a two-dimensional photonic crystal," Nature **425**, 944 (2003).

[66] K. Debnath, M. Clementi, T. D. Bucio, A. Z. Khokhar, M. Sotto, K. M. Grabska, D. Bajoni, M. Galli, S. Saito, and F. Y. Gardes, "Ultrahigh-Q photonic crystal cavities in silicon rich nitride," Optics express **25**, 27334–27340 (2017).

[67] A. Mekis, J. C. Chen, I. Kurland, S. Fan, P. R. Villeneuve, and J. D. Joannopoulos, "High transmission through sharp bends in photonic crystal waveguides," Phys. Rev. Lett. **77**, 3787 (1996).

[68] V. R. Almeida, Q. Xu, C. A. Barrios, and M. Lipson, "Guiding and confining light in void nanostructure," Opt. Lett. **29**, 1209–1211 (2004).

[69] M. G. Scullion, T. F. Krauss, and A. Di Falco, "Slotted photonic crystal sensors," Sensors **13**, 3675–3710 (2013).

[70] A. Shinya, T. Tanabe, E. Kuramochi, and M. Notomi, "All-optical switch and digital light processing using photonic crystals," NTT Technical Review **3**, 61–68 (2005).

[71] I. Fushman, E. Waks, D. Englund, N. Stoltz, P. Petroff, and J. Vučković, "Ultrafast nonlinear optical tuning of photonic crystal cavities," Appl. Phys. Lett. **90**, 091118 (2007).

[72] S. Fan, P. R. Villeneuve, J. D. Joannopoulos, and H. A. Haus, "Channel drop filters in photonic crystals," Opt. Express **3**, 4–11 (1998).

[73] Y. Guo, Y. Wang, M. Pu, Z. Zhao, X. Wu, X. Ma, C. Wang, L. Yan, and X. Luo, "Dispersion management of anisotropic metamirror for super-octave bandwidth polarization conversion," Sci. Rep. **5**, 8434 (2015).

[74] H. Kosaka, T. Kawashima, A. Tomita, M. Notomi, T. Tamamura, T. Sato, and S. Kawakami, "Self-collimating phenomena in photonic crystals," Appl. Phys. Lett. **74**, 1212–1214 (1999).

[75] D. N. Chigrin, S. Enoch, C. M. S. Torres, and G. Tayeb, "Self-guiding in two-dimensional photonic crystals," Opt. Express **11**, 1203–1211 (2003).

[76] A. Berrier, M. Mulot, M. Swillo, M. Qiu, L. Thylén, A. Talneau, and S. Anand, "Negative refraction at infrared wavelengths in a two-dimensional photonic crystal," Phys. Rev. Lett. **93**, 073902 (2004).

[77] L. V. Hau, S. E. Harris, Z. Dutton, and C. H. Behroozi, "Light speed reduction to 17 metres per second in an ultracold atomic gas," Nature **397**, 594 (1999).

[78] T. Baba, "Slow light in photonic crystals," Nat. Photon. **2**, 465 (2008).

[79] Z. Shi, R. W. Boyd, R. M. Camacho, P. K. Vudyasetu, and J. C. Howell, "Slow-light Fourier transform interferometer," Phys. Rev. Lett. **99**, 240801 (2007).

[80] R. Hayakawa, N. Ishikura, H. C. Nguyen, and T. Baba, "High-speed delay tuning of slow light in pin-diode-incorporated photonic crystal waveguide," Opt. Lett. **38**, 2680–2682 (2013).

[81] D. M. Beggs, T. P. White, L. O'Faolain, and T. F. Krauss, "Ultracompact and low-power optical switch based on silicon photonic crystals," Opt. Lett. **33**, 147–149 (2008).

[82] A. Opheij, N. Rotenberg, D. M. Beggs, I. H. Rey, T. F. Krauss, and L. Kuipers, "Ultracompact (3 μm) silicon slow-light optical modulator," Sci. Rep. **3**, 3546 (2013).

[83] W.-C. Lai, S. Chakravarty, X. Wang, C. Lin, and R. T. Chen, "Photonic crystal slot waveguide absorption spectrometer for on-chip near-infrared spectroscopy of xylene in water," Appl. Phys. Lett. **98**, 7 (2011).

[84] W.-C. Lai, S. Chakravarty, X. Wang, C. Lin, and R. T. Chen, "On-chip methane sensing by near-IR absorption signatures in a photonic crystal slot waveguide," Opt. Lett. **36**, 984–986 (2011).

[85] Z. Shi and R. W. Boyd, "Slow-light enhanced spectrometers on chip," in *Photonics North 2011,* vol. 8007 (International Society for Optics and Photonics, 2011), p. 80071D.

[86] M. Soljačić and J. D. Joannopoulos, "Enhancement of nonlinear effects using photonic crystals," Nat. Mater. **3**, 211 (2004).

[87] Z. Shi, R. W. Boyd, D. J. Gauthier, and C. Dudley, "Enhancing the spectral sensitivity of interferometers using slow-light media," Opt. Lett. **32**, 915–917 (2007).

[88] J. Arlandis, E. Centeno, R. Polles, A. Moreau, J. Campos, O. Gauthier-Lafaye, and A. Monmayrant, "Mesoscopic self-collimation and slow light in all-positive index layered photonic crystals," Phys. Rev. Lett. **108**, 037401 (2012).

[89] C. Monat, M. Ebnali-Heidari, C. Grillet, B. Corcoran, B. J. Eggleton, T. White, L. O'Faolain, J. Li, and T. F. Krauss, "Four-wave mixing in slow light engineered silicon photonic crystal waveguides," Opt. Express **18**, 22915–22927 (2010).

[90] H. Takesue, N. Matsuda, E. Kuramochi, and M. Notomi, "Entangled photons from on-chip slow light," Sci. Rep. **4**, 3913 (2014).

[91] P. Lodahl, S. Mahmoodian, and S. Stobbe, "Interfacing single photons and single quantum dots with photonic nanostructures," Rev. Mod. Phys. **87**, 347 (2015).

[92] B. Le Feber, N. Rotenberg, and L. Kuipers, "Nanophotonic control of circular dipole emission," Nat. Commun. **6**, 6695 (2015).

[93] D. Melati, A. Melloni, and F. Morichetti, "Real photonic waveguides: guiding light through imperfections," Adv. Opt. Photonics **6**, 156–224 (2014).

[94] S. Hughes, L. Ramunno, J. F. Young, and J. Sipe, "Extrinsic optical scattering loss in photonic crystal waveguides: role of fabrication disorder and photon group velocity," Phys. Rev. Lett. **94**, 033903 (2005).

[95] L. Sapienza, H. Thyrrestrup, S. Stobbe, P. D. Garcia, S. Smolka, and P. Lodahl, "Cavity quantum electrodynamics with Anderson-localized modes," Science **327**, 1352–1355 (2010).

[96] E. Kuramochi, M. Notomi, S. Hughes, A. Shinya, T. Watanabe, and L. Ramunno, "Disorder-induced scattering loss of line-defect waveguides in photonic crystal slabs," Phys. Rev. B **72**, 161318 (2005).

[97] L. Ramunno and S. Hughes, "Disorder-induced resonance shifts in high-index-contrast photonic crystal nanocavities," Phys. Rev. B **79**, 161303 (2009).

[98] W.-P. Huang, "Coupled-mode theory for optical waveguides: an overview," JOSA A **11**, 963–983 (1994).

[99] K. v. Klitzing, G. Dorda, and M. Pepper, "New method for high-accuracy determination of the fine-structure constant based on quantized hall resistance," Phys. Rev. Lett. **45**, 494 (1980).

[100] C. L. Kane and E. J. Mele, "Z 2 topological order and the quantum spin hall effect," Phys. Rev. Lett. **95**, 146802 (2005).

[101] F. Haldane and S. Raghu, "Possible realization of directional optical waveguides in photonic crystals with broken time-reversal symmetry," Phys. Rev. Lett. **100**, 013904 (2008).

[102] S. Raghu and F. D. M. Haldane, "Analogs of quantum-hall-effect edge states in photonic crystals," Phys. Rev. A **78**, 033834 (2008).

[103] Z. Wang, Y. Chong, J. D. Joannopoulos, and M. Soljačić, "Reflection-free one-way edge modes in a gyromagnetic photonic crystal," Phys. Rev. Lett. **100**, 013905 (2008).

[104] J. Koch, A. A. Houck, K. Le Hur, and S. Girvin, "Time-reversal-symmetry breaking in circuit-qed-based photon lattices," Phys. Rev. A **82**, 043811 (2010).

[105] M. Hafezi, E. A. Demler, M. D. Lukin, and J. M. Taylor, "Robust optical delay lines with topological protection," Nat. Phys. **7**, 907 (2011).

[106] A. B. Khanikaev, S. H. Mousavi, W.-K. Tse, M. Kargarian, A. H. MacDonald, and G. Shvets, "Photonic topological insulators," Nat. Mater. **12**, 233 (2013).

[107] G. Siroki, P. A. Huidobro, and V. Giannini, "Topological photonics: From crystals to particles," Phys. Rev. B **96**, 041408 (2017).

[108] P. Wang, L. Lu, and K. Bertoldi, "Topological phononic crystals with one-way elastic edge waves," Phys. Rev. Lett. **115**, 104302 (2015).

[109] S. Barik, H. Miyake, W. DeGottardi, E. Waks, and M. Hafezi, "Two-dimensionally confined topological edge states in photonic crystals," New J. Phys. **18**, 113013 (2016).

[110] M. I. Shalaev, W. Walasik, A. Tsukernik, Y. Xu, and N. M. Litchinitser, "Robust topologically protected transport in photonic crystals at telecommunication wavelengths," Nat. Nanotechnol. **14**, 31 (2019).

[111] J. Guglielmon and M. C. Rechtsman, "Broadband topological slow light through higher momentum-space winding," Phys. Rev. Lett. **122**, 153904 (2019).

[112] P. W. Anderson, "Absence of diffusion in certain random lattices," Phys. Rev. **109**, 1492 (1958).

[113] J. Topolancik, B. Ilic, and F. Vollmer, "Experimental observation of strong photon localization in disordered photonic crystal waveguides," Phys. Rev. Lett. **99**, 253901 (2007).

[114] H. H. Sheinfux, Y. Lumer, G. Ankonina, A. Z. Genack, G. Bartal, and M. Segev, "Observation of anderson localization in disordered nanophotonic structures," Science **356**, 953–956 (2017).

[115] T. Schwartz, G. Bartal, S. Fishman, and M. Segev, "Transport and Anderson localization in disordered two-dimensional photonic lattices," Nature **446**, 52 (2007).

[116] J. Liu, P. Garcia, S. Ek, N. Gregersen, T. Suhr, M. Schubert, J. Mørk, S. Stobbe, and P. Lodahl, "Random nanolasing in the anderson localized regime," Nat. Nanotechnol. **9**, 285 (2014).

[117] A. Javadi, I. Söllner, M. Arcari, S. L. Hansen, L. Midolo, S. Mahmoodian, G. Kiršanskė, T. Pregnolato, E. Lee, J. Song *et al.*, "Single-photon non-linear optics with a quantum dot in a waveguide," Nat. Commun. **6**, 8655 (2015).

[118] V. Liberman and B. Y. Zel'dovich, "Spin-orbit interaction of a photon in an inhomogeneous medium," Phys. Rev. A **46**, 5199 (1992).

[119] S. Mahmoodian, K. Prindal-Nielsen, I. Söllner, S. Stobbe, and P. Lodahl, "Engineering chiral light–matter interaction in photonic crystal waveguides with slow light," Opt. Mater. Express **7**, 43–51 (2017).

[120] S. G. Johnson and J. D. Joannopoulos, "Block-iterative frequency-domain methods for Maxwell's equations in a planewave basis," Opt. Express **8**, 173–190 (2001).

[121] W. Kuang, W. J. Kim, A. Mock, and J. O'Brien, "Propagation loss of line-defect photonic crystal slab waveguides," IEEE J. Sel. Top. Quantum Electron. **12**, 1183–1195 (2006).

[122] A. Mock and J. D. O'Brien, "Strategies for reducing the out-of-plane radiation in photonic crystal heterostructure microcavities for continuous wave laser applications," J. Light. Technol. **28**, 1042–1050 (2010).

[123] A. B. Khanikaev and G. Shvets, "Two-dimensional topological photonics," Nat. Photon. **11**, 763–773 (2017).

[124] R. Mitsch, C. Sayrin, B. Albrecht, P. Schneeweiss, and A. Rauschenbeutel, "Quantum state-controlled directional spontaneous emission of photons into a nanophotonic waveguide," Nat. Commun. **5**, 5713 (2014).

[125] J. Witzens, M. Hochberg, T. Baehr-Jones, and A. Scherer, "Mode matching interface for efficient coupling of light into planar photonic crystals," Phys. Rev. E **69**, 046609 (2004).

[126] P. Pottier, M. Gnan, and M. Richard, "Efficient coupling into slow-light photonic crystal channel guides using photonic crystal tapers," Opt. Express **15**, 6569–6575 (2007).

[127] E. Moreno, L. Martin-Moreno, and F. García-Vidal, "Efficient coupling of light into and out of a photonic crystal waveguide via surface modes," Photonics Nanostructures: Fundam. Appl. **2**, 97–102 (2004).

[128] H. S. Dutta, A. K. Goyal, V. Srivastava, and S. Pal, "Coupling light in photonic crystal waveguides: A review," Photonics Nanostructures: Fundam. Appl. **20**, 41–58 (2016).

[129] Z. Weissman and I. Hendel, "Analysis of periodically segmented waveguide mode expanders," J. Light. Technol. **13**, 2053–2058 (1995).

[130] V. R. Almeida, R. R. Panepucci, and M. Lipson, "Nanotaper for compact mode conversion," Opt. Lett. **28**, 1302–1304 (2003).

[131] E. Miyai and S. Noda, "Structural dependence of coupling between a two-dimensional photonic crystal waveguide and a wire waveguide," J. Opt. Soc. Am. B **21**, 67–72 (2004).

[132] Y. A. Vlasov and S. J. McNab, "Coupling into the slow light mode in slab-type photonic crystal waveguides," Opt. Lett. **31**, 50–52 (2006).

[133] M. Suter and P. Dietiker, "Calculation of the finesse of an ideal fabry–perot resonator," Appl. Opt. **53**, 7004–7010 (2014).

[134] A. Faraon, I. Fushman, D. Englund, N. Stoltz, P. Petroff, and J. Vučković, "Dipole induced transparency in waveguide coupled photonic crystal cavities," Opt. Express **16**, 12154–12162 (2008).

[135] J.-P. Hugonin, P. Lalanne, T. P. White, and T. F. Krauss, "Coupling into slow-mode photonic crystal waveguides," Opt. Lett. **32**, 2638–2640 (2007).

[136] C. M. De Sterke, K. Dossou, T. White, L. Botten, and R. McPhedran, "Efficient coupling into slow light photonic crystal waveguide without transition region: role of evanescent modes," Opt. Express **17**, 17338–17343 (2009).

[137] C. M. De Sterke, K. Dossou, T. White, L. Botten, and R. McPhedran, "Efficient coupling into slow light photonic crystal waveguide without transition region: role of evanescent modes," Opt. Express **17**, 17338–17343 (2009).

[138] I. A. Young, E. M. Mohammed, J. T. Liao, A. M. Kern, S. Palermo, B. A. Block, M. R. Reshotko, and P. L. Chang, "Optical technology for energy efficient i/o in high performance computing," IEEE Commun. Mag **48**, 184–191 (2010).

[139] L. Jia, J. Song, T.-Y. Liow, X. Luo, X. Tu, Q. Fang, S.-C. Koh, M. Yu, and G. Lo, "Mode size converter between high-index-contrast waveguide and

cleaved single mode fiber using sion as intermediate material," Opt. Express **22**, 23652–23660 (2014).

[140] R. Takei, E. Omoda, M. Suzuki, S. Manako, T. Kamei, M. Mori, and Y. Sakakibara, "Ultranarrow silicon inverse taper waveguide fabricated with double-patterning photolithography for low-loss spot-size converter," Appl. Phys. Express **5**, 052202 (2012).

[141] Y. A. Vlasov, M. O'boyle, H. F. Hamann, and S. J. McNab, "Active control of slow light on a chip with photonic crystal waveguides," Nature **438**, 65 (2005).

[142] J. Auerhammer, C. Hartig, K. Wendt, R. van Oostrum, G. Pfeiffer, S. Bayer, and B. Srocka, "Silicon thickness variation of fd-soi wafers investigated by differential reflective microscopy," in *2016 IEEE SOI-3D-Subthreshold Microelectronics Technology Unified Conference (S3S),* (IEEE, 2016), pp. 1–3.

[143] K. R. Williams, K. Gupta, and M. Wasilik, "Etch rates for micromachining processing-part ii," J. Microelectromech. Syst. **12**, 761–778 (2003).

[144] A. A. Tseng, K. Chen, C. D. Chen, and K. J. Ma, "Electron beam lithography in nanoscale fabrication: recent development," IEEE Trans. Electron. Packag. **26**, 141–149 (2003).

[145] A. L. Bogdanov, J. Lapointe, and J. H. Schmid, "Electron-beam lithography for photonic waveguide fabrication: Measurement of the effect of field stitching errors on optical performance and evaluation of a new compensation method," J. Vac. Sci. Technol. B **30**, 031606 (2012).

[146] R. K. Dey and B. Cui, "Stitching error reduction in electron beam lithography with in-situ feedback using self-developing resist," J. Vac. Sci. Technol. B **31**, 06F409 (2013).

[147] C. S. Wu, Y. Makiuchi, and C. Chen, *High-energy electron beam lithography for nanoscale fabrication* (InTech Europe: Rijeka, Croatia, 2010).

[148] A. Zangwill, *Physics at surfaces* (Cambridge university press, 1988).

[149] G. Owen and P. Rissman, "Proximity effect correction for electron beam lithography by equalization of background dose," J. Appl. Phys. **54**, 3573–3581 (1983).

[150] S. Wind, M. Rosenfield, G. Pepper, W. Molzen, and P. Gerber, "Proximity correction for electron beam lithography using a three-gaussian model of the electron energy distribution," J. Vac. Sci. Technol. B **7**, 1507–1512 (1989).

[151] A. Misaka, K. Harafuji, and N. Nomura, "Determination of proximity effect parameters in electron-beam lithography," J. Appl. Phys. **68**, 6472–6479 (1990).

[152] L. Ren and B. Chen, "Proximity effect in electron beam lithography," in *Proceedings. 7th International Conference on Solid-State and Integrated Circuits Technology, 2004.*, vol. 1 (IEEE, 2004), pp. 579–582.

[153] L. Stevens, R. Jonckheere, E. Froyen, S. Decoutere, and D. Lanneer, "Determination of the proximity parameters in electron beam lithography using doughnut-structures," Microelectron. Eng. **5**, 141–150 (1986).

[154] M. Parikh, "Corrections to proximity effects in electron beam lithography. II. implementation," J. Appl. Phys. **50**, 4378–4382 (1979).

[155] M. Parikh, "Corrections to proximity effects in electron beam lithograhy. III. experiments," J. Appl. Phys. **50**, 4383–4387 (1979).

[156] D. Chow, J. McDonald, D. King, W. Smith, K. Molnar, and A. Steckl, "An image processing approach to fast, efficient proximity correction for electron beam lithography," J. Vac. Sci. Technol. B **1**, 1383–1390 (1983).

[157] P. Li, "A review of proximity effect correction in electron-beam lithography," arXiv preprint arXiv:1509.05169 (2015).

[158] T. R. Figueiro, "Process modeling for proximity effect correction in electron beam lithography," Ph.D. thesis (2015).

[159] Genisys-gmbh, "Beamer," .

[160] J. Zhang, M. Fouad, M. Yavuz, and B. Cui, "Charging effect reduction in electron beam lithography with nA beam current," Microelectron. Eng. **88**, 2196–2199 (2011).

[161] S. Choi, M. Yan, L. Wang, and I. Adesida, "Ultra-dense hydrogen silsesquioxane (HSQ) structures on thin silicon nitride membranes," Microelectron. Eng. **86**, 521–523 (2009).

[162] K. Mohamed, M. Alkaisi, and R. Blaikie, "Surface charging suppression using PEDOT/PSS in the fabrication of three dimensional structures on a quartz substrate," Microelectron. Eng. **86**, 535–538 (2009).

[163] J. Li, Q. Zhang, A. Liu, W. Goh, and J. Ahn, "Technique for preventing stiction and notching effect on silicon-on-insulator microstructure," J. Vac. Sci. Technol. B **21**, 2530–2539 (2003).

[164] F. Laermer and A. Schilp, "Method of anisotropically etching silicon," (1996). US Patent 5,501,893.

[165] M. Herskind, "Experimental characterization of silicon photonic crystal waveguides with glide-plane symmetry," (2018).

[166] P. D. García, G. Kiršanskė, A. Javadi, S. Stobbe, and P. Lodahl, "Two mechanisms of disorder-induced localization in photonic-crystal waveguides," Phys. Rev. B **96**, 144201 (2017).

[167] M. W. Lee, C. Grillet, C. G. Poulton, C. Monat, C. L. Smith, E. Mägi, D. Freeman, S. Madden, B. Luther-Davies, and B. J. Eggleton, "Characterizing photonic crystal waveguides with an expanded k-space evanescent coupling technique," Opt. Express **16**, 13800–13808 (2008).

[168] R. Sarkissian and J. O'Brien, "Group index oscillations in photonic crystal waveguides," Appl. Phys. Lett. **105**, 121102 (2014).

[169] J. Edwards and D. Thouless, "Numerical studies of localization in disordered systems," J. Phys. C: Solid State Phys. **5**, 807 (1972).

[170] M. Kanskar, P. Paddon, V. Pacradouni, R. Morin, A. Busch, J. F. Young, S. Johnson, J. MacKenzie, and T. Tiedje, "Observation of leaky slab modes in an air-bridged semiconductor waveguide with a two-dimensional photonic lattice," Appl. Phys. Lett. **70**, 1438–1440 (1997).

[171] P. García, S. Smolka, S. Stobbe, and P. Lodahl, "Density of states controls Anderson localization in disordered photonic crystal waveguides," Phys. Rev. B **82**, 165103 (2010).

[172] J. Drake and A. Genack, "Observation of nonclassical optical diffusion," Phys. Rev. Lett. **63**, 259 (1989).

[173] A. Gomez-Iglesias, D. O'Brien, L. O'Faolain, A. Miller, and T. F. Krauss, "Direct measurement of the group index of photonic crystal waveguides via fourier transform spectral interferometry," Appl. Phys. Lett. **90**, 261107 (2007).

[174] S. Combrié, E. Weidner, A. DeRossi, S. Bansropun, S. Cassette, A. Talneau, and H. Benisty, "Detailed analysis by fabry-perot method of slab photonic crystal line-defect waveguides and cavities in aluminium-free material system," Opt. Express **14**, 7353–7361 (2006).

[175] R. S. Jacobsen, A. V. Lavrinenko, L. H. Frandsen, C. Peucheret, B. Zsigri, G. Moulin, J. Fage-Pedersen, and P. I. Borel, "Direct experimental and numerical determination of extremely high group indices in photonic crystal waveguides," Opt. Express **13**, 7861–7871 (2005).

A

Process recipe

More than 200 photonic-crystal membrane structures and circuits have been fabricated on the silicon-on-insulator (SOI) platform. The SOI wafer was manufactured by SOITEC and has a devices layer of 250 nm and buried oxide-layer of 3 µm. All the structures were fabricated at the DTU Nanolab facility in Lyngby. The process flow for fabricating these structures is described below.

1. Wafer cleaning: Acid/base fumehood
    - The Piranha solution is prepared by adding 1 part of concentrated H_2O_2 (30%) to a glass beaker containing 4 parts of concentrated H_2SO_4 (98%). The reaction is highly exothermic and hence this should be done inside the acid/base fume hood. The wafer is then placed in the beaker for 10 minutes. This removes most traces of organic type contaminants.
    - The wafer is then rinsed in DI water by gently agitating back and forth for 2 minutes, followed by another rinse in flowing DI water for 3 minutes.
    - The wafer is then transferred to the cassette of centrifugal spin dryer to get rid of excess water.
    - The temperature of the Piranha solution is allowed to settled down to 30 °C before disposing it off in the sink or into the container using the aspirator.
    - The wafer is then diced into small samples of size 2 cm × 2 cm.
2. Sample pre-treatment: Solvent fumehood
    - The sample is cleaned with acetone followed by a quick rinse with IPA solution. Acetone can leave behind residue if it is not dried immediately and hence IPA is used to wash any remnants of acetone.

- The sample is then nitrogen-blow dried to remove excess water.

3. Resist spin-coating: Labspin
   - The sample is mounted on the holder and using a disposable pipette (cleaned thoroughly) the resist CSAR-62 is dispensed on the sample. The parameters are shown in table. A.1. It is made sure that the resist puddle covers the entire chip including the edges. The lid is closed and the correct recipe is loaded.
   - After spin coating, the sample is then soft-baked at 180 °C for 60 seconds. This evaporates the solvent hardening the resist. Next, the sample is placed on the cooling plate for few seconds until it cools down.
   - Utmost care has to be taken in disposing the excess resist and cleaning the inlay set of the spinner. A 4K sterile glove, apron, and protective glasses should be worn while handling the cleaning solvent (solvent 1165).

Spin speed (rpm)	Accleration (rpm)	Thickness (nm)	Duration (sec)
3000	4000	215	60
2000	4000	275	60
1500	4000	310	60

Table A.1: CSAR-resist spin parameters

4. Pattern definition: E-beam writer JBX-9500FSZ
   - A number of layout editors can be used to create the mask field of the required design and is saved in the usually readable GDSII format. At the same time, a jobdeck file (JDF) and schedule file (SDF), which specifies the various condition for writing patterns is also prepared.
   - The next step is to create a pattern file that the machine understands. The exposure files are created in the machine readable format (. V30) using the BEAMER software. The following steps are performed.
     - In GDSII: Imports the GDSII file.
     - Heal: Performs logical OR operation on overlapping layers and heals them together in the output.

- Proximity effect correction (PEC): This process module performs correction for different electron scattering effects and artifacts. The electron scattering is specified using a point spread function (PSF) represented by a Gaussian approximation. The following PSF parameters are used.

PSF parameters	value
alpha	0.005
eta	0.6
beta	34

- Out GDSII: Generate and saves the output file in the V30 format. Always select center-to-field option in order to align the origin to the center of the pattern.

- The 20 mm × 20 mm sample is mounted in the appropriate slot of a chip-carrier cassette using an additional protective set of glove, which is then loaded into the autoloader by a trained staff from DTU Nanolab .
- While the cassette is being transferred from the autoloader into the e-beam writer, the condition file (0.2na_ap3) is calibrated which generates a magazine file. Before the exposure starts, some initial calibration will be performed automatically which keeps fluctuations of current and drift in control.
- After the exposure is finished, the machine will display a message. The cassette can then be transferred into the autoloading chamber and unloaded.

5. Resist development: Dedicated fumehood
   - The exposed sample is developed by immersing it completely in a beaker filled with a standard CSAR developer, AR-600-546. It is developed for 60 seconds at room temperature.
   - The sample is then rinsed with IPA solution for another 60 seconds followed by quick dry using nitrogen gun.

6. Silicon dry etch: Advanced silicon etch
    - The etching is done at a temperature of 10 °C, hence the first step is to set the temperature of the stage to 10 °C.
    - In order to ensure that the chamber is clean and free of contamination, a 10 minute preclean (O_2-clean) program is run on a dummy 4" silicon wafer. It is advisable to run this preclean procedure on a dummy wafer before every single etch process.
    - The sample to be etched is then glued to a 4" carrier wafer (top-layer oxide) using a crystal bond. If the crystal bond is spread uneven, the etch rates can vary at different corners of the sample. So it has to be spread evenly to have a uniform heat transfer before the sample is glued to it.
    - The carrier wafer is loaded into the etch chamber via the loading chamber. The correct etch-recipe is selected and the process is started. Since this is a an alternative cyclic process, an etching step of 5 seconds is followed by a passivation step for 3 seconds. A total of 7 cycles should be sufficient which leads to a total process time of 56 seconds. Few important parameters are listed below.

	Item	Quantity
Gas	C_4F_8	50 (sccm)
	SF_6	50 (sccm)
Etch cycle	time	5 (sec.)

	Item	Quantity
Gas	C_4F_8	50 (sccm)
	SF_6	0
Passivation cycle	time	3 (sec.)

Table A.2: Parameter settings. The important parameters for etch and passivation cycles are shown.

7. Ashing process: Inductively coupled plasma
    - A new O_2-clean process should be run with the sample still inside the chamber. This is to strip off most of the remaining resist.

	Item	Quantity
Gas	O_2	200 (sccm)
Clean cycle	time	3 (minutes)

    - The chamber is given a final round of O_2-clean for 20 min at 20 °C to make it ready for the next user.
8. Buried-oxide wet etch: Acid/base fumehood
    - Sioetch is an industry-grade BHF with a wetting agent. Care has to be taken to pour this chemical into a plastic beaker placed inside a acid fumehood. The sample is then immersed into this chemical with the help of a plastic handle for a period of 35 minutes at room temperature.
    - The sample is then slowly removed and rinsed in a water bath for 5 minutes. The membrane structures still run the risk of collapsing due to the surface tension of water.
    - The remaining sioetch has to be drained into the sink or drained using an aspirator.
9. Sample drying: Ethanol fume dryer
    - Ethanol is poured into the ethanol-vapour bath placed inside the solvent fumehood. Ethanol is heated to a temperature of 70 °C when it starts to fume.
    - The sample is placed inside this chamber filled with ethanol fume and the lid is closed for 20 minutes. Finally, the membrane structure is carefully taken out warm and dried.

B

Ensemble measurements

It is necessary to do an ensemble measurement on hundreds of samples when discussing statistical concepts like Anderson localization [112]. Over 200 photonic devices in different configurations have been fabricated and measured in this work. To avoid systematic errors, each device has been measured after careful realignment of the mirrors in the excitation path and the objective focus. This section consists of measurements done on multiple realizations and illustrates different aspects of the transmission measurements.

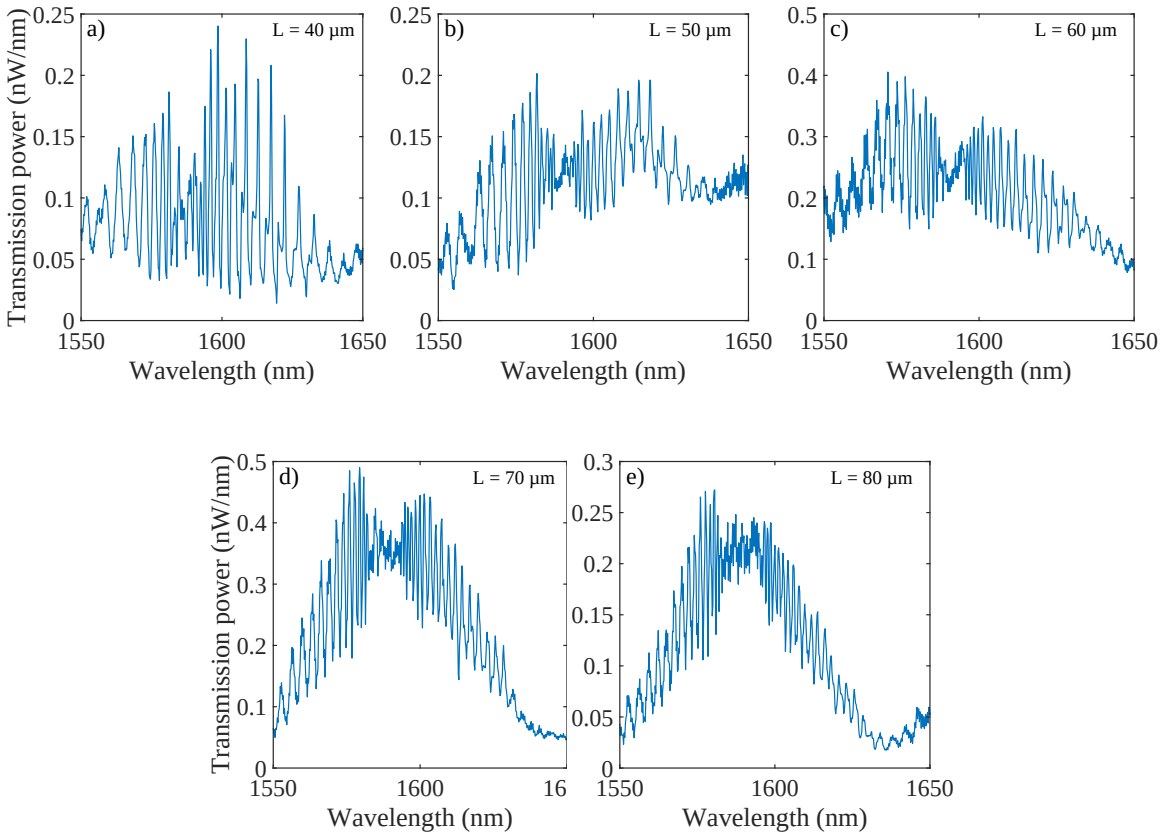

Figure B.1: Transmission measurement from cleaved-edge coupling.

(a-e) Transmission measurements on glide-symmetry waveguides with edge facets for different lengths of 40 µm to 80 µm.

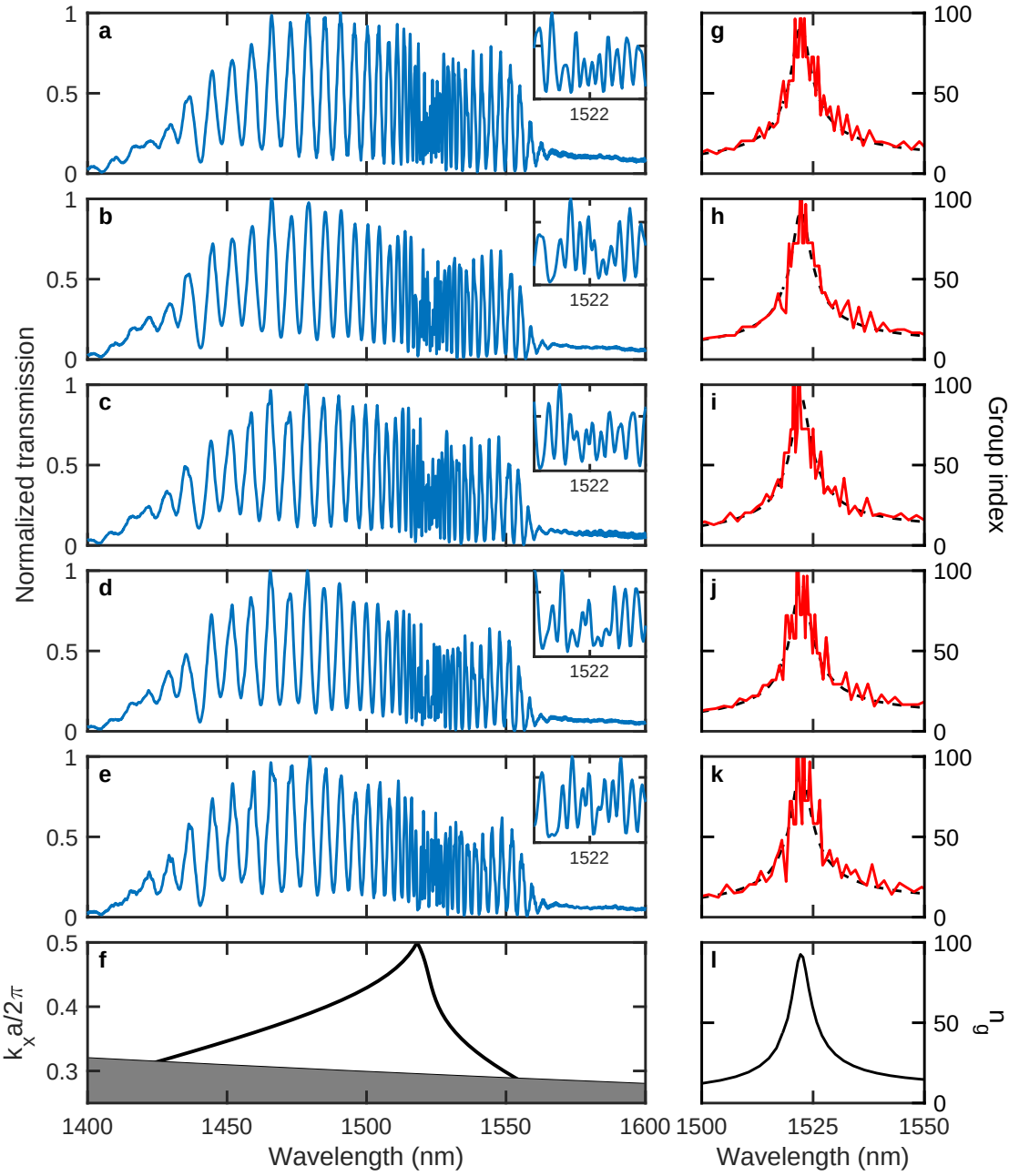

Figure B.2: Transmission of five nominally identical glide-plane waveguide resonators (length = 40 µm) with good incoupling conditions. (a-e) Normalized raw data exhibiting clear Fabry-Pérot resonance fringes, whose period is clearly reduced around the zone-edge degeneracy, cf. (f) the dispersion relation. The insets show the same data over a 10 nm span and centered at 1522 nm. (g-l) The extracted group indices (red) show excellent agreement with theory (black).

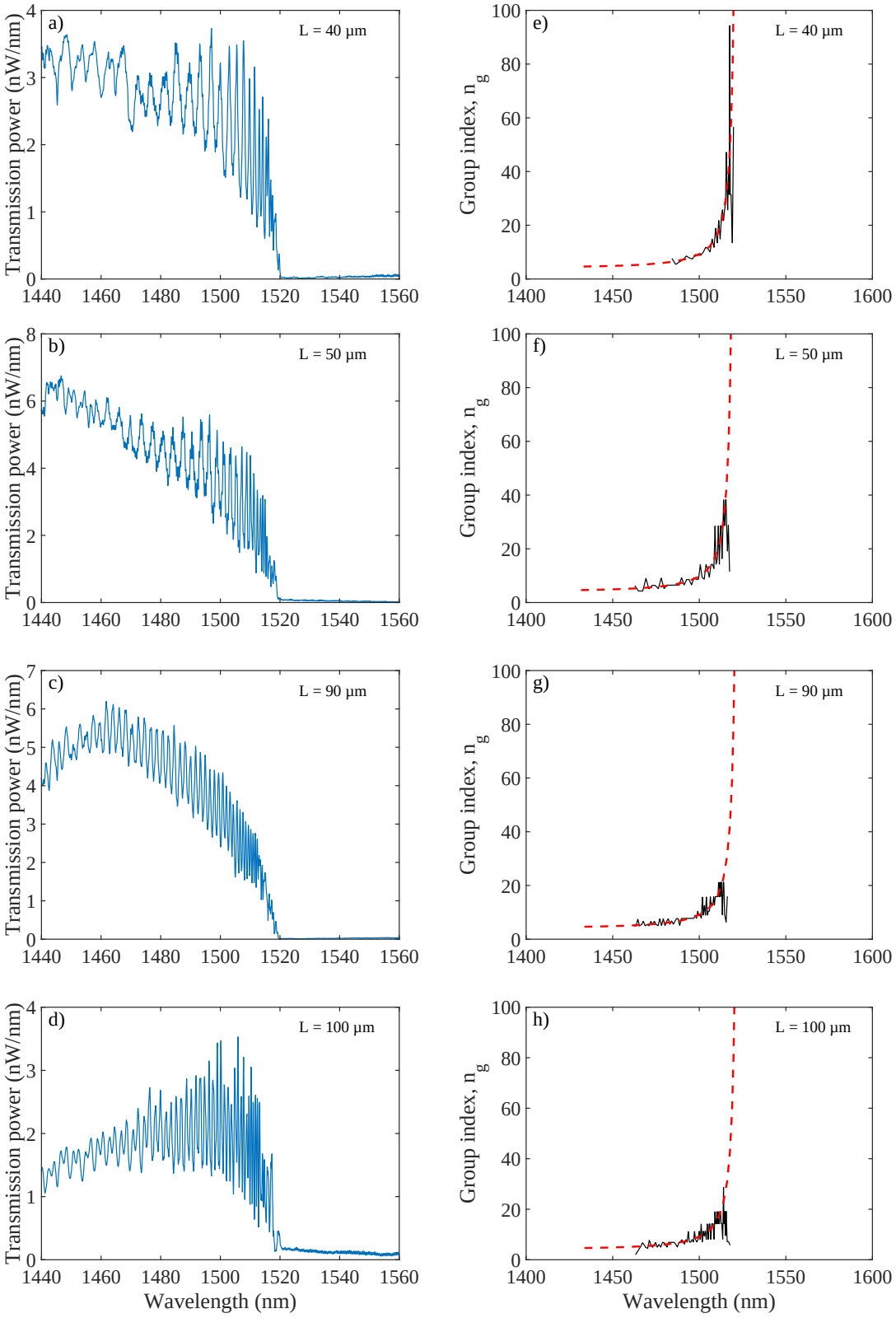

Figure B.3: Transmission spectrum of W1 photonic-crystals. (a-d) Transmission spectrum of W1 waveguide resonators with twice the number of characteristic Fabry-Peròt fringes. (e-h) The corresponding group index extracted experimentally without any correction factor.

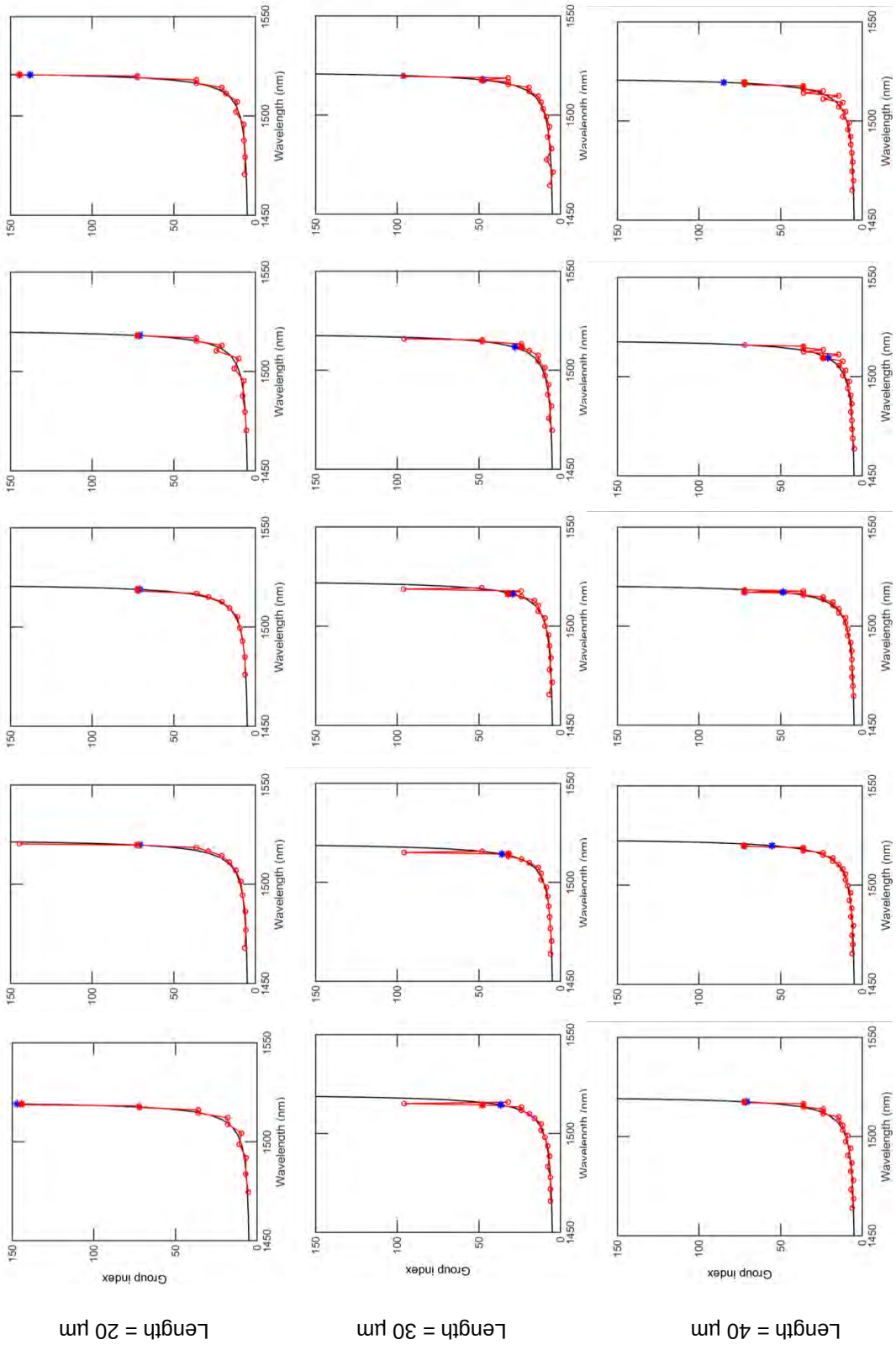

Figure B.4: W1 waveguides. Maximum group index for 5 different realizations of different lengths, criterion=0.2.

Length = 70 µm
Length = 60 µm
Length = 50 µm
Group index
Wavelength (nm)
150
100
50
0
1450
1500
1550

Length = 100 µm
Length = 90 µm
Length = 80 µm
Group Index
Wavelength (nm)
150
100
50
0
1450
1500
1550

Length = 40 µm
Length = 30 µm
Length = 20 µm
Group Index
Wavelength (nm)
150
100
50
0
1450
1500
1550

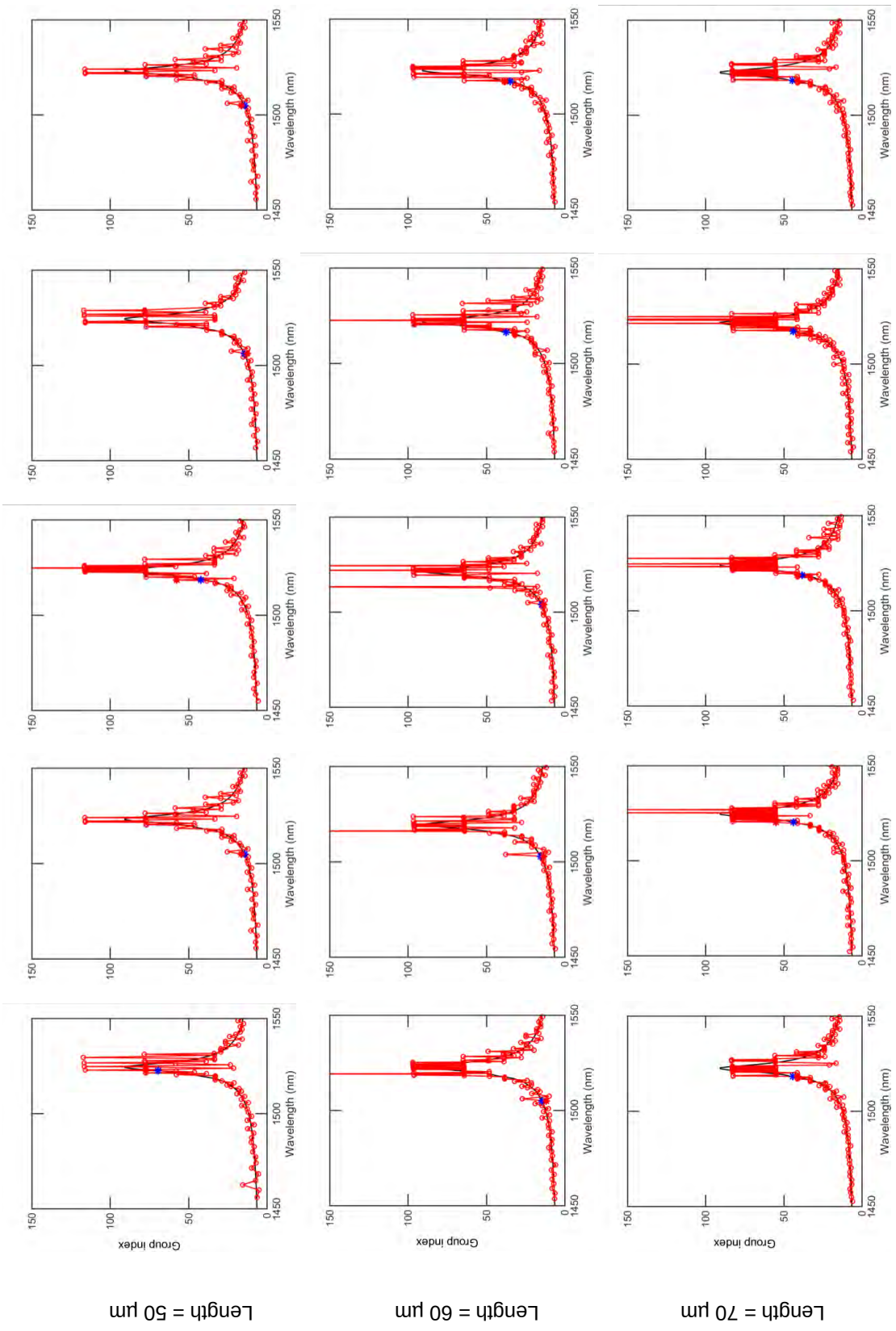

Figure B.5: Glide-symmetry waveguides. Maximum group index for 5 different realizations of different lengths, criterion=0.2.

Length = 100 µm
Length = 90 µm
Length = 80 µm
Group index
Wavelength (nm)
150
100
50
0
1450
1500
1550

C

Hole radii analysis

A MATLAB code to measure the hole dimensions by inspecting the scanning electron micrograph of a photonic-crystal structure is developed. It is assumed that fluctuation during the electron-beam lithography process are minimum and the holes are etched at a proper spacing. This spacing, or lattice constant can be considered as a known value in the code (standard scale) to measure the dimensions of different holes. The spacing between two rows of holes is not taken into account. This implies that if two rows of holes are closer to each other (pitch $< a$), it should not affect the measurement of the hole radii.

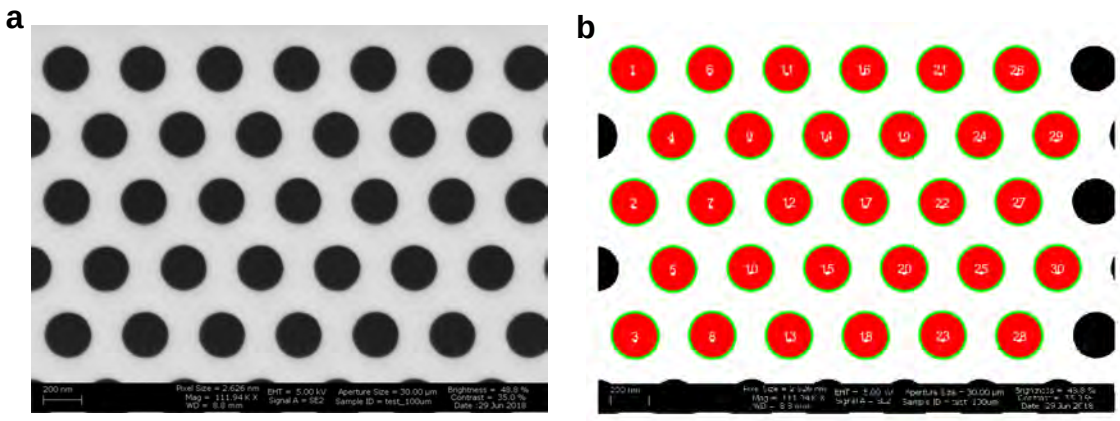

Figure C.1: Hole-radii analysis. (a) The scanning electron micrograph image of a standard photonic-crystal structure showing the air-hole structures. (b) The MATLAB processed image identifies the holes from other structures.

D

Fabry-Peròt fringe analysis

Group index is an important parameter to characterize any slow-light waveguide. Hence its reliable measurement is extremely important. A number of techniques have been proposed and used to extract group index: Fourier transform interferometry [173,174], time-of-flight (ToF) method [175], and the Fabry-Peròt fringe analysis [61]. Using the later method, the group index can be easily extracted from free spectral range or the spacing between adjacent peaks. This method is very easy and can also be used for highly dispersive media, where the fringe spacing changes as a function of wavelength especially at frequencies close to the cutoff wavelengths.

D.1 Peak search method

The free spectral range (FSR) is inversely proportional the the group index and hence the fringe spacing can be used to extract group indices as a function of wavelength. In terms of wavelength, the FSR is defined as,

$$\Delta\lambda_{FSR} \approx \frac{\lambda^2}{n_g L} \tag{D.1}$$

Here, n_g is the group index of the propagating medium, λ is the material wavelength, and L is the optical path length of the total distance covered by light in one round trip around the cavity length l. For our analysis, we use a slightly modified version of Eqn. D.1. We consider subsequent peak-valley spacing instead of peak-peak spacing. This adjustment gives us a slightly better group index value with higher resolution. Hence the group index is extracted using the equation

$$n_g = \frac{\lambda^2}{\Delta\lambda_{FSR} 4l} \tag{D.2}$$

Using the peak search option in Matlab®, an automatic peak finding routine was constructed which identifies the peaks and valleys and measures the group index at a given wavelength.

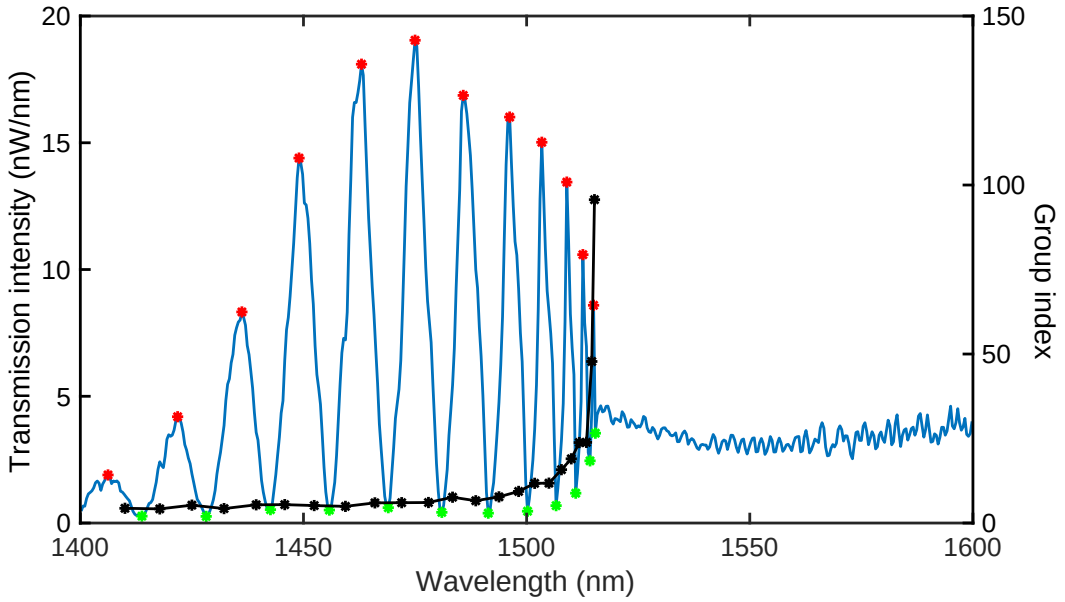

Figure D.1: Group index extraction. Transmission spectrum in a 30 µm long W1 waveguide. The different peaks(red) and valleys(green) identified by the peak-finding routine is highlighted. The calculated group index is plotted(black) at different wavelengths.

D.2 Calculating the shift parameter

The theoretically calculated group index has to be shifted by an offset value in order to compare and fit the experimentally measured group index. This compensates for the systematic shifts in hole radii and slab thickness that arises from fluctuations in fabrication process.

In order to measure the correct offset value, a routine was developed to measure the total variation in x-direction by scanning the theoretical group index around

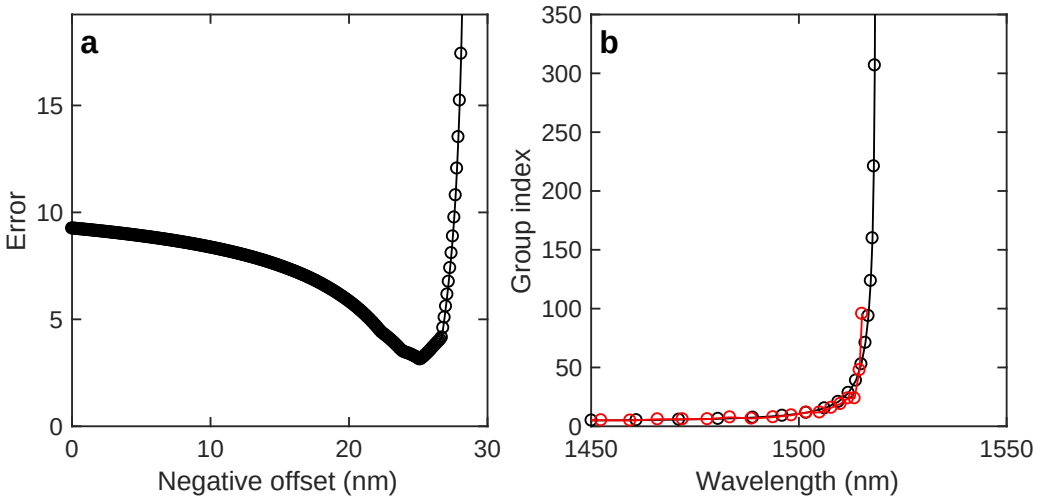

Figure D.2: Theoretical shift in group index. (a) The error computed for different offset values showing a minima at offset = 25.1 nm. (b) The theory group index (black) is shifted by 25.1 nm providing a good fit with the group index extracted from experiment (red).

the experimentally extracted value. This gives a local minima in the error plot as shown in Fig. D.2. This local minima precisely gives the offset value by which the theoretical group index has to be shifted.

D.3 Factor of 2 in group index

The waveguide modes are excited by carefully optimizing the laser beam spot over the input gratings. The collection path is also optimized at the same time. It has been observed that moving the laser spot around the input gratings would cause the spectral features to shift back and forth. This has been described in detail by Morten Herskind in his thesis [165]. It is quite clear that there are two different signals that were interfering with each and beating with their own frequencies. This appears as shoulder signal in shorter devices and becomes more apparent in longer devices.

When light enters into a cavity at a certain angle, the phase builds up after completing an optical path at each interface. Eventually, when it build up a phase of 2π, standing waves are formed and resonance is observed. At the same time, when light

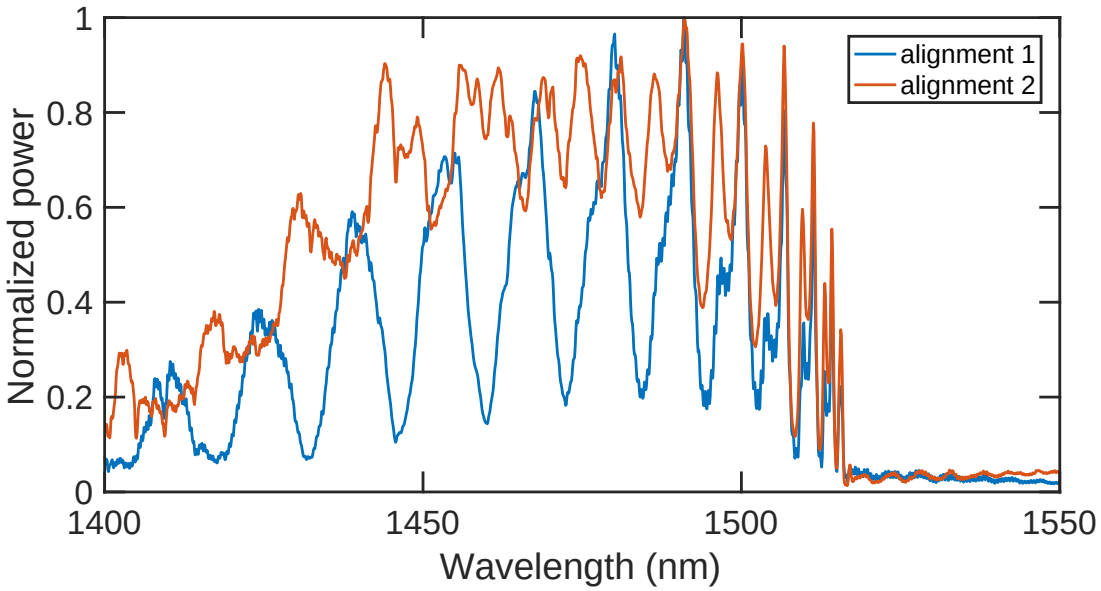

Figure D.3: Transmission comparison between two different alignments. The transmission spectra of the same W1-waveguide resonator (length=30 µm) measured with two different alignments. The spectrum in red shows twice the number of peaks that is observed in blue spectrum.

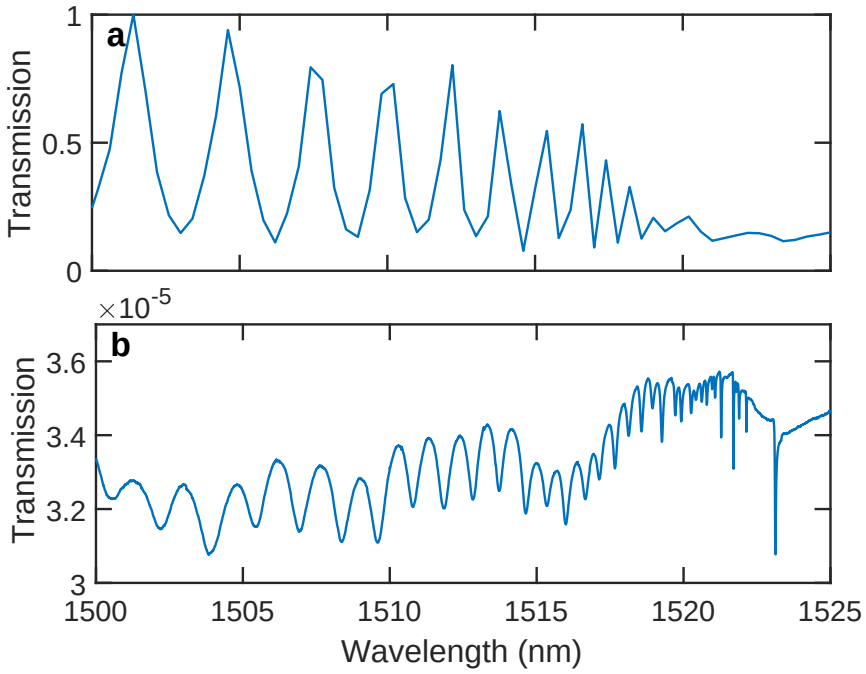

Figure D.4: Transmission comparison between two different setups. The same W1-waveguide resonator of length 70 µm, is measured with two different setups. The spectrum in (a) is measured with free-space optics setup and the spectrum in (b) is measured with evanescent-coupling setup.

enters into the cavity from a different angle, it builds up phase, but is distinctly out of phase with the first signal. Depending on the amplitude of these two waves, few peaks will be partially suppressed and this is what is observed in the experiment. Since the gratings are smaller than the laser spot, the point where light is focused is not certain. Depending on the way light impinges on the grating coupler, the two signals can be in or out of phase and this is observed in few measurements as shown in Fig. D.3.

This was further confirmed by transmission measurements done on the same sample using an evanescent-coupling method by Guillermo Arregui at the Catalan Institute of Nanoscience and Nanotechnology (ICN2), Barcelona as shown in Fig. D.4b. Since the setup couples light into the waveguide section directly, there is no interference from the gratings as such. Consequently, the measured spectrum is free from destructive interferences and other spurious scattering.

E

Polarization experiments

In this section, the measurement and characterization of glide-symmetry waveguides with different polarization settings is shown. The polarization test measurements were done on the resonator setup and the orthogonal setup.

The photonic-crystals have been designed such that only TE-like modes are excited. Preparatory tests were performed to see if any TM-like modes could also be excited. The input polarization was controlled by a half-wave plate in the input-path, while the output signal was monitored using polarization filters.

For the resonator setup shown in Fig. E.1a, TE-modes were excited, and a TM-polarization filter was placed in the path of the output signal. Hence only TE-like signal was measured (green arrow). For Fig. E.1b, a TE-polarization filter was placed at the output path which blocks transmission of the TE-excited modes. Similarly, Fig. E.1c and d shows that some TM-modes can be excited within these waveguides as well. However, it has to be noted that the mirrors were aligned to maximise the transmission in all the cases. Hence, the angle with which we hit the circular gratings can have an effect on the type of modes that is being excited. The same procedure was also done for the glide-plane waveguide devices in the orthogonal setup (see Fig. E.2) and similar trends were observed indicating that there is no considerable TE-TM mode mixing.

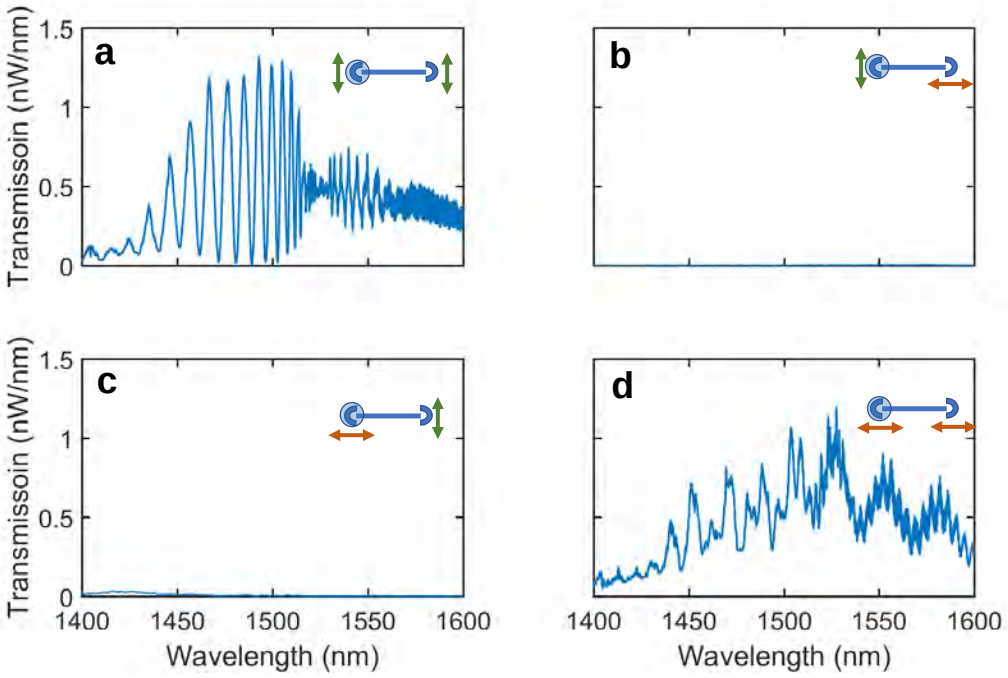

Figure E.1: Different polarization configurations for resonator setup. Transmission in a glide-symmetry waveguide with different configurations of the in-out polarization can be seen. The coupler highlighted in blue shade corresponds to the point of excitation. The green and red arrows represent the TE- and TM-polarization of the measured signal.

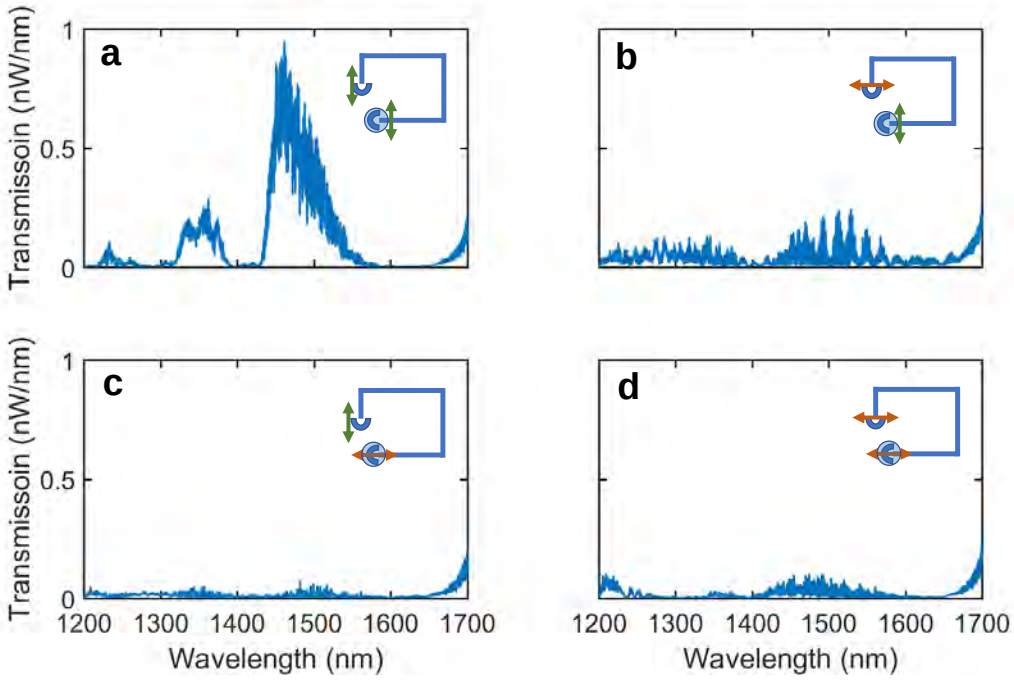

Figure E.2: Different polarization configurations for orthogonal setup. Transmission in an orthogonal setup with different configurations of the in-out polarization can be seen. The two couplers are positioned orthogonal to each other, and the coupler highlighted in blue shade corresponds to the point of excitation. The green and red arrows represent the TE- and TM- polarization of the measured signal.